# Université de Montréal

# Characterization of the radiation field in ATLAS using Timepix detectors

par

# Thomas Billoud

Département de Physique
Faculté des arts et des sciences

Thèse présentée à la Faculté des études supérieures et postdoctorales
en vue de l'obtention du grade de
Philosophiæ Doctor (Ph.D.)
en Physique

mai 2019

# Université de Montréal

Faculté des études supérieures et postdoctorales

Cette thèse intitulée

# Characterization of the radiation field in ATLAS using Timepix detectors

présentée par

# Thomas Billoud

a été évaluée par un jury composé des personnes suivantes :

*Sjoerd Roorda*

(président-rapporteur)

*Claude Leroy*

(directeur de recherche)

*Jean-François Arguin*

(membre du jury)

*Alan Owens*

(examinateur externe)

*Sjoerd Roorda*

(représentant du doyen de la FESP)

Thèse acceptée le :

*16 Octobre 2019*

# Résumé

Le travail présenté dans cette thèse porte sur le réseau de détecteurs à pixels ATLAS-TPX, installé dans l'expérience ATLAS afin d'étudier l'environement radiatif en utilisant la technologie Timepix. Les travaux sont rapportés en deux parties, d'une part l'analyse des données recueillies entre 2015 et 2018, d'autre part l'étude de nouveaux détecteurs pour une mise à niveau du réseau.

Dans la première partie, une méthode pour extraire certaines propriétés des MIPs (*Minimum Ionizing Particles*) est développée, basée sur l'étude des traces laissées par ces particules lorsqu'elles traversent les matrices de pixels des détecteurs ATLAS-TPX. Il est montré que la direction des MIPs et leur perte d'énergie (dE/dX) peut être déterminée, permettant d'évaluer leur origine. De plus, la méthode pour mesurer les champs de neutrons thermiques et neutrons rapides avec ces détecteurs est expliquée, puis appliquée aux données. Les flux de neutrons thermiques mesurés aux différentes positions des détecteurs ATLAS-TPX sont présentés, alors que le signal des neutrons rapides ne se distingue pas du bruit de fond. Ces résultats sont décrits dans une publication, et la façon dont ils peuvent être utilisés pour valider les simulations de champs de radiation dans ATLAS est discutée.

Dans la seconde partie, la thèse présente une étude de détecteurs Timepix utilisant l'arséniure de gallium (GaAs) et le tellurure de cadmium (CdTe) comme capteur de radiation. Ces semiconducteurs offrent des avantages par rapport au silicium et pourraient être utilisés dans les prochaines mises à niveau du réseau ATLAS-TPX. Comme ils sont connus pour des problèmes d'instabilité dans le temps et une efficacité de collection de charge incomplète, ils sont testés en utilisant divers types d'irradiation. Ceci est décrit dans deux articles, l'un portant sur un capteur au GaAs de $500\,\mu m$ d'épaisseur, l'autre sur un capteur au CdTe de $1\,mm$ d'épaisseur. Malgré l'apparition de pixels bruyants lors des mesures, les détecteurs montrent une bonne stabilité du signal dans le temps. Par contre, l'efficacité de

collection de charge est inhomogène à travers la surface des détecteurs, avec des fluctuations de produits *mobilité-temps de vie ($\mu\tau$)* importantes. Ces résultats montrent qu'il est nécessaire d'étudier l'influence de ces défauts sur les algorithmes de reconnaissance de traces avant l'utilisation du GaAs et CdTe dans les mises à niveau du réseau ATLAS-TPX.

**Mots-clés: mesure de radiation, ATLAS, Timepix, détecteur GaAs, détecteur CdTe**

# Abstract

The work presented in this thesis focuses on the ATLAS-TPX pixel detector network, installed in the ATLAS experiment for studying the radiation environement using the Timepix technology. The achievements are presented in two parts, on one hand the analysis of data acquired between 2015 and 2018, on another hand the study of new detectors for an upgrade of the network.

In the first part, a method to extract properties of MIPs (*Minimum Ionizing Particles*) is developed, based on the analysis of clusters left by the interaction of these particles in the pixel matrixes of the ATLAS-TPX detectors. It is shown that the direction of MIPs and their energy loss (dE/dX) can be determined, allowing the evaluation of their origin. Moreover, the method for mesuring the thermal and fast neutron fields is explained, and applied to the data. The thermal neutron fluxes at the different detector locations are reported, whereas the fast neutron signal cannot be distingished from the background. Thoses results are described in a publication, and their use for benchmarking simulations of the radiation field in ATLAS is discussed.

In the second part, the thesis presents a study of Timepix detectors equipped with gallium arsenide (GaAs) and cadmium telluride (CdTe) sensors. These semiconductors offer some advantages over silicon and could be used for upgrades of the ATLAS-TPX network. Since they are known to suffer from time instabilities and incomplete charge collection efficiency, they are tested using several types of irradiation. This is described in two publications, one focusing on a $500\,\mu\mathrm{m}$ thick GaAs sensor, another focusing on a 1mm thick CdTe sensor. Despite the appearance of noisy pixels during the measurements, the detectors are found to be reasonably stable in time. However, the charge collection efficiency is found to be inhomogeneous across the sensor surfaces, with significant fluctuations of *mobility-lifetime ($\mu\tau$)* products. These results show that

it is necessary to study the influence of these material defects on the pattern recognition algorithms before the integration of such sensors in the ATLAS-TPX upgrades.

# Personal contributions

I present here an overview of my work done during the PhD program, which lasted from late 2013 to early 2019 and included two propaedeutic years.

**Timeline overview**

Having a background in electronics engineering, the first two years of my PhD were mostly dedicated to courses on theoretical and experimental particle physics, and related subjects. In parallel, I contributed to the calibration and installation of the ATLAS-TPX detector network at the Large Hadron Collider (CERN) from 2014 to mid-2015. Soon after, I started my involvement in the ATLAS experiment by performing monitoring shifts for the calorimeter and forward detector systems. These 8 hrs-long shifts were done in the ATLAS control room at CERN. They involved calibration runs, coordination between maintenance activities of the sub-system experts, and continuous surveillance of the detectors' status and data acquisition during LHC runs. I dedicated about two months per year to this task from 2015 to 2018.

From 2015 to early 2016, I achieved my ATLAS authorship qualification task, which is a required work to become a co-author of the ATLAS collaboration. This involved the analysis of ATLAS-TPX data for luminosity monitoring. My results were used by the ATLAS-TPX luminosity group for publications [**1**], but are not included in this thesis which focuses on more consequent personal achievements.

From early 2016 to late 2017, my main research activities were related to the characterization of new TPX detectors with CdTe and GaAs sensors, which is the subject of chapter 4. For these investigations, I used the Tandem accelerator of UdeM (University of Montreal), with the help of the responsible technician and ATLAS collaborators, and other radioactive sources available at this facility ($^{241}$Am, $^{137}$Cs). I organized with ATLAS collaborators a

Rutherford backscattering setup to irradiate the CdTe Timepix detector with a proton beam at various energies. I also used an X-ray facility at IEAP (Institute of Experimental and Applied Physics in Prague) for detector calibrations and characterizations. There, I exposed fluorescence foils to X-rays in order to obtain mono-energetic sources. I performed analysis of the obtained data with the MAFalda framework. This is a C++ and ROOT [2] based software developed at UdeM for the Medipix/Timepix community, that unifies several analytical utilities for pattern recognition and integration of user-defined algorithms, but needs to be adapted for specific applications. I extended the program for my purposes and worked on the time-consuming task of writing new algorithms to study the charge collection efficiency in GaAs. This analysis required theoretical and algorithmic developments for taking into account the small pixel effect in the Hecht equation, and for fitting this model to the data recorded by the 65536 pixels of the detector. Based on this analysis, I wrote two articles (included in chapter 4), one addressing the CdTe Timepix detector, and one addressing the GaAs detector. I presented some of the results at a Medipix collaboration seminar at CERN.

Finally, in 2018, I focused my research activities on the analysis of ATLAS-TPX data, which is the subject of chapter 3. To characterize the radiation field in ATLAS with these detectors, I had to develop new algorithms. Therefore, I created a C++/ROOT based software for convenient comparison between different algorithms and data visualization. In parallel, I began to validate these algorithms using Monte Carlo simulations. Here, I used an open-source software based on Geant4 [3] and specialized for pixel detectors, called Allpix2 [4]. Since this program was developed by a team working on vertex detectors, I had to adapt the code for my needs. The developed algorithms led to successful results from the analysis of the ATLAS-TPX data, that allowed me to write the article included in chapter 3. Preliminary results were presented at the IEEE Nuclear Science Symposium of 2018. The article was submitted for publication to IEEE TNS in February 2019. At the same time of these research activities, I helped with the maintenance of ATLAS-TPX detectors and to the installation of new prototypes (i.e. Timepix3 detectors) tested in 2018 for the future upgrade.

## Additional experience

For every code development performed during my research activities, I tried as much as possible to write clean, reusable and publicly available code. This habit can be time-consuming, but it allows to share the acquired experience with the pixel detector community, which can lead to a faster and more efficient technology development. The aforementioned MAFalda and Allpix2 frameworks are tools following this line of thinking. Thus, I integrated my developments to these frameworks whenever appropriate, as can be seen on the public code repositories [5, 6]. In addition, the program I developed for the analysis of ATLAS-TPX data is also accessible on the web [7].

Finally, at the UdeM Tandem accelerator, I performed with ATLAS collaborators additional measurements with He, Li, C and O ions to investigate the energy resolution and amplifier response of Timepix detectors. In the context of pattern recognition studies, I also participated in measurements at the SPS (Super Proton Synchrotron, CERN), Prague Microtron MT25, and Prague Van De Graaff accelerator (IEAP CTU[1]).

---

[1]Institute of Experimental and Applied Physics, Czech Technical University, Prague

# Contents

# List of tables

# List of figures

# Acronyms

**ASIC:** Application-Specific Integrated Circuit

**CCE:** Charge Collection Efficiency

**CERN:** Centre Européen de la Recherche Nucléaire

**IEAP:** Institute of Experimental and Applied Physics in Prague

**IP:** Interaction Point

**MIP:** Mimimum Ionizing Particle

**MPX2:** Medipix2

**PCB:** Printed Circuit Board

**SPS:** Super Proton Synchrotron

**TPX:** Timepix

**TPX3:** Timepix3

**UdeM:** Université de Montréal

# Acknowledgments

First, I would like to warmly thank my PhD supervisor, Prof. Claude Leroy, for his support in my research activities and for his guidance in general.

At the University of Montreal, I have been helped with several colleagues for experimental setups. I annoyed the technician operating the Tandem accelerator a lot, so I thank Louis Godbout for his patience. I performed many measurements with the help of a PhD mate, Costa Papadatos, and gave a hard time to Jean-Samuel Roux (BSc. student) for help with code development. During my PhD experience at the GPP[2] group of UdeM, I have had a feeling of professionalism and consideration, to which Jean-François Arguin and Peggy Larreau contributed.

At IEAP (Prague), I have received a lot of experimental support and expertise from Benedikt Bergmann and Martin Pichotka. I am grateful to the former institute director Stanislav Pospisil, for his welcome and plentiful scientific advices, and to his successor, Ivan Stekl, for continuing to trust in me. The engineering team were also very supportive for detector related purposes, in particular Ing. Yesid Mora.

Finally, I am grateful to my girlfriend, Roxane Martz, for following me to Canada and to my parents, Evelyne Boguet and Pierre Billoud, for their continuous support.

---

[2]Groupe de Physique des Particules

# Introduction

Collider experiments require high collision rates, i.e. high energies and luminosities, to investigate physics beyond the Standard Model. The LHC is currently the largest accelerator worldwide, providing about a billion proton-proton collisions per second at a center-of-mass energy of 13 TeV. Despite the exciting discovery potential provided by this achievement, experiments face serious challenges in terms of performance, lifetime and maintenance of their detectors. Indeed, the harsh radiation environment generated by collisions induces high levels of background, radiation damage to electronics and sensors, and induced radioactivity. This was known long before LHC operation, and studies of the radiation field contributed to the design of LHC experiments [8]. For ATLAS, Monte Carlo simulations were performed during more than two decades in order to obtain a detailed knowledge of the expected radiation environment, before the start of the LHC operation in 2008 [9, 10].

Even though simulation tools can predict detailed properties of particle fields at any location in the experiment, actual measurements must be performed once the accelerator has started providing collisions. In ATLAS, several monitors were installed in detector systems particularly affected by the adverse effects of radiation, such as in the inner detector or the muon chambers [11]. While serving their purpose, these monitors only see localized parts of the radiation environment and are typically sensitive to one type of radiation only. In the 2000s, a new particle tracking technology emerged from the Medipix collaboration at CERN, called the Timepix detectors. These are small hybrid pixel detectors capable of measuring charged particles, photons and neutrons at the same time, using a sensor that can be made of several semiconductors such as silicon, GaAs or CdTe. In view of their success as radiation monitors in other applications, it was decided to install a network of such devices [12] at various positions in ATLAS to characterize the radiation field from a more global perspective as other detectors do. A first network, ATLAS-MPX [13], operated

during LHC Run-1 (2010-2013) [14], and was upgraded for the LHC Run-2 (2015-2018) [15] using more recent chip generations. This network upgrade, ATLAS-TPX [16], is the subject of the present thesis. Both analysis of the data obtained during LHC Run-2 and possible future upgrades are investigated.

The first chapter briefly describes the overall context of the ATLAS experiment, with its physics goals and its design. The second chapter is an introduction to particle tracking with Timepix detectors, encompassing general particle detection principles, chip descriptions and data analysis tools. The two last chapters contain the achievements of the thesis. They were submitted in three separate papers (two published, one being reviewed), which are included in their entirety and accompanied with explanatory sections. The third chapter presents results obtained from the ATLAS-TPX network, with discussions about their potential for radiation simulation benchmarking. Finally, the fourth chapter is a preliminary investigation of Timepix detectors with high-Z sensors, which have been available only recently and could be used together with Timepix3 chips for the next upgrade of ATLAS-TPX.

# Chapter 1

## The ATLAS experiment

## 1.1. Status of Particle Physics in 2019

If Aristotle's ideas about the fundamental constituents of nature were not challenged by the curiosity of others, we would think that everything is made of earth, water, air and fire. Luckily, this rather philosophical question has occupied many minds over the centuries. Democritus brought forth the idea of *indivisible atoms* in the $4^{\text{th}}$ century BC, but we had to wait more than twenty centuries for a real scientific breakthrough. Some of the standing out initiators of that breakthrough, at the end of the 19th century, are J. Dalton with his investigation on elemental weights, and J.J. Thomson who separated the electron from the *heavier* part of matter. Soon after, Rutherford, Geiger and Marsden revealed this heavier part of matter with their famous gold foil experiments, establishing a first milestone in the understanding of the fundamental constituents of matter. Further research in this topic then emerged as *particle physics* for some, and *nuclear physics* for others, encompassing several methods such as particle accelerators and related detectors, which is the context of the present thesis.

The origin of this scientific area can be traced back to the 1930s, when experimental physicists investigating elementary particles could not be satisfied anymore by radioactive and cosmic ray sources [17]. They expressed the need for intense beams of energetic particles, which was materialized for example with the Cockroft-Walton Generator, one of the first particle accelerators. During the following decades, the development of such machines led to regular discoveries of elementary particles, following the evolution of achievable energies and collision rates. The milestones achieved were also the result of detector development,

adapted to the increasing energies available, making access to smaller constituents possible and allowing study of their properties and interactions. By the 1970s, the accumulation of these discoveries led to the establishment of a solid theory of fundamental interactions and particles called the *Standard Model* [18] (SM). Since then, several predictions of the model have been confirmed, such as the top quark in 1995 [19] or the tau neutrino in 2000 [20]. The last expected milestone was the discovery of the Higgs Boson, which was achieved in 2012 by the ATLAS and CMS experiments at CERN[1] [22, 23]. However, it has been suspected, since its inception, that the SM is not a complete theory. The simple fact that the theory is built upon arbitrary parameters, for example, raises the suspicion of theorists [24]. One might also wonder whether quarks and leptons really are elementary particles [25]. In addition, several experimental observations revealed inconsistencies with the SM. For example, neutrino oscillations experiments showed that neutrinos have a mass, contrary to the SM where they are massless, and a series of astrophysical and astronomical observations lead to the hypothesis of dark matter and dark energy, not predicted by the SM.

To answer these questions, high energy accelerator experiments are still considered as a tool-of-choice nowadays. Currently, the *terra incognita* explorer of accelerator physics is the Large Hadron Collider (LHC) at CERN [26], a storage ring accelerating two proton beams colliding at a maximum center-of-mass energy ($\sqrt{s}$) of $13\,\text{TeV}$. Now that the Higgs boson has been confirmed, an important focus is directed towards physics beyond the SM, including supersymmetry and other theories such as composite quark models, extra dimensions or the grand unified theory [27]. Since the LHC has the highest energy ever achieved by an accelerator to date, unexpected findings are also possible. The accelerator gave first collisions at $\sqrt{s} = 7\,TeV$ in 2010 [28], and is now in a shutdown period (2019-2020) to upgrade its injector. Its last main upgrade will be the High-Luminosity-LHC (HL-LHC), which should operate from 2027 to 2037 with a significantly higher luminosity and an energy reaching $\sqrt{s} = 14\,TeV$ [29, 30]. Extensive efforts are being invested in this project, with about 7,000 scientists [29] working on the four main experiments (CMS, ATLAS, ALICE, LHCb), and

---

[1]Centre Européen pour la Recherche Nucléaire, increasingly called the European Laboratory for Particle Physics in literature [21].

new analytical tools (e.g neural networks) are being developed to confront the huge amount of recorded data. Unfortunately, no evidence of new physics has been found so far [27].

For the future, one hope of the particle physics community is that still increasing accelerator energies and luminosities will lead to findings beyond the standard model. Various projects are ongoing or considered around the world [31, 32]. However, the resources needed for such infrastructures are reaching a point where it becomes difficult to convince the public [33]. In this regard, it is important to remember that accelerators are not the only way of studying high energy particles. Indeed, space physics is also a very active field, with sophisticated detection systems being built continuously.

## 1.2. Proton collisions at the LHC

The LHC is a synchrotron-type accelerator of 27 km circumference. Before they enter the LHC, protons are pre-accelerated by a chain of 4 accelerators, reaching 450 GeV in the Super Proton Synchrotron (SPS). They are transfered to the LHC rings bunch by bunch, and then further accelerated by superconducting magnets. The center-of-mass energy was increased gradually up to 8 TeV during LHC Run-1[2] (2010-2013), and ramped up to 13 TeV for the LHC Run-2 (2015-2018). Nominally, a LHC beam can contain 2808 bunches of $10^{11}$ protons each, squeezed so that there can be about 20 collisions per bunch crossing [34]. During Run-2, the LHC went beyond the nominal performance, reaching an average of 37 collisions per bunch crossing [15]. This determines the achieved instantaneous luminosity ($\mathscr{L}$), a key parameter for an accelerator representing its collision rate performance. Considering an interaction with cross section $\sigma$, one can calculate the rate of events ($R$) with:

$$R = \mathscr{L} \cdot \sigma \tag{1.2.1}$$

The total cross section for inelastic proton-proton collisions at 13 TeV being $\sim 70$ mbarns [35], the LHC produced during its 2018 luminosity peaks ($\mathscr{L} \sim 2 \cdot 10^{34}$ cm$^{-2}$ s$^{-1}$) about $10^9$ collisions every second. In order to study rare processes, one needs to obtain a maximum integrated luminosity over time, which requires high instantaneous luminosity and a continuous operation of the accelerator. Since the number of protons in each beam decreases while collisions

---

[2]A LHC *Run* is a continuous operation of the LHC over the years, followed by a *long shutdown* during which major upgrades are done on the accelerator and detectors. The LHC Run-1 period was 2010-2013, Run-2 was 2015-2018 [14, 15]. A daily collision period, with start/stop of the machine, is called a *fill*.
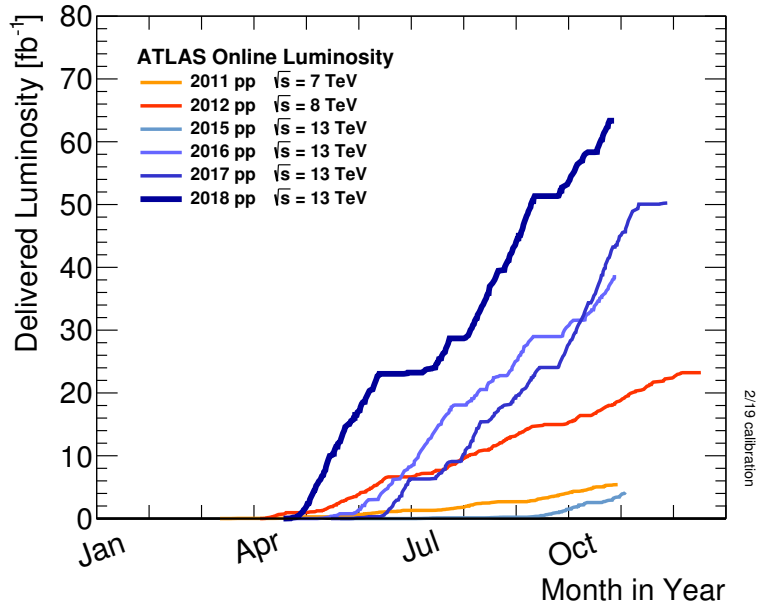
**Fig. 1.2.1.** Integrated luminosity recorded by ATLAS as a function of time, during the years after 2010 [**36**].

go on, the collision rate decreases accordingly, and when the instantaneous luminosity is no longer deemed sufficient, beams are dumped and new ones are injected. The delivered luminosity[3] is illustrated in figure 1.2.1, showing the operation and performance of the LHC over the years.

While the ever increasing luminosity improves the discovery potential, it results in serious challenges for detector lifetime and performance. Each proton-proton collision produces hundreds of secondaries (including neutrons), which interact in the surrounding materials and create subsequent radiation such as the gamma fields related to induced radioactivity. This radiation environment has various deleterious consequences, which require a careful detector design. Indeed, it is important to 1) detect physics processes successfully and 2) allow the experiment to survive these adverse conditions during the entire LHC runs.

---

[3]The delivered (or *integrated*) luminosity is the integration of the instantaneous luminosity over time and is usually given in *inverse barn*, instead of cm$^{-2}$. One barn is equal to $10^{-24}$ cm$^2$. In the figure, the delivered luminosity is given in *inverse femtobarns* (fb$^{-1}$), as is commonly done in the literature.
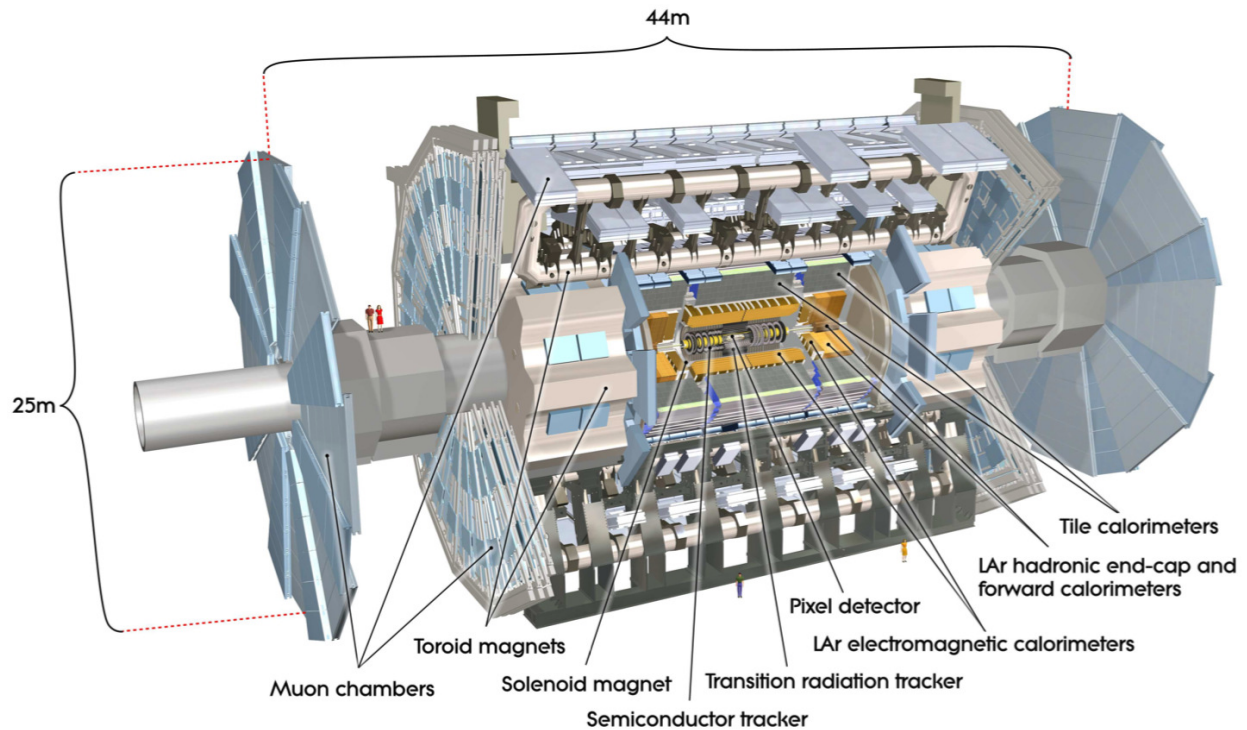
**Fig. 1.3.1.** Overview if the ATLAS detector [**11**].

## 1.3. The ATLAS detector design

At the LHC, two general-purpose experiments were proposed to investigate new physics, each with a specific design [**37**]: ATLAS and CMS. The main conceptual differences are in the magnet systems, used for identifying charged particles and measuring their momenta by bending their trajectories. CMS stands for Compact Muon Solenoid: one solenoidal magnet deflects both highly interacting particles, stopped in the calorimeters, and energetic muons, which have low stopping power and escapes further away. ATLAS (A Toroidal LHC Apparatus), on the other hand, has two magnets: one core solenoid, and one large outer toroid dedicated to escaping muons. Shaped as a 44 m long cylinder with 25 m radius, the ATLAS experiment contains 7000 tonnes of material which is shared between detection systems and their radiation shieldings.

### 1.3.1. Sub-detectors

The ATLAS detector is thoroughly described in Ref. [**11**]. An overview of its structure is illustrated in figure 1.3.1. It is composed of cylindrical sub-detector layers added on top
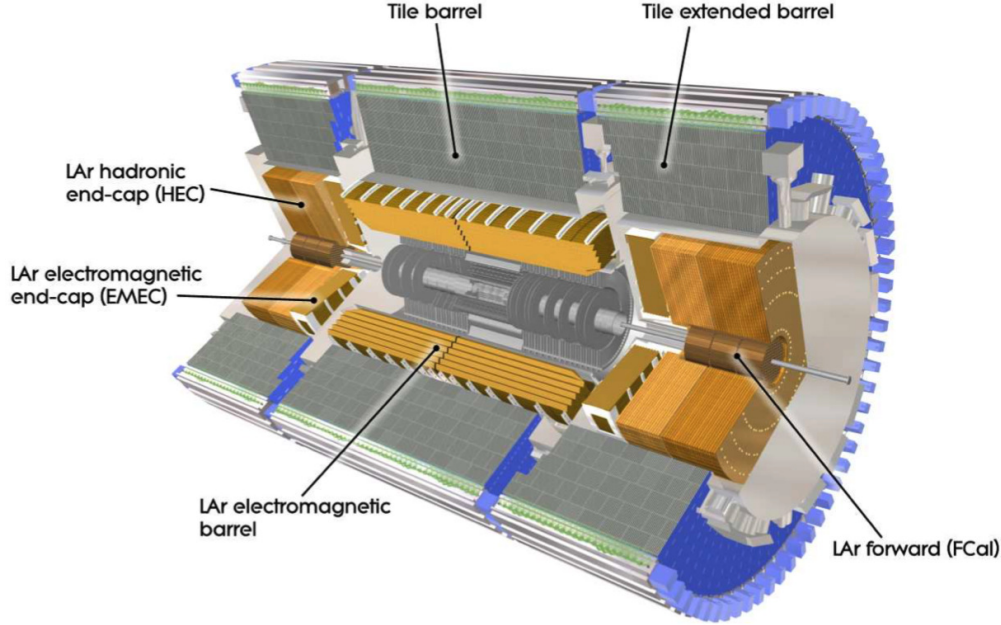
**Fig. 1.3.2.** The ATLAS calorimeter. It is composed of an inner layer for electromagnetic showers, the *LAr barrel*, which uses liquid argon (LAr) as active material and lead as absorber. A second outer layer, the *Tile barrel*, is dedicated to hadronic showers: scintillating tiles were chosen as active component and steel as absorber [**11**]. In the end-caps and forward regions, additional LAr calorimeters are installed to increase the solid angle coverage.

of each other, in a similar way as onion layers, which can be grouped in three main parts listed below in order of proximity to the interaction point (IP):

- the inner tracker: high spatial granularity for precise trajectory reconstruction. It is composed of a pixel detector, a strip detector and a transition radiation tracker (see figure 1.3.1).

- the calorimeter: heavy absorber materials for stopping most particles and active materials for measuring their energy. See figure 1.3.2 and its caption for a more detailed description. It is surrounded by the solenoid magnet.

- the muon system: gas-filled detection chambers integrated with the toroidal magnet.

Even though each particle interacting in those detectors produces a signal, electronic readouts are not capable of recording all proton-proton collisions during the bunch spacing time. Consequently, the experiment is equipped with a trigger system that filters events of interest for physics analysis. This system takes information from various detector sub-components

as input, and performs online computations to select desired data. Finally, four independent detectors are placed in the forward regions:

- LUCID (LUminosity measurement using Cerenkov Integrating Detector). It monitors the online luminosity, and is calibrated using measurements from other detectors [38].
- ALFA (Absolute Luminosity For ATLAS), scintillating fiber trackers placed in Roman pots that can move as close as $1\,\mathrm{mm}$ to the beam [39]. It measures the absolute luminosity, and is calibrated during dedicated Van-Der-Mer scans.
- AFP (ATLAS Forward Proton detector), tracking detectors also placed on Roman pots, to measure momentum and emission angle of forward protons [40].
- ZDC (Zero-Degree Calorimeter), calorimeter detecting forward neutrons and photons in both proton-proton and special heavy-ion collision runs [41].

### 1.3.2. Shielding

In addition to detector systems and associated magnets, radiation shieldings also contribute significantly to the overall experimental weight, adding up to 2825 tons. The purpose of shielding is to protect sensitive detectors from the deleterious effects of radiation and has to be specifically designed, as will be discussed in more detail in chapter 3. The main shielding components in ATLAS are illustrated in figure 1.3.3. They were optimized by taking into account the regions where most of the radiation comes from: the IP, the beam pipe, the forward calorimeter (FCal) and the TAS collimator (Target Absorber Secondaries, which prevents the first LHC quadrupole from quenching due to radiation) [42]. The main shielding components were made up of three layers, each designed to stop a specific field of the radiation environment: 1) an iron or copper layer to stop energetic hadrons, 2) a boron-doped polyethylene layer to moderate and absorb neutrons, and 3) a steel or lead layer to stop photons originating from radioisotopes created in the second layer [42]. The *moderator shielding* is placed on the front side[4] of FCal and the end-caps, which are an intense source of background radiation [42]. On their backside, the *Calorimeter shielding* (tailored blocks filling small available spaces) and *disk shielding* protect the end-cap muon inner station. The *toroid shielding* sits just behind the disk shielding and has an additional protection layer around the beam-pipe. The *forward shielding* protects the middle and outer end-cap muon

---

[4]with respect to IP.
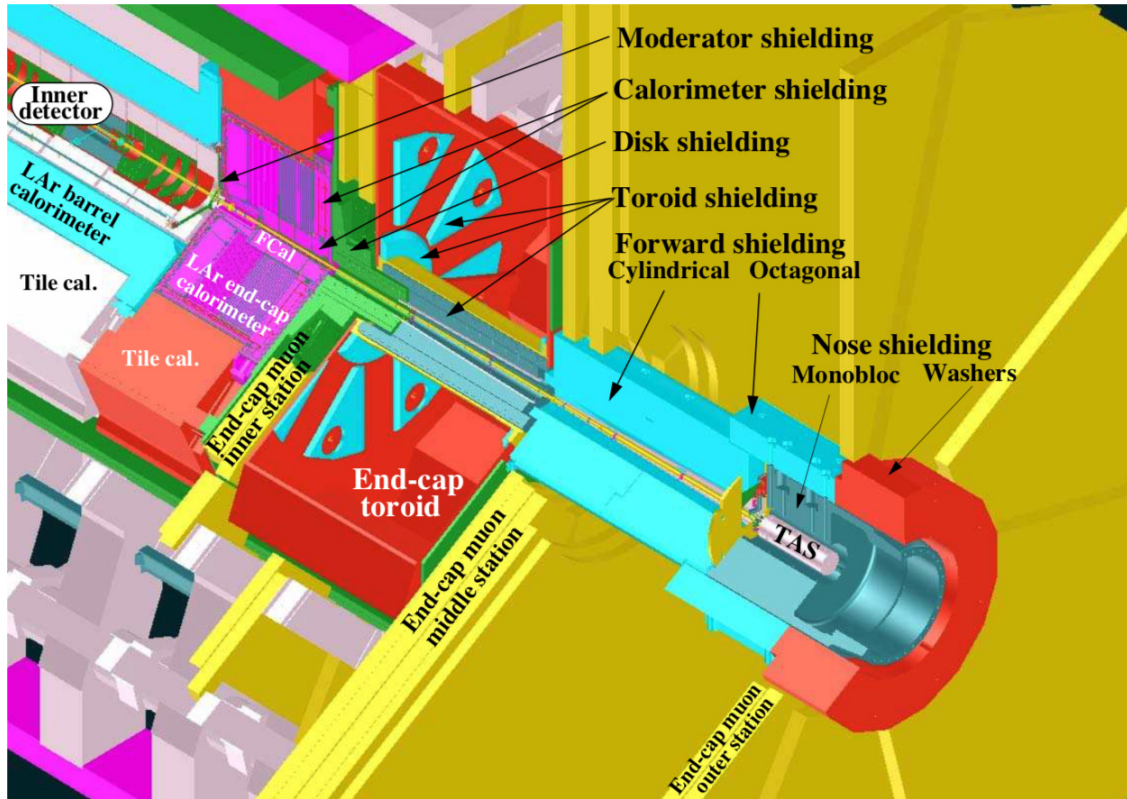
**Fig. 1.3.3.** The radiation shielding in ATLAS [**11**]. Shielding components are indicated with arrows. See text for more details.

stations from radiation originating from the beam pipe and TAS. Finally, the nose shielding is an extra protection to globally reduce the impact of radiation from the TAS on the overall experiment.

# Chapter 2

## The TPX detectors

In the 1990s, the WA97 experiment at CERN investigated the quark-gluon plasma filling the universe during the quark epoch, which lasted from $10^{-12}$s up to $10^{-6}$s after the big bang bang. To detect the products of lead-lead collisions provided by the SPS with fine spatial granularity, it was decided to develop a tracking system using a new technology. This led to the design of pixelated readout chips which can be bonded to any type of sensor (e.g. Si, GaAs, CdTe, gas), with the aim of detecting individual radiation quanta with minimal noise. This technology was called *hybrid pixel detectors*[1] [**43**]. Soon, it was realized that the concept had a potential for applications beyond accelerator experiments, for example medical imaging, radiation background monitoring or space physics. It was then that the Medipix collaboration was born, pooling the forces of several institutes aspiring to a widespread technology transfer [**44**]. Gaining a high degree of success over the years, it was decided to branch the development of hybrid pixel detectors in two directions: Medipix, a chip initially developed as a single photon counting detector with medical applications in mind, and Timepix, a general purpose chip for radiation tracking [**45**]. Among the various versions available today, three will be discussed in the context of the present thesis: Medipix2 (or *MPX2*), Timepix (*TPX*) and Timepix3 (*TPX3*). The chapter starts with a general description of radiation detection with pixel detectors and of the various readout ASICs used throughout the thesis. Then, the related physics of particle interaction in matter is presented, followed by a section on the data analysis tools used for particle tracking.

---

[1]the term *hybrid* is used in opposition to *monolithic* pixel detectors, which are produced differently: electronic chip and sensor are made out of one single semiconductor block.

## 2.1. Particle detection principles

As for many other radiation detector types, the physical feature exploited with pixel detectors is the fact that ionizing energetic particles create electron-hole pairs along their path in matter that can induce a detectable signal on electronic circuitry. A pixel detector is composed of two parts: a sensor and a readout chip. The sensor is the part sensitive to particle interactions, where charge carriers create a signal, and the readout is where the signal is shaped, allowing the physicist to perform his interpretations. A rich set of physical laws and properties encompass the working principles of the sensor, while the electronic readout design is an engineering challenge. This is thoroughly described in text books such as Ref. [**46**]. In this section, I summarize the concepts that are directly related to topics discussed in later chapters, and provide graphs illustrating the behavior of Medipix/Timepix detectors used in practice.

### 2.1.1. Charge carriers in a sensor

Charged particles interact all the way along their path in matter by Coulomb scattering with atomic electrons. The amount of scattering per unit distance, and how neutral particles can also be detected, are the subjects of section 2.3. Coulomb interactions create free electron-hole pairs within the semiconductor, or *charge carriers*, that must travel towards electrodes in order to induce a signal. This is achieved by applying a bias voltage to a customized semiconductor piece, which must have limited leakage current in order to minimize the dark signal. The most common sensors are reverse biased diodes made of silicon, while Schottky diodes or ohmic contact sensors are becoming increasingly available with compound semiconductors (e.g. CdTe, GaAs) [**47**]. A pixel detector is made by tailoring semiconductor junctions to a matrix of electrodes on one side of the sensor, that is then bump-bonded to the electronic readout (or *chip*). The other side of the sensor is covered by a common electrode, called the *backside electrode*[2]. The working principle of a pixel detector is summarized in figure 2.1.1.

When electron-hole pairs are released by a particle interaction, they start to move under the influence of competing phenomena. First, when a high charge carrier density is created,

---

[2]Note that this name can be misleading, because most of the time one puts this side of the sensor in *front* of the radiation source.

**(a)**



**(b)**



**(c)**
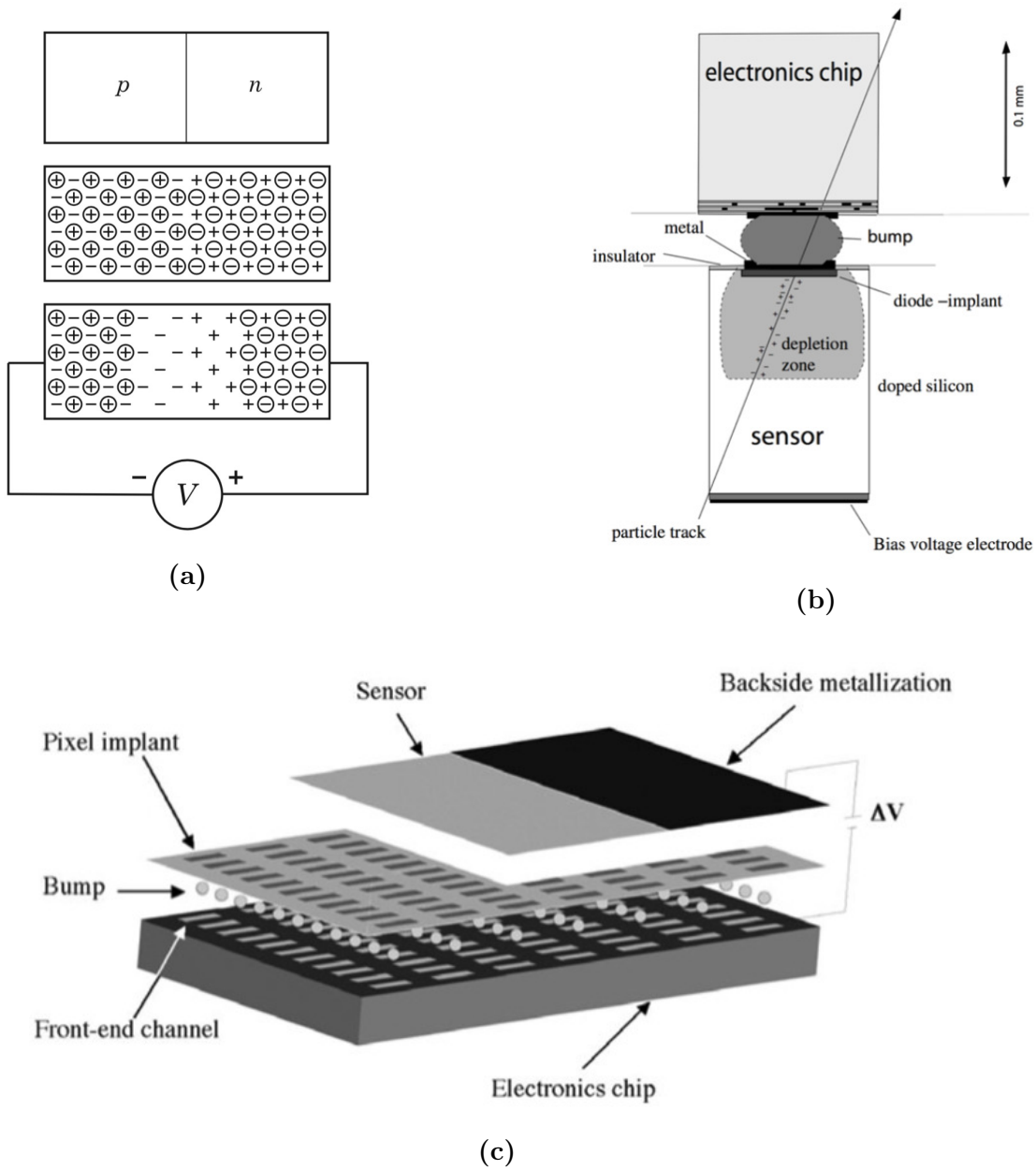
**Fig. 2.1.1.** Working principle of a hybrid pixel detector. (a) Standard silicon sensors are doped (p-type on one side, n-type on the other), creating a depletion region at the p-n junction, which must be extended by applying a bias voltage [**48**]. Sensors are then bump-bonded to a pixelated electronics chip. (b) When a particle interacts in the depletion zone of a sensor, electron-hole pairs are created, and charge carriers move toward the pixel electrodes (e⁻ towards anode, holes towards cathode) under influence of the electric field [**46**]. (c) 3D schematics of the pixel detector [**46**].

it is subjected to a *plasma* effect, delaying the signal induction [49]. This is accompanied by a *funneling* effect, describing the fact that carriers in the center of the plasma are pulled toward the collecting electrode [50]. In parallel, thermal *diffusion* of the carrier cloud and its *drift* motion under the electric field occur simultaneously, making carriers spread while they move towards the electrode. Consequently, when pixels are small, carriers can spread to the neighboring electrodes, leading to a signal on several adjacent pixels (cluster). This is called the charge sharing effect, and it has already been studied with TPX detectors [51, 52].

The drift velocity of charge carriers depends on both the carrier mobility, which varies among sensor materials, and the applied bias. A comparison of drift times in TPX sensors available in practice[3] is given in table 2.1.1. It can be noticed, for example, that GaAs has

| | | mobility $(cm^2V^{-1}s^{-1})$ | drift time (ns) for 1mm @300V |
|---|---|---|---|
| Si | e- | 1500 | 22 |
| | holes | 480 | 69 |
| GaAs | e- | 8500 | 4 |
| | holes | 400 | 83 |
| CdTe | e- | 1050 | 32 |
| | holes | 100 | 333 |

**Tab. 2.1.1.** Comparison of charge carrier drift times in a 1 mm thick sensor for different materials (see footnote in the text). Mobilities used for the calculation are taken from Ref. [53].

the fastest electron collection time, which is of interest for applications where the particle time stamp is measured. However, it is known that compound semiconductors such as GaAs and CdTe suffer from carrier trapping centers, which block carriers before they have fully induced the signal. This is explained in more details in the following section.

[3]The comparison here is given for a 300 V bias, which is slightly above typical values for Si (to avoid breakdown, i.e. when the sensor becomes conductive). On the contrary, at room temperature, TPX detectors made of recent 1 mm GaAs and CdTe sensors can usually be operated successfully up to $\sim 500$ V.

### 2.1.2. Signal induction

When charge carriers move inside the sensor, they induce a voltage pulse in the pixel electrodes, that is then amplified by the electronic circuitry of the chip. This voltage pulse does not appear at the time when the carriers reach the electrode, but rises as soon as the carriers start to move inside the sensor volume. The charge induced by a carrier moving from depth $x_1$ to $x_2$ in the sensor can be calculated from the Ramo theorem [54, 55], giving [46]:

$$Q_{(x)} = e(\phi(x_1) - \phi(x_2)) \tag{2.1.1}$$

where $e$ is the elementary charge and $\phi(x)$ the so-called *weighting potential*. Even though equation 2.1.1 looks straightforward, the calculation of the weighting potential for a pixel detector is not, and depends on the electrode geometry. Using the expression derived in Ref. [56], the weighting potential affecting a charge carrier traveling along a straight path in the center of a pixel volume, for the TPX pixel size with a standard $300\,\mu\text{m}$ thick sensor, is shown in figure 4.4.1 (c.f. publication in section 4.4). Interestingly, a consequence of this relation is that carriers induce most of the charge when they travel close to the pixel electrode, which is commonly referred to as the *small pixel effect* [57]. Moreover, it can be noted that only one carrier type (either electron or hole) significantly contributes to the signal, depending on the applied bias polarity. A last remarkable consequence is that the weighting potential for neighboring pixels also fluctuates as function of depth in the sensor, even though it starts and ends at 0, resulting in no net induced charge. Since pixel amplifiers are sensitive to voltage fluctuations (either positive or negative), they will record part of the induced voltage on neighboring pixels, thus adding an extra component to the overall signal: this is called the *transient signal* [57]. Combined with the charge sharing effect described earlier, this can result in signals spread over a large number of pixels (cluster).

For fully depleted silicon sensors, the induced charge is, to a good approximation, equal to the amount of charge carriers created by the interaction of the particle. This is not the case, however, with compound semiconductors, because they usually suffer from abundant charge carrier trapping centers. Since carriers induce the signal while they move towards the electrode, they will stop contributing when they are trapped. This results in the deterioration of energy resolution and cluster morphology, and, in the worst case, to an absent signal. To quantify this effect, an average lifetime is attributed to electrons and holes in the material,
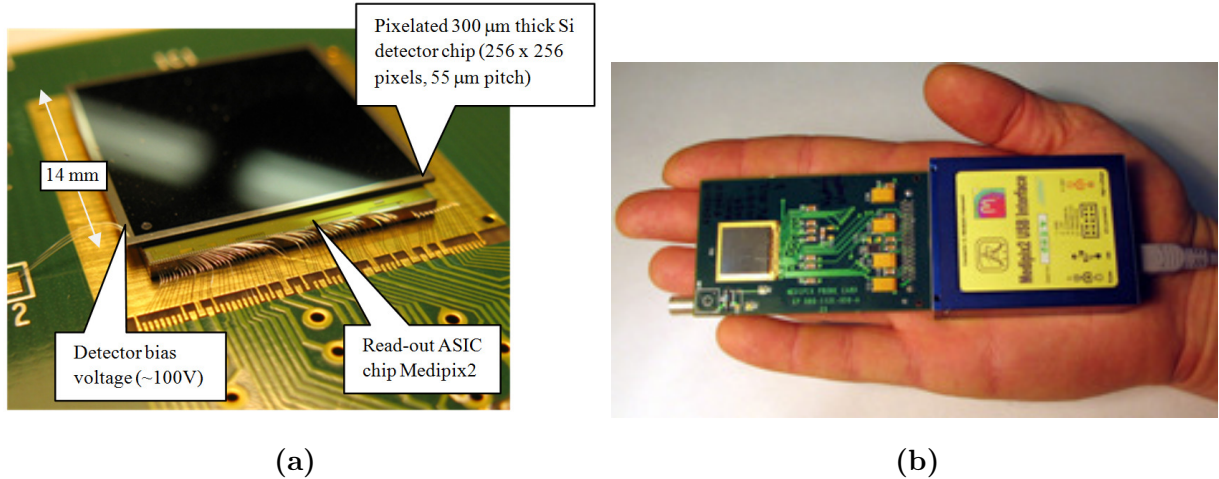
**Fig. 2.2.1.** Illustration of a MPX2 detector [**59**]. a) Description of the Medipix2 chip and its sensor. b) Photo of the whole detector with its USB interface (blue box) for connection to a computer.

representing the time during which they drift before they are trapped. When assessing the quality of a compound semiconductor, a common parameter to measure is the mobility-lifetime product ($\mu\tau$). This parameter allows one to get an estimate of the maximum sensor thickness that can be used to obtain a reasonable charge collection efficiency (CCE). The CCE is the ratio of the induced charge to the charge deposited originally by the incident particle in the sensor. It is given by the Hecht equation [**58**], which is used in practice to extract the $\mu\tau$ product of either electrons or holes depending on the bias polarity.

## 2.2. The TPX chip family

### 2.2.1. Common properties

The MPX, TPX and TPX3 chips are $2\,\mathrm{cm}^2$ ASICs subdivided into 256 x 256 pixels with a $55\,\mu\mathrm{m}$ pitch[4]. The chip is bump-bonded to a sensor, most commonly $300\,\mu\mathrm{m}$ silicon, and wired to a PCB as shown in figure 2.2.1a. The PCB is connected to a USB interface (blue box in figure 2.2.1b), allowing connection to a computer for detector control, data acquisition

---

[4]except the oldest chip Medipix1, which has not been used in the present work and is therefore not discussed here.

and visualization. The detector fits in a hand and can be easily positioned in a wide range of experiments, or integrated in larger particle tracking systems. Each pixel has its own electronic circuitry (e.g. clock, shutter, digitizer), meaning that a chip is in fact made of 65536 independent detectors. Data can be recorded in different modes depending on the chip version, as described below.

### 2.2.2. Medipix2

The Medipix2 chip is available since 2005 [**45**]. It was used in the ATLAS-MPX network (operated in 2008-2012), predecessor of the ATLAS-TPX radiation monitoring system presented in chapter 3. Pixels are active during constant acquisition time intervals called frames, which can be adjusted according to particle fluxes. Frames can be viewed as images of incoming radiation, interspersed by a dead time depending on the amount of readout data. Each pixel can count the number of times it has been hit by an interacting particle: this is called the *counting mode*. During a frame, the hit count is incremented each time the input charge induced on the pixel amplifier reaches a threshold, which can be tuned to select different energy ranges. If the acquisition time is short enough, the frame is composed of pixel clusters, each cluster corresponding to one particle interaction. This is illustrated in figure 2.2.2 with frames recorded by a MPX2 detector exposed to various sources of radiation. The cluster shape depends on the particle type, energy and direction, as will be discussed in the next section. In cases where high statistics is required, e.g. for medical imaging or luminosity measurement in LHC, one chooses a longer acquisition time to reduce the dead time. This is illustrated, in figure 2.2.3, with an X-ray image (integration of multiple frames) of mouse bones obtained with a MPX2-based detector. The detector used for this image is a matrix of 2x2 MPX2 chips connected together side by side. Here, the pixels count the number of photons that go through the mouse during the exposure time.

### 2.2.3. Timepix

With the release of TPX in 2007, it became possible to measure the energy deposited by particles in the sensor and their timestamp. While the ASIC is still based on a frame-by-frame readout, two modes of operation were added, the *TOT mode* and the *TOA mode*. ToA means *Time Of Arrival*: during a frame, when a pixel is hit by a particle, the timestamp is recorded. The reference clock can be set up to $100\,\mathrm{MHz}$ [**62**], resulting in a $10\,\mathrm{ns}$ time
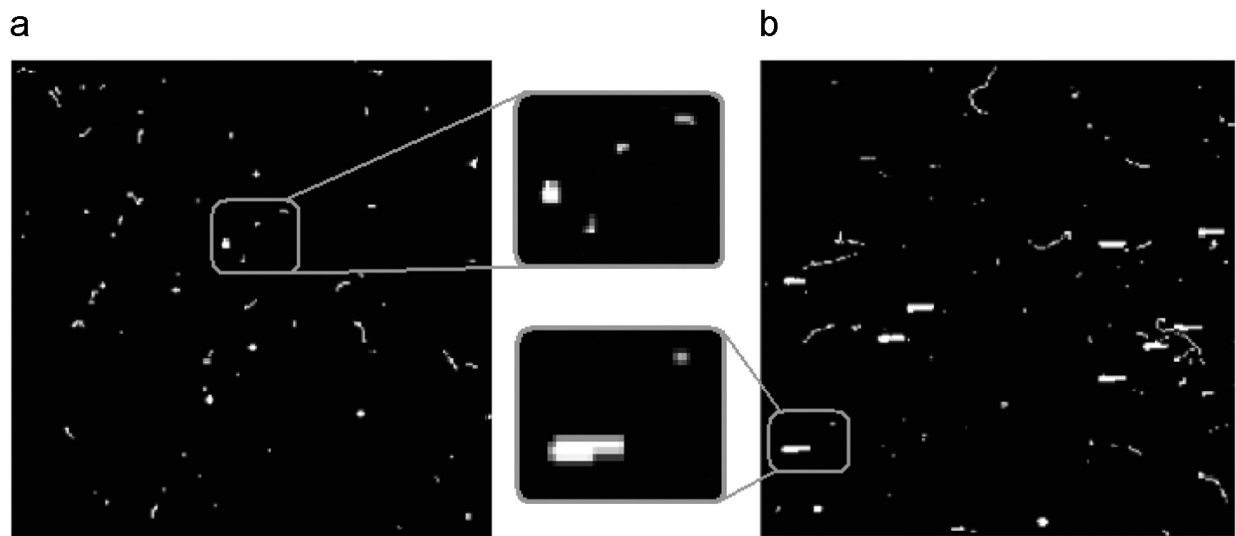
**Fig. 2.2.2.** Example of frames recorded by a MPX2 detector exposed to $^{241}$Am, $^{106}$Ru, $^{137}$Cs and 10 MeV protons at 0°(left) and 85°(right) [**60**]. Large tracks are due to protons or to 5.48 MeV $\alpha$-particles from $^{241}$Am, while thin tracks come from electrons (up to 39 keV from $^{106}$Ru) and photons (662 keV from $^{137}$Cs).
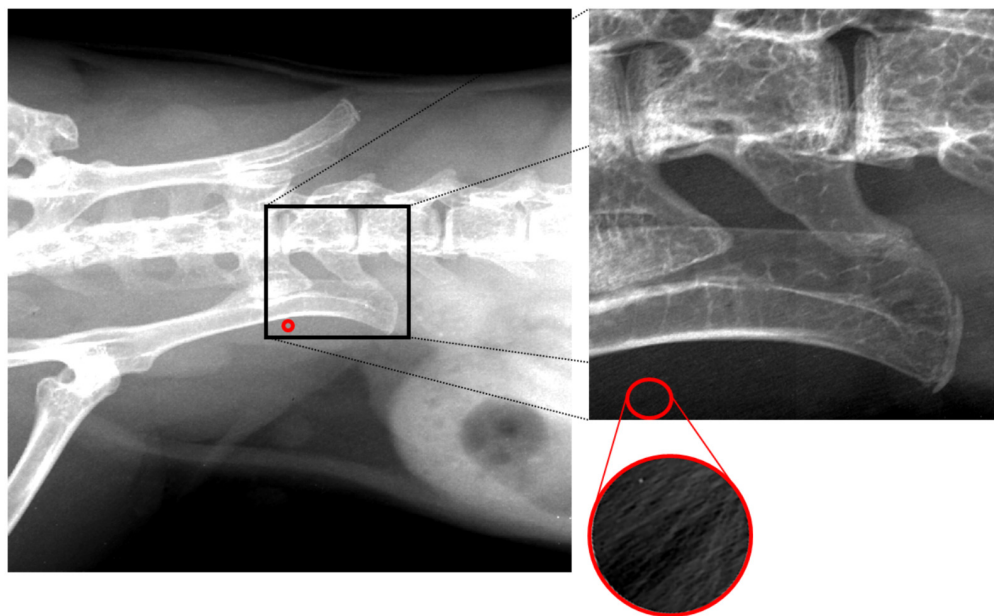


**Fig. 2.2.3.** Image of mouse bones obtained by a MPX2-based detector. The detector is irradiated by an X-ray tube [**61**], with the mouse placed in-between.

granularity[5]. TOT means *Time Over Threshold*: during a frame, each pixel records the time during which the input charge is above a predefined threshold. The higher the TOT value, the higher the energy. To obtain a good energy resolution, a standard method is to perform a per-pixel calibration using X-ray irradiation. It has been found [63] that the relation between TOT and deposited energy (E) is non-linear for energies close to the threshold (t):

$$TOT_{(E)} = aE + b - \frac{c}{E - t} \tag{2.2.1}$$

Using several X-ray sources, typically from 6 keV to 60 keV, the four parameters (a,b,c,t) can be extracted [64]. The threshold is adjustable, and is usually set to its minimum (around 3 keV for silicon sensors) for best particle tracking performance.

As for MPX2, the TPX detector can thus perform particle tracking, with either its counting, TOT or ToA mode. Nevertheless, the TOT mode adds a significant advantage compared to MPX. Indeed, with this mode, pixel clusters contain the deposited energy and can be represented with a third dimension, as shown in figure 2.2.4. This allows to achieve sub-pixel spatial resolution, stopping power measurements and better particle categorization, as will be discussed in the next section. The TPX chip is the technology used in the ATLAS-TPX network, which is the topic of chapter 3.

### 2.2.4. Timepix3

TPX3 is currently the latest available version of the Timepix family, even though its successor, TPX4, has already been announced [67] and should be released soon[6]. TPX3 has been tested in 2018 in ATLAS and will be replacing ATLAS-TPX for LHC Run-3. The chip has the same operational modes as TPX but comes with new features. From a physics point of view, the noticeable improvements are the following [68]:

- Pixels can be active continuously, without frames and related dead time (*data driven readout*).
- The TOT and TOA modes can be used simultaneously.
- Timing resolution reaches 1.56 ns.

---

[5]The time resolution is actually lower due to a time-walk effect affecting every pixel [62]. It stays in the order of tens of ns, though.

[6]The main expectations with TPX4 are a smaller pixel pitch and better time granularity [67].
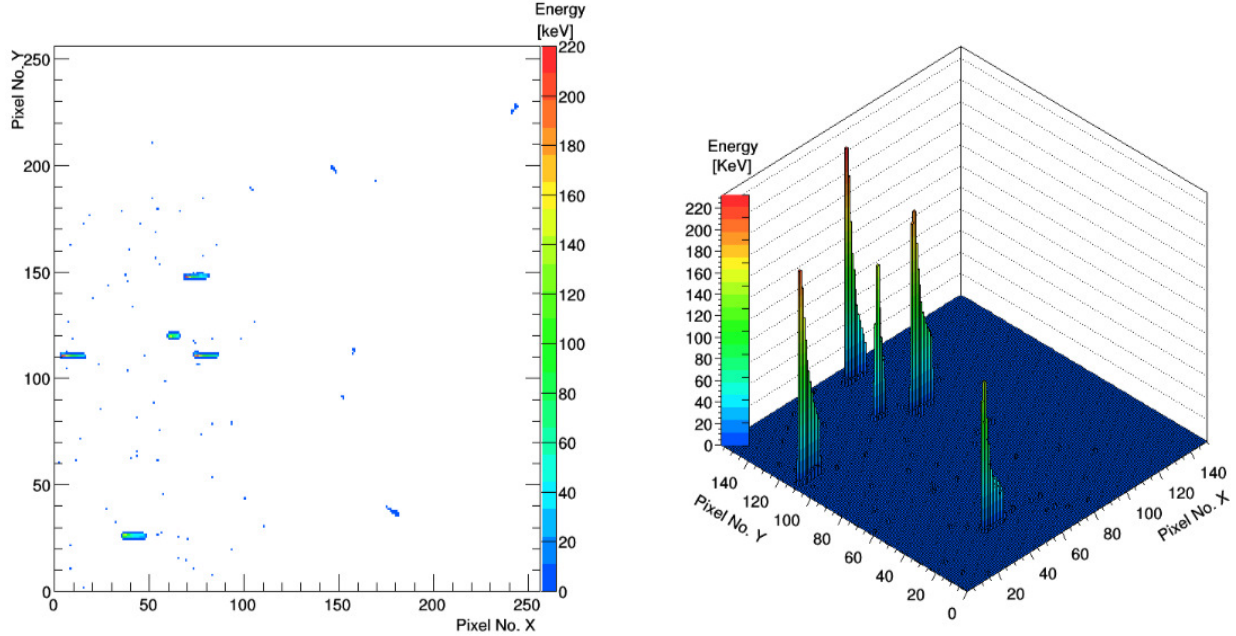
**Fig. 2.2.4.** Example of frame recorded with a TPX detector exposed to $^{241}$Am, $^{106}$Ru, $^{137}$Cs and 10 MeV protons at 75° [**65, 66**]. The frame is not full of clusters due to the positioning of the detector compared to the beam and sources. In contrast to figure 2.2.2, the frame has a third dimension (represented in color on the left, and with 3D view on the right), thanks to the TOT mode of the TPX chip.

These features push the pixel detector technology to another level and open new doors for applications. They allow, for example, the reconstruction of charged particle path in the sensor, similarly as with time projection chambers, allowing a fourth dimension to cluster representation. This is illustrated in figure 2.2.5 with a MIP (Minimum Ionizing Particle) and delta electron trajectory in a Si sensor [**69**]. Of interest for ATLAS-TPX upgrades, the improved timing resolution allows to keep track of LHC bunch crossing time, as will be discussed in chapter 3. Finally, TPX3 brings the possibility to develop Compton cameras, a technology where algorithmic methods had already been developed for years but where appropriate hardware were missing. Compton cameras allow the localization of gamma sources and could be part of the ATLAS-TPX upgrade. They require high-Z sensors and will be discussed in chapter 4.

21
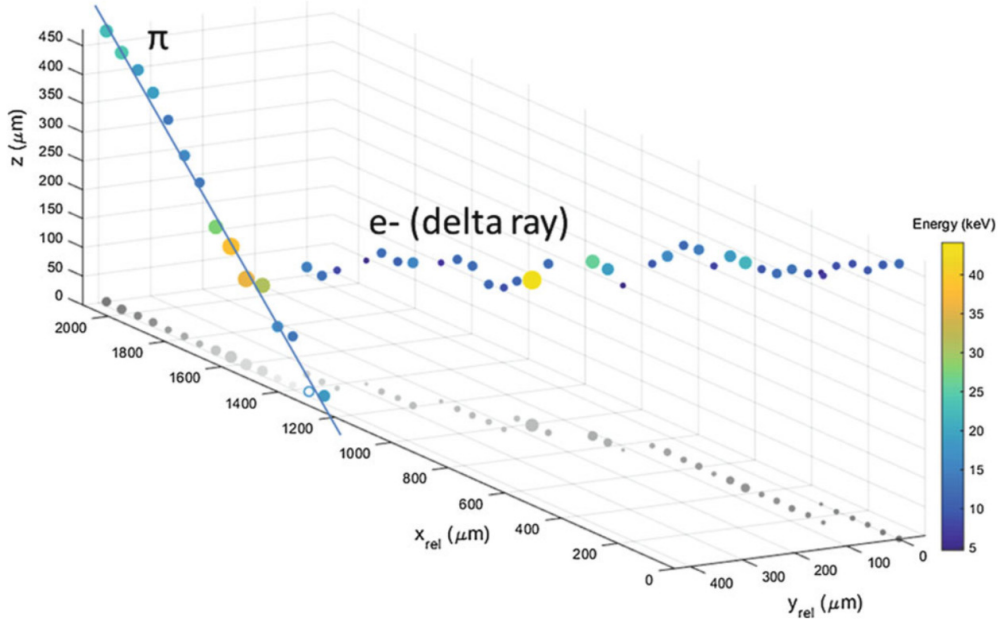
**Fig. 2.2.5.** 120 GeV/c pion track with ejected delta ray recorded by a TPX3 detector [**69**]. In contrast to figure 2.2.4, the cluster can be represented with a fourth dimension (z-coordinate of the particle trajectory) due to the simultaneous TOT and TOA operation of the TPX3 chip.

## 2.3. Particle interactions in sensors

In order to analyze the data recorded by pixel detectors, a good knowledge of particle interactions in semiconductors is necessary. This is a complex topic and has been studied both theoretically and experimentally for decades. As literature is abundant (see, for example Ref. [**70, 57, 71**]), I only outline features directly related to pattern recognition techniques used with detectors of the Timepix family.

### 2.3.1. Charged particles

As mentioned earlier, charged particles deposit energy by ionizing matter along their path. For particles heavier than the electron, such as hadrons, muons or pions, the energy loss per unit distance (also called stopping power, or simply dE/dx) is described by the Bethe-Bloch formula [**70**]. The stopping power depends on the material properties, as illustrated in figure 2.3.1a with different TPX sensor materials. It can be observed in this figure that protons and pions have clearly distinct dE/dx for a given material. This is due to their
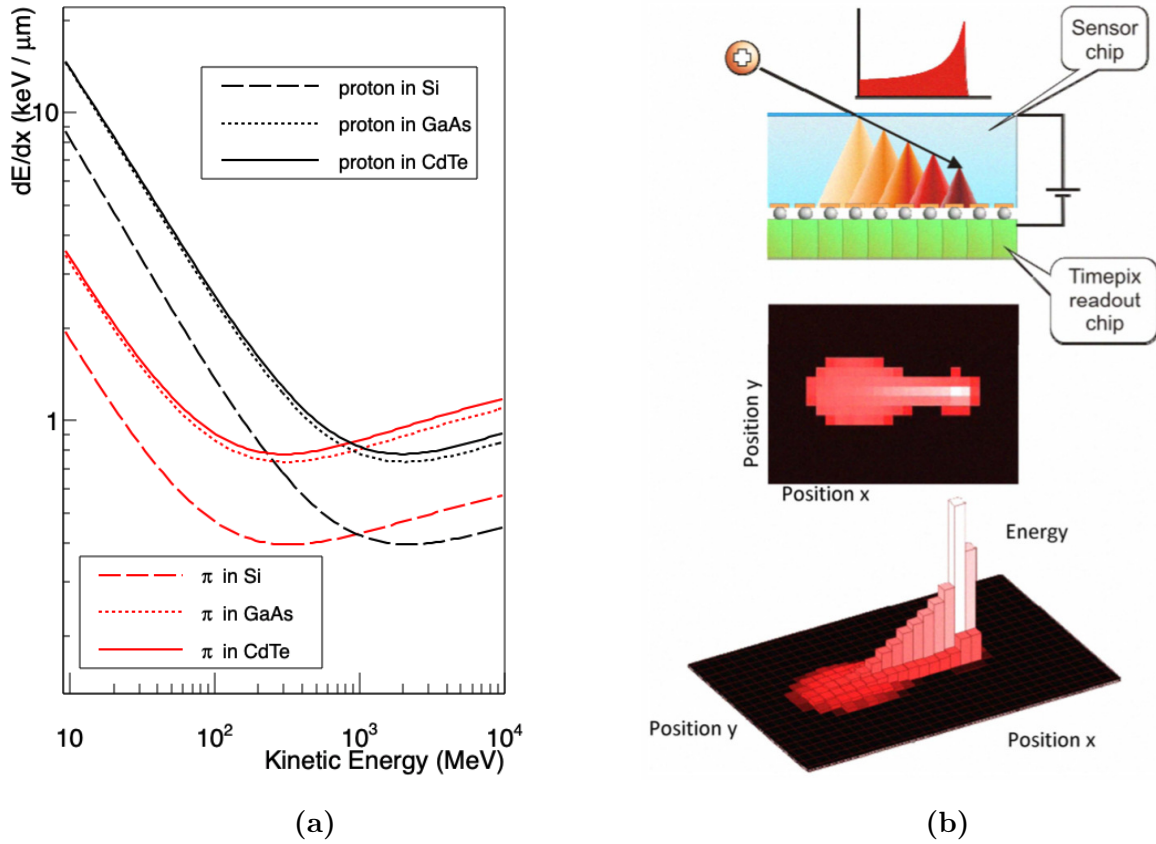
**Fig. 2.3.1.** (a) Energy loss of heavy charged particles in different sensor materials. The stopping power (dE/dx) is calculated using the Bethe-Bloch formula [18]. Multiplying the y-axis by 55 μm, one gets an idea of the deposited energy per pixel if the particle is parallel to the sensor surface. b) Illustration of energy loss measurement by a TPX detector [72]. Here, a heavy charged particle is stopped in the sensor. The measured track reproduce the Bragg curve (shown on the very top).

different masses, and can be exploited with TPX detectors to distinguish incoming particles. When these *heavy* charged particles have low energy (few MeV), they are stopped in the sensor and the dependence of dE/dx on depth is described by the so-called Bragg curve [70]. This is illustrated in figure 2.3.1b with a TPX track measured in TOT mode (see the Bragg curve on the very top). At higher energies, when they are close to their MIP energy range, heavy charged particles go through the sensor with straight trajectories and constant dE/dx.
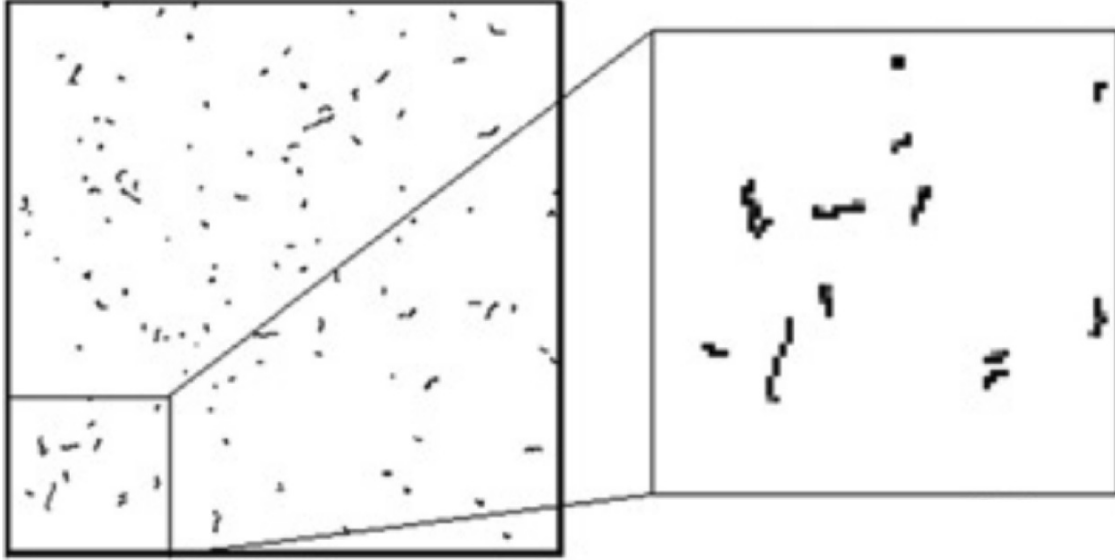
**Fig. 2.3.2.** 2D projections of electron trajectories recorded by a TPX detector irradiated with a $^{90}$Sr/$^{90}$Y radioactive source [**73**].

For electrons and positrons, the Bethe-Bloch formula must be accompanied by a term representing radiative losses (Bremsstrahlung), which starts to dominate above few tens of MeV [**70**]. Moreover, since they have the same mass as atomic electrons, they are deflected when they travel in sensors. Hence, in pixelated detectors, these particles do not usually leave straight clusters, contrary to heavy charged particles. This can be seen in figure 2.3.2 with measured electrons emitted by a $^{90}$Sr/$^{90}$Y radioactive source (end-point energy of 2.28 MeV) [**73**]. It is also important to note that in the MeV energy range, and below, electrons have short penetration ranges in matter and can therefore be easily stopped in detector casings. To illustrate this, simulations of electron beams directed at a TPX detector with similar casing dimensions as ATLAS-TPX detectors are shown in figure 2.3.3a. Here, it can be observed that 2 MeV electrons are stopped in the casing (green layers on the left) before they interact in the sensor (last gray layer on the right). At 5 MeV, they go through the sensor, and leave curly tracks as shown in the example frame of figure 2.3.3b (left). Finally, it is only above few tens of MeV that electrons go through the sensor linearly and that, consequently, the recorded tracks (figure 2.3.3b, right) start to look like other charged particle tracks (e.g. protons, muons, pions) in their MIP regime. As will be seen in

**2 MeV**

**5 MeV**          **50 MeV**

**(a)**

**5 MeV**          **50 MeV**
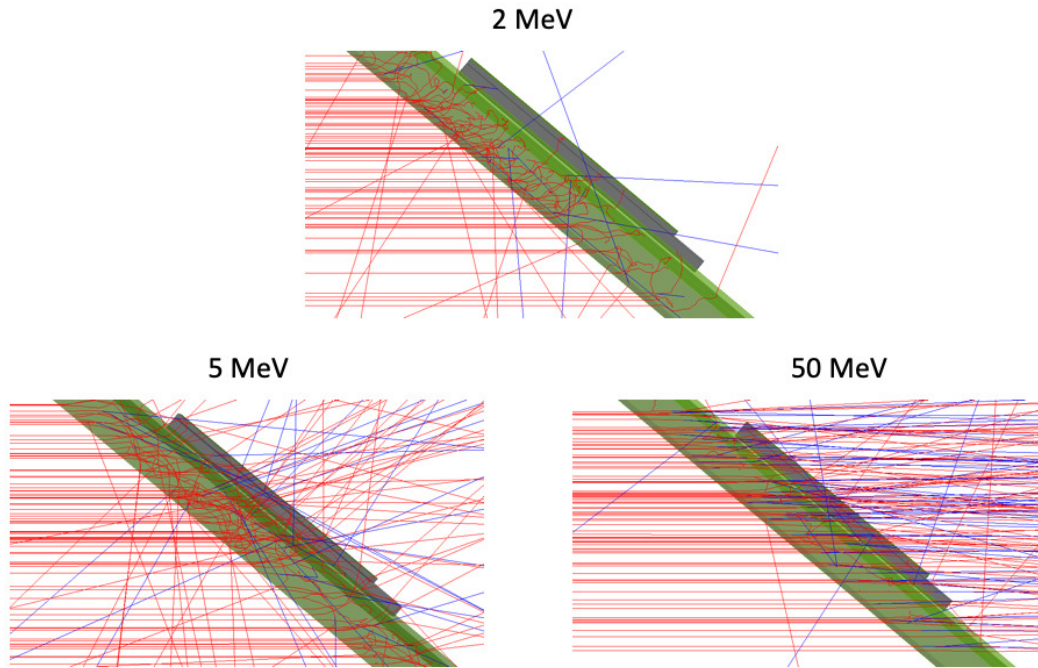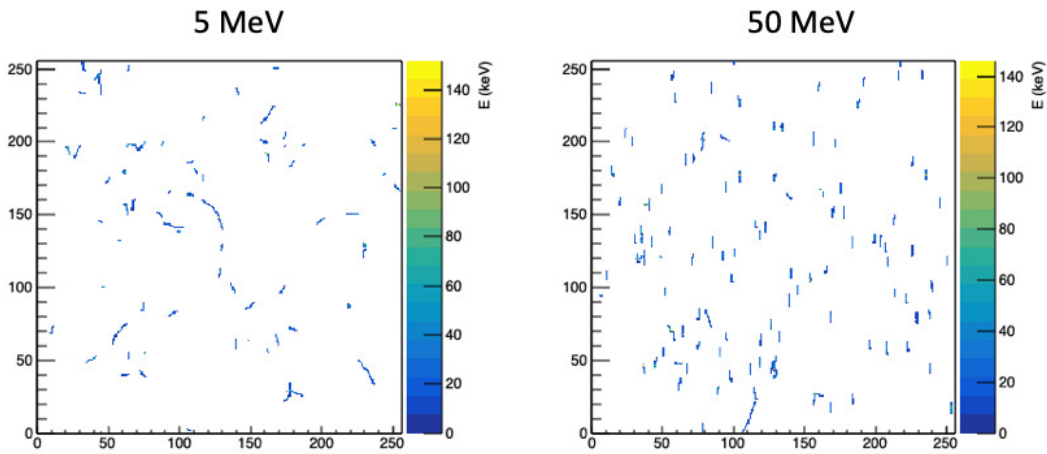
**(b)**

**Fig. 2.3.3.** (a) Simulations of a 2, 5 and 50 MeV electron beam directed at a TPX detector, equipped with a similar casing than ATLAS-TPX detectors. The detector is irradiated from the back (left side on the pictures), to show the effect of the casing on electron trajectories (red lines). The silicon sensor is the last gray layer on the right, and blue lines represent photons emitted by Bremsstrahlung. (b) Example frames of the 5 MeV and 50 MeV beams, showing the 2D projection of electron trajectories in the sensor. Simulations were performed using the Allpix2 framework [**4**].

chapter 3, electrons of the ATLAS radiation environment are mostly below the MeV range, therefore they are rarely detected by the ATLAS-TPX detectors.

### 2.3.2. Photons

Neutral particles do not ionize matter along their path. They interact through specific processes, emitting one or more charged particles that can then be detected. In the context of ATLAS-TPX, photon spectra from the radiation background (see chapter 3) are such that only the photoelectric effect and Compton scattering have a significant contribution to the detected events. The dominance of each process depends on the photon energy and the atomic number of the sensor material, as illustrated in figure 2.3.4. Photoelectric absorption and Compton scattering result in the ejection of an atomic electron inside the TPX sensor volumes, thus leaving similar tracks as those illustrated in figure 2.3.2. Consequently, there is no observable difference between photons and electrons with TPX detectors, except that photons have a lower detection efficiency. This will be discussed further in chapter 4.

### 2.3.3. Neutrons

As for photons, neutrons are not detected directly in semiconductor detectors. But in contrast to the electromagnetic interactions of photons, they interact with matter through the strong force and require different sensitive materials. Unfortunately, their cross section with silicon is small, as shown in figure 2.3.5a for a broad energy range. Since the choice of sensors that can be bonded to the TPX chip family is limited, one solution is to position thin material layers that are more neutron-sensitive on top of their surface (*neutron converters*). For example, thermal neutron detection with MPX2 detectors have been investigated by assessing several converter materials such as $^6$LiF or amorphous $^{10}$B [77], exploiting the neutron absorption reactions of $^6$Li and $^{10}$B atoms. The corresponding cross sections and nuclear reactions are shown in figure 2.3.5b. Comparing figures 2.3.5a and 2.3.5b, it can be seen that the thermal neutron cross section (at $0.025\,\mathrm{eV}$) on $^6$Li is three orders of magnitude higher than on Si, clearly indicating the advantage of adding the converter layer on top of the Si sensor. The triton ($2.73\,\mathrm{MeV}$) and $\alpha$ ($2.05\,\mathrm{MeV}$) particles emitted after $^6$Li absorption have short ranges in Si and leave distinguishable signals, as will be discussed in the next section.
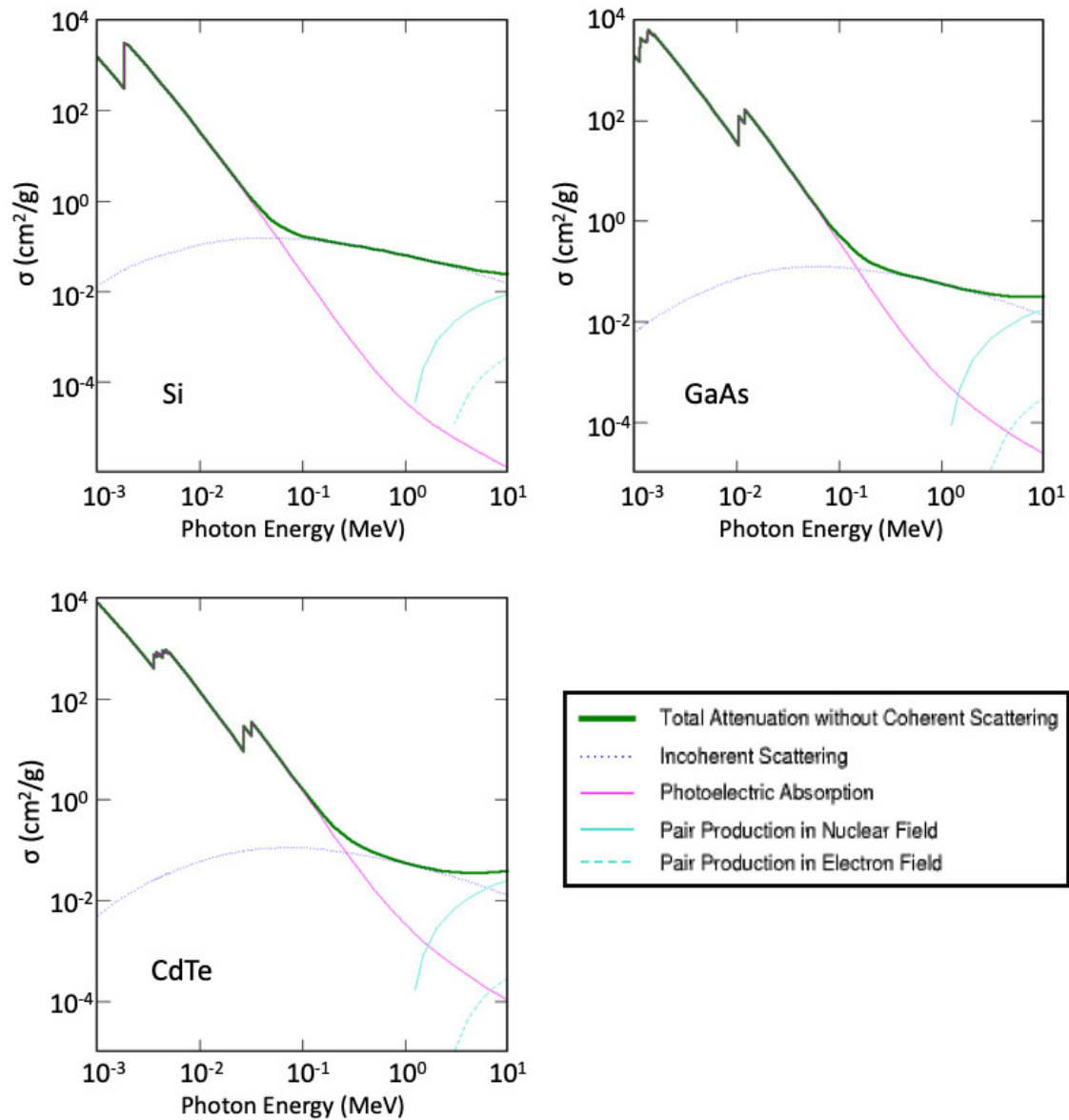
**Fig. 2.3.4.** Cross section of photon interactions in TPX sensor materials as a function of energy [**74**].

## 2.4. Data analysis tools

The TPX chip segmentation allows one to identify several properties of the interacting particles, by means of track recognition algorithms. First, I describe algorithmic methods used in the publications of chapters 3 and 4, and then discuss publicly available softwares for data analysis with TPX detectors.
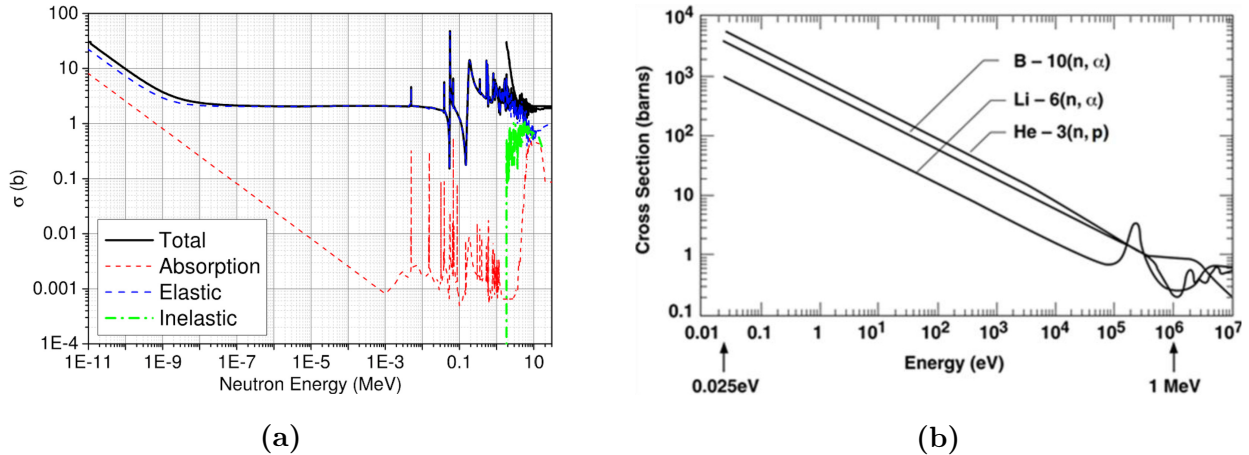
**Fig. 2.3.5.** (a) Cross section of neutron interactions in silicon [**75**]. For comparison with photon cross sections in Si given in figure 2.3.4, the y-axis here must be divided by 50 to obtain $\sigma$ in cm$^2$/g. (b) Cross section of neutron absorption in different materials [**76**].

### 2.4.1. Pattern recognition algorithms

Track recognition is done by exploiting information from each pixel: binary information with MPX2 (hit or no hit), energy or timestamp with TPX, and energy + timestamp with TPX3. Meaningful information can be obtained just by looking at a cluster's two-dimensional shape: particle type, direction or even energy range. The first pattern recognition methods were developed with MPX2 chips, and can still be used with TPX and TPX3 since all chips have the same pixel geometry. A reference paper where cluster shapes were categorized into six categories was published in 2011 (Ref. [**60**]), mainly using data from the UdeM Tandem accelerator. These categories cover all detectable particles from mixed radiation fields such as in ATLAS, and are illustrated in figure 2.4.1. To perform the classification, the algorithm extracts several geometrical properties of the clusters, such as their size, roundness or length. Since the charge sharing effect results in large clusters for high energy deposits (see section 2.1), highly ionizing particles (e.g. protons or ions at relatively low energy) can be easily distinguished from the rest (e.g. electrons, MIPs). They leave *heavy tracks* or *heavy blobs*, which will be referred together as *High Energy Transfer Events* (HETEs) in the following text. HETEs are also the trace of neutrons after their interactions in converters. When they hit the sensor surface non-perpendicularly, MIPs are easily distinguishable too, because they leave thin *straight tracks* with length depending on inclination. On the other

28

**Fig. 2.4.1.** Cluster categories defined in Ref. [**60**], from investigations with MPX2 detectors. See text for more details.

hand, electrons and photons can leave *dot*, *small blobs* or *curly tracks*, in order of increasing energy. Finally, it should be added that perpendicular MIPs can also leave dots and small blobs, or even curly track when they eject a $\delta$-ray.

This categorization has been extensively used with MPX2 detectors in the past years for radiation field studies, and it can be improved when using TPX detectors. Indeed, the TOT mode allows for dE/dX measurements, which can be used to distinguish charged particles in mixed radiation fields. Moreover, this mode reveals two distinctive parts in a HETE cluster: a track core with high energy values, and a surrounding halo due to charge sharing and $\delta$-rays. This can be used, for example, to reach sub-pixel resolution when measuring particle impact points [**78**].

### 2.4.2. Particle direction and dE/dX

Knowing the sensor thickness, the 2D trajectory profile of MIPs and HETEs allows for reconstructing their incident angles. This is illustrated in figure 2.4.2. For straight tracks, the projected length can simply be taken as the maximum distance between two pixels in the cluster. For HETEs, the halo can be first removed with an energy threshold to improve the precision (possible with TPX and TPX3, but not with MPX2). Once the incident angles have been determined, the distance traveled by the particle in the sensor is easily calculated

29
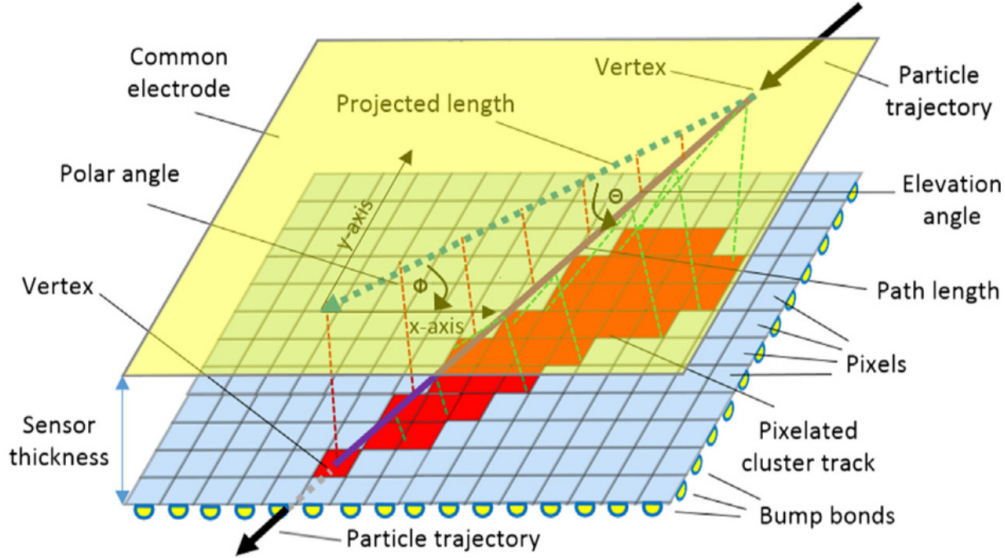
**Fig. 2.4.2.** Reconstruction of incident angles using the track shape [**79**].

using the sensor thickness. However, it cannot be determined whether the particle comes from the front- or the backside and whether the azimuth is $\phi$ or $\phi+180°$ (c.f. figure 3.3.4 in the publication of section 3.3). Dividing the cluster *volume* (energy summed over the pixels forming the cluster) by the distance traveled by the particle in the sensor, one obtains the electronic stopping power (dE/dx), also termed the *Linear Energy Transfer (LET)*. This parameter is useful for characterizing charged particles in mixed radiation fields, as will be discussed in chapter 3.

### 2.4.3. Neutron detection

As discussed earlier, an approach for neutron detection is to position, on top of the semiconductor sensor, converter materials that are more neutron-sensitive than the sensor, and that result in signals distinguishable from gamma signals. This was tested with MPX2 detectors, using LiF foils for thermal neutrons and low density polyethylene (PE) for fast neutrons. Thermal neutrons are absorbed through the $^6$Li(n,$\alpha$)$^3$H reaction, ejecting one triton and one alpha particle that are recorded as HETEs by the detector. Fast neutrons, on the other hand, hit atoms in the PE layer, resulting in recoiled protons (and C ions, to a lesser extent) with sufficient energy to reach the sensor, which are also detected as HETEs. To separate the thermal component from the fast component in the signal, an idea is to

split the sensor surface with different neutron converter areas. In addition, one area can be left uncovered, to exclusively record the (rare) neutron interactions in silicon, such as $^{28}$Si(n,p)$^{28}$Al or $^{28}$Si(n,$\alpha$)$^{25}$Mg. These reactions represent a background to the technique and can thus be subtracted to fluences in other areas, giving a net neutron signal. This method was applied in ATLAS with MPX2 detectors (2008-2012), and later with TPX detectors (2015-2018).

### 2.4.4. Timepix hodoscopes

To improve the tracking capabilities of pixel detectors, it is common to stack them into hodoscopes[7], taking advantage of their fine segmentation. This is commonly done in tracking systems of accelerator experiment, but also for beam monitoring or space physics [80, 81, 82]. An hodoscope was used for radiation monitoring with the ATLAS-TPX network (see chapter 3), combining the design with neutron converters to make a versatile detector measuring simultaneously charged particles, photons and neutrons. Since TPX detectors can either operate in TOT or TOA mode, one cannot take advantage of simultaneous energy measurement, allowing dE/dx determination, and cluster timing, helping to reconstruct the particle track through the different layers of the hodoscope. However, since the particle incident angles can be determined, its trajectory can be extrapolated and it can be verified whether the particle induce coincident clusters in the different layers of the hodoscope. With TPX3, this problem does not occur since TOT and TOA modes can be used simultaneously, making the chip more efficient for hodoscopes.

### 2.4.5. Data analysis tools

Because of the extensive adjustability of the TPX chip and the amount of information present in the recorded data, sophisticated softwares are required for detector operation and data analysis. While detector operation can be performed using commercial softwares [83], one typically needs to write his own program for data analysis.

For the study presented in chapter 3, the data was available in ROOT format [2], sorted on a cluster-by-cluster basis. To analyze this data, I developed a C++ based program[8] using the pattern recognition algorithms illustrated in figure 2.4.1. On top of these algorithms, I

---

[7]The term *telescope* is also used in literature

[8]available in Ref. [7]

added several selection criteria for coincidence determination between the two layers of the TPX hodoscope (more details are available in the publication). Moreover, this study required Monte Carlo simulations to validate the developed methods. For this purpose, I used the Allpix2 simulation framework [4], a publicly available software based on C++, ROOT and the Geant4 simulation package [3]. For the work presented in chapter 4, the analysis was done using a framework for MPX/TPX detectors developed at UdeM called MAFalda [5]. This framework, based on C++ and ROOT, is also a publicly available tool. It has been used for several published works [84], and allows a quick and easy integration of cluster algorithms for specific analysis.

It is worth to mention that, even though they were not tested in the present thesis, machine learning algorithms tools are being increasingly used in particle physics. Recent studies have started to appear in the literature related to TPX technology, where these tools are tested for general purpose [85] or for specific applications [86]. The principle of machine learning is to choose an algorithm adapted to the task (e.g. particle tagging), define parameters of interest (e.g. cluster volume, size, etc) and feed data (measured or simulated) to *train* the algorithm. Then, the trained algorithm can be used to analyze new data. Such tools could improve particle identification and the extraction of properties, and help filtering hardware-related issues such as noisy pixels or other data acquisition dysfunctions.

# Chapter 3

---

# Radiation field characterization with ATLAS-TPX

## 3.1. Context

During the design phase of an accelerator physics experiment, in particular, it is necessary to predict the radiation environment and associated adverse effects that will be generated by collisions on the detector. This is of primary importance for background evaluation in physics analysis and for estimation of sensors and electronic components lifetime. Moreover, the induced radioactivity puts constraints on detector maintenance, for instance when dead components of detector parts need to be replaced or when system upgrades must be performed. In modern experiments, a consistent knowledge of the radiation environment can be obtained using standard particle transport codes, such as Geant4 [3] or Fluka [87, 88]. These Monte Carlo simulation tools make use of cross section data bases and particle interaction models obtained both experimentally and phenomenologically, and have been developed through several decades of experience. Due to their importance on physics goals and detector operation, an extensive effort is usually dedicated to simulations. For ATLAS, first predictions of the radiation field were reported about twenty years before the start of operation, playing a major role in the design of the detector and its radiation shielding [9, 10]. Currently, this work is continued by a dedicated team [89], which provides detailed predictions in view of future upgrades.

Once the experiment is in operation, it is necessary to assess predictions of the radiation environment with actual measurements. Indeed, simulations are affected by various sources of uncertainty and can differ from actual radiation levels [8]. A precise knowledge of the

deposited dose at an early stage is important to properly anticipate radiation damages to detectors [90]. The comparison of simulations with measurements furthermore permits precise adjustments of detectors calibration factors and thresholds [11]. In ATLAS, several detectors are specifically dedicated to the monitoring of various quantities of interest, at different locations in the experiment. For example, field-effect transistors, p-i-n diodes and bipolar transistors are used to monitor the total ionizing dose (TID), 1 MeV (Si) neutron equivalent[1] and thermal neutron fluences, respectively [90]. The leakage current in the ATLAS pixel detector is also an actively monitored quantity [92]. While a special emphasis is made on the inner detector, which is the system most exposed to radiation damage [93], the calorimeters and muon system have also been equipped with several radiation monitors [11, 94].

The aforementioned detector types are standards in the field of radiation monitoring (see, for example, Ref. [95] for a comprehensive list of solid-state radiation monitors). However, the measured units require empirical calibrations that add a possible source of discrepancy when comparing measurements with simulations. Moreover, they are generally installed at specific locations in ATLAS, resulting in a localized and restricted overall view of the radiation environment. In order to extend the field of view and take advantage of more recent technology, IEAP[2] and GPP[3] decided in 2006 [96] to install a network of Medipix detectors spanning most of the ATLAS experiment. This network, so-called ATLAS-MPX, was based on the Medipix technology (see chapter 2) and operated during the LHC Run-1. The main advantage of such detectors for this type of investigation is their ability to measure radiation on a track by track basis, and to categorize incident particles according to their type, incidence and energy range. This allows the possibility of benchmarking the simulated radiation directly, without the need to convert particle fluences to other units. During the first LHC long shutdown (2013-2014), the ATLAS-MPX network was upgraded to the ATLAS-TPX network. This new network was installed at similar locations than ATLAS-MPX but took advantage of the more recent Timepix chip. As depicted in figure 3.1.1, each detector unit was composed of two Timepix chips facing each other with neutron converters

---

[1]This unit is used to normalize the expected radiation damage caused by any radiation environment to the equivalent damage that would result from a 1 MeV neutron fluence. It concerns only non-ionizing energy losses and can be directly measured by p-in-n diodes [91].

[2]Institute of Experimental and Applied Physics in Prague

[3]Groupe de Physique des Particules, Université de Montréal
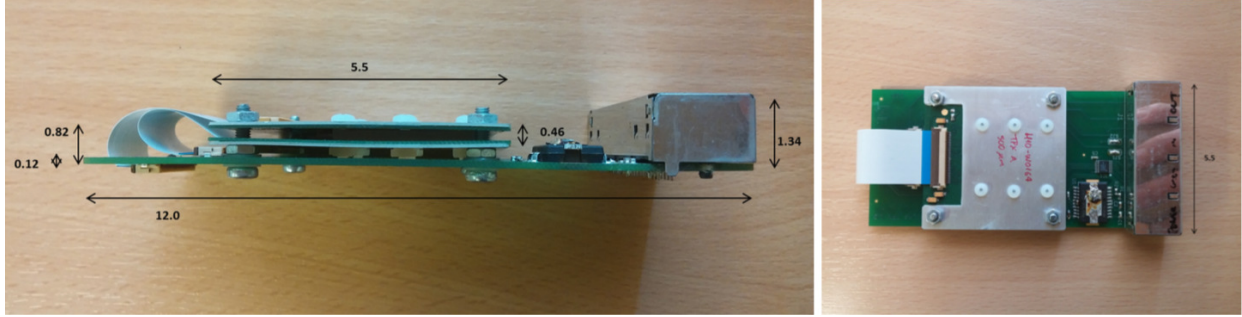
**Fig. 3.1.1.** Picture of an ATLAS-TPX detector.

in-between (hodoscope design), improving the tracking capabilities of the network. Based on standard pattern recognition techniques developed at GPP and IEAP during the last decade, a new set of algorithms had to be developed for the ATLAS-TPX detector design. This is summarized in the following section, and presented in more technical terms in the publication.

## 3.2. Methodology

Each ATLAS-TPX detector is sensitive to all types of radiation in ATLAS: photons, neutrons and charged particles. The objective is to categorize the recorded tracks and, for each particle type, extract possible properties. The results can then be used to benchmark the corresponding aspects of simulations. To give a first idea of the radiation environment, the proportion of different particle types hitting one detector (TPX01) of the ATLAS-TPX network is shown in figure 3.2.1, as obtained from simulations.

### 3.2.1. Energetic charged particles

The major development presented in the following paper concerns the energetic charged particle field. As can be seen in figure 3.2.1, the charged component of the radiation environment is mainly composed of protons, muons, pions and electrons. Simulations also show that heavy charged particles ($m \gg m_e$) have high energy ranges[4], while electrons rarely exceed the MeV range (see figure 3.2.2). In these energy ranges, heavy charged particles go through the ATLAS-TPX sensors with straight directions, as is typical for MIPs[5]. In contrast, electrons

---

[4]$m_e$ = electron mass = $511 \, \text{keV}/\text{c}^2$

[5]For this reason, we will encompass these particles under the term MIP in the present context.
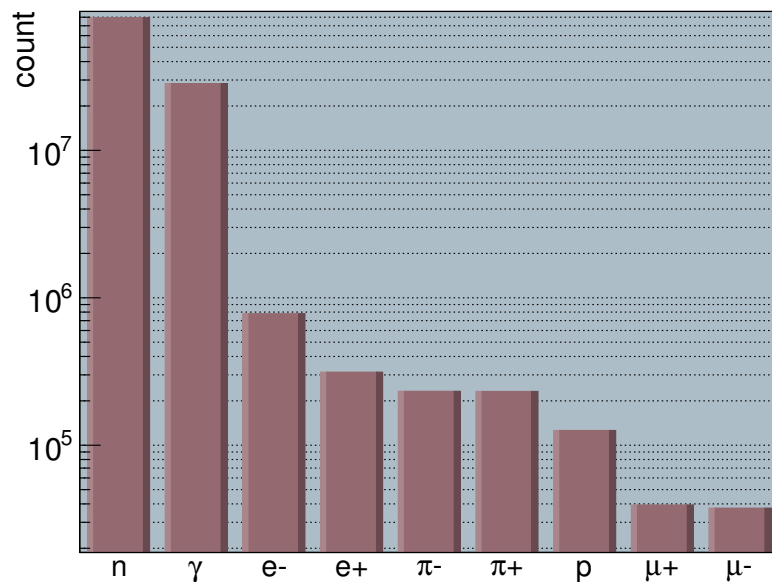
**Fig. 3.2.1.** Proportion of radiation field components in the region of the TPX01 detector (see table 3.3.1 for detector position in ATLAS), as obtained from simulations [**97**]. The y-axis is the number of particles hitting the TPX01 region for $10^5$ proton-proton collisions. To increase statistics, the detector region is taken to be a cut-away ring of the ATLAS cylinder where TPX01 is placed, assuming that radiation fluences are symmetrical around the longitudinal axis. Hence, the particle count is higher than the one actually measured by TPX01 for the same number of proton-proton collisions.

at few hundreds keV will be stopped in the detector casing, while the remaining few at higher energies will mostly have randomly curved trajectories (see chapter 2), being categorized as curly tracks.

In the publication, pattern recognition techniques adapted to the hodoscope design were established in order to extract stopping power and directions of detected MIPs. Because of the flat rectangular shape of Si sensors bonded to the Timepix chips, the probability that a MIP hits the sensitive volume depends on its direction. Indeed, a MIP arriving parallel to the sensor surface has less chance to hit the sensor than a perpendicular MIP, which faces the full $2\,cm^2$ area. To account for this effect, measured MIP fluences were normalized to
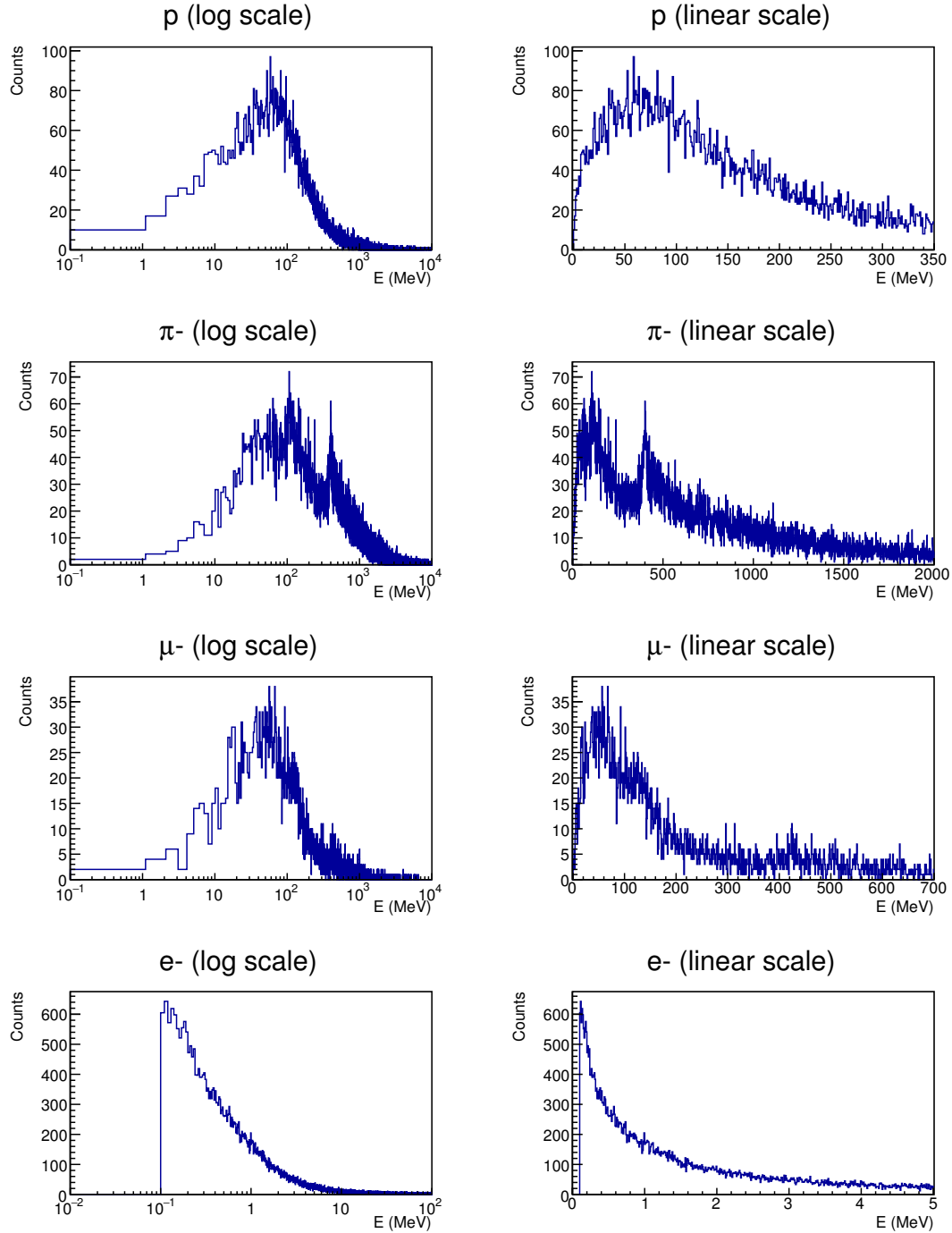
**Fig. 3.2.2.** Spectra of charged particles hitting the location of TPX01 in ATLAS (see table 3.3.1), as obtained from simulations [**97**]. On the left spectra, the x-axis is in logarithmic scale. Note the different x-axis range between heavy charged particles (protons, muons, pions), where 1 bin = 1 MeV, and electrons, where 1 bin = 10 keV.
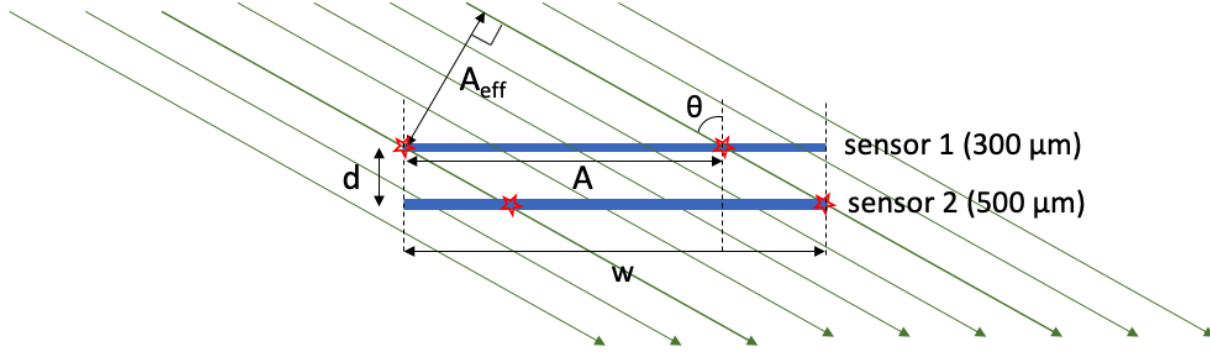
**Fig. 3.2.3.** Side view illustration of the ATLAS-TPX effective area used for the measurement of MIP fluences. $\phi$ cannot be indicated on side view, see figure 2.4.2.

the effective area $(A_{eff})$, defined as:

$$A_{eff} = A \ \cos\theta$$

$$= (w - d \ \tan\theta \ |\cos\phi|)(w - d \ \tan\theta \ |\sin\phi|)\cos\theta \qquad (3.2.1)$$

where $w$ is the sensor side $(1.4\,\mathrm{cm})$ and $d$ the distance between the two sensor centers $(1.8\,\mathrm{mm})$. Here, $A$ represents the area that a particle flux hitting the first sensor with angles $\theta/\phi$ would hit in the second sensor, as illustrated in figure 3.2.3. In addition, when representing the particle fluences as a function of their $\theta$ and $\phi$ angles, care must be taken with the histogram binning. Indeed, bins representing large solid angles will naturally be favored, leading to counterintuitive fluctuations between bins of the 2-dimensional histograms (see figure 3.3.7 in the publication), which is to be avoided for spotting radiation sources. A good way of representing the need for angular corrections is to imagine an isotropic particle source surrounding a detector. In this case, one would expect to obtain a homogeneous 2D histogram when measuring MIP fluences as a function of $\theta$ and $\phi$. This was assessed by simulating a spherical source of MIPs with random directions around an ATLAS-TPX detector, as illustrated in figure 3.3.6 (in the publication). The geometry only included the Timepix chips with sensors and converters, to validate the method independently of PCB/casing design.

### 3.2.2. Neutrons

When investigating the detrimental effects of harsh radiation conditions, neutrons are a major concern because they are responsible for detector damage and electronic disruptions [70]. With ATLAS-TPX, they are detected through their interactions in the dedicated converter layers placed in between the two Timepix detectors, as illustrated in figure 3.3.1 (in the publication):

- A $^6$Li layer for thermal neutron capture, inducing an $\alpha$ and a triton particle ($^6$Li(n,$\alpha$)$^3$H, E$_\alpha$=2.05 MeV, E$_{triton}$=2.73 MeV).
- A polyethylene (PE) layer for fast neutrons, emitting recoiled H and C ions through inelastic scattering. Here, $E_R = \frac{4A}{(1+A)^2} \cos^2(\theta) E_n$ where $\theta$ is the angle between the incoming neutron ($E_n$) and the recoiling nucleus ($E_R$, R=H,C).
- A PE+Al layer for fast neutrons above 4 MeV, the 80 µm thick aluminum layer acting as a kinematic threshold.
- A free (uncovered) area for measuring neutron interactions in the silicon sensor, which represent a background signal for this method.

The technique, then, consists of three steps. First, neutron-induced events are counted in each of the four sensor areas. They are distinguishable from MIPs and photon events because the short range of neutron-induced particles leave large symmetrical pixel clusters, as illustrated in figure 3.2.4. Secondly, the count rate measured below the uncovered area is subtracted from the three other count rates, resulting in net neutron signals. Finally, calibration factors are applied to obtain thermal and fast neutron fluences: each ATLAS-TPX detector was calibrated in several neutron fields, which is described in Ref. [16]. Applying this methodology to measured data, neutron fluences at several positions in ATLAS are presented and discussed in the following publication.

### 3.2.3. Photons

Finally, the study of the photon field is also important because, as for neutrons, it is an abundant component (see figure 3.2.1) that is responsible for detector aging [98]. Moreover, it is a trace of induced radioactivity ($\gamma$ decay of radioisotopes produced by neutron interaction with ATLAS materials and LHC beam pipe), which limits the possibility for human interventions during LHC shutdowns. As seen in chapter 2, Timepix detectors can, to
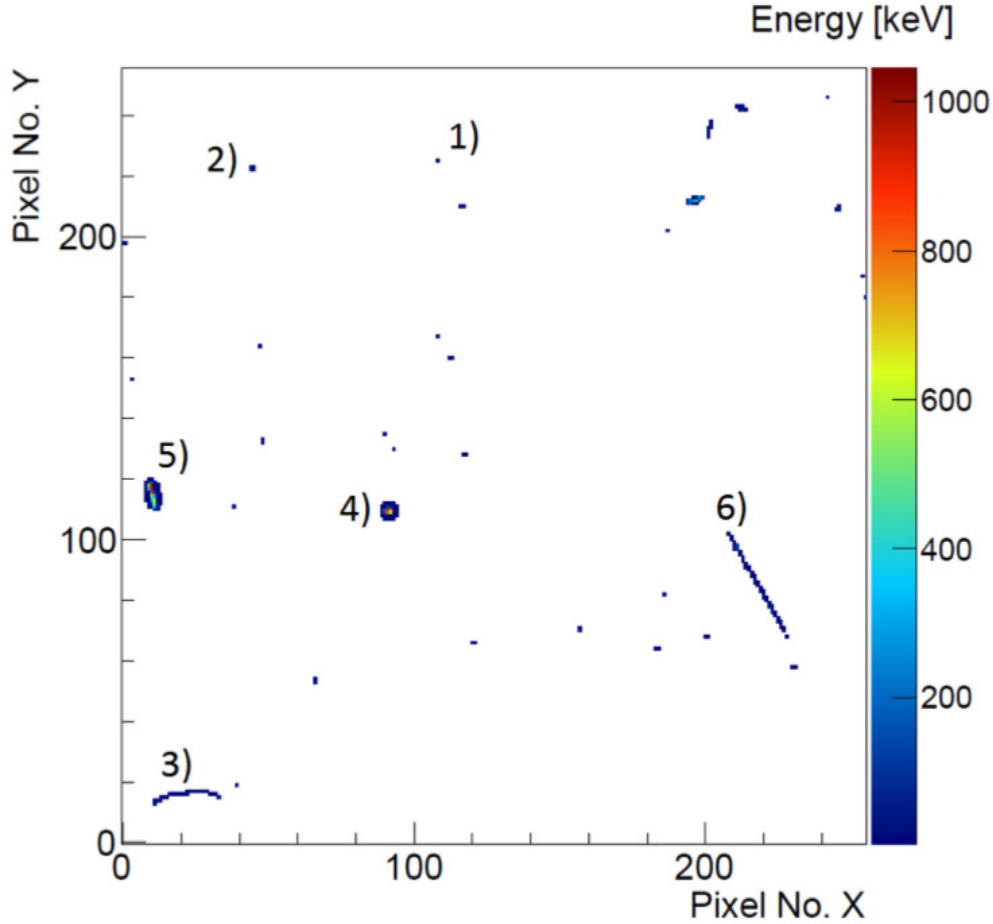
**Fig. 3.2.4.** Example of a frame recorded by ATLAS-TPX, showing the different categories of clusters (see section 2.4): dots (1, 2) and curly tracks (3) originate either from X/$\gamma$ rays or electrons below their MIP regime, straight tracks (6) come from MIPs and HETEs (4,5) are typical neutron-induced events.

some extent, distinguish X and $\gamma$ rays from other particle types, allowing the measurement of deposited dose and other operational quantities. This has been demonstrated in well defined conditions, for example in Ref. [99]. However, in ATLAS, due to the complexity of the radiation field, it is difficult to extract such properties, or even separate photon tracks from electron tracks, especially with the silicon sensors involved. Moreover, the chipboards and casing of ATLAS-TPX detectors stop incident photons below few tens of keV before they interact in the sensors. Possibilities for improving photon detection include high-Z sensors (e.g. CdTe, GaAs) and the next generation Timepix3 chip, which is discussed in chapter 4.

For this reason, the photon field was not investigated in details in the following paper, which only concerns silicon-based Timepix detectors.

## 3.3. Publication: Characterization of the Radiation Field in ATLAS With Timepix Detectors

My contributions to the publication:

- Authorship of the paper
- Development of the analytical methods
- Carrying out of the simulations
- Analysis of the data
- Participation in the energy calibration and installation of ATLAS-TPX detectors in ATLAS

C. Leroy and S. Pospisil established the proposal for the ATLAS-TPX project [12] and supported the formulation of the paper. B. Bergman contributed to the developments of methods and helped formulating the paper.

Note: the authors are listed in alphabetical order.

# Characterization of the Radiation Field in ATLAS With Timepix Detectors

*Benedikt Bergmann[1], Thomas Billoud[1,2,*], Claude Leroy[2] and Stanislav Pospisil[1]*

[1]Institute of Experimental and Applied Physics, Czech Technical University in Prague

[2]Groupe de Physique des Particules, Université de Montréal

[*]Corresponding author

publication

### 3.3.1. Abstract

We present a study of the radiation field at various locations in the ATLAS experiment, using compact detector systems based on pixelated silicon sensors assembled with Timepix readout chips. The hodoscope design of the ATLAS-TPX detectors includes neutron converters in between two sensors, allowing the characterization of both neutron and charged particle fields on a track by track basis. Thermal and fast neutrons are discriminated by segmenting the sensor area with dedicated sensitive materials. Using specific pattern recognition algorithms, clusters from electrons and photons above $\sim 10\,\text{keV}$, MIPs and highly ionizing particles are classified. A coincidence method using the Time-over-Threshold mode of the chip is developed to extract stopping power and directional information of energetic charged particles. Thermal neutron fluences are obtained for each ATLAS-TPX unit, illustrating the effect of detector material and shielding in the experimental cavern. Reconstructed trajectories of energetic charged particles point out radiation coming from the interaction point and other hot spots.

### 3.3.2. Introduction

In modern high energy collider experiments, a precise knowledge of the radiation field and its impact are important for several reasons. Concerning physics analysis, particles originating from interactions in the experiment materials affect detector occupancy and trigger rates. On an operational point of view, induced radioactivity limits access for human intervention in between collision periods. Such harsh environments are also responsible for radiation damage to sensors and their electronics [42], which is a challenge for detector design. The effects of these adverse conditions depend on the composition of the radiation field, and vary according to the location in the experiment.

In practice, the knowledge of the radiation field mainly relies on simulations. In the ATLAS experiment [11], a significant effort is devoted to this purpose [89], which is necessary for detector upgrades and radiation hazard predictions [101]. Even though the comparison between different simulation tools can be used for validating predictions, benchmarking the radiation field composition with actual measurements is necessary. Depending on the purpose of measurements, several types of detectors can be used [102, 103]. For damage studies, simulated particle fluences are typically converted to measurable values such as Total Ionizing

Dose (TID) or 1 MeV neutron equivalent fluences, whereas for induced radioactivity studies, the Sievert is a common unit representing the effect of radiation on the human body. For the ATLAS pixel and strip detector systems, in particular, investigations performed before and after the start of LHC operation have led to a comprehensive knowledge of radiation damage to silicon sensors, for example in terms of leakage current and depletion voltage stability [104, 105, 90, 93]. These various quantities and units are measured by applying different conversion factors or models [106], that are usually obtained experimentally and depend on the radiation type. They consequently come with intrinsic errors and can lead to discrepancies between simulation and measurement.

In the present study, we propose a method to characterize the radiation field in ATLAS without the need to apply specific models, measuring incident particle properties on a track by track basis. We use compact pixelated detectors, based on the Timepix (TPX) readout technology [107], that can be easily positioned at different locations in the experiment. This detector network, so-called ATLAS-TPX [108], was monitoring radiation during the LHC Run 2 (2015-2018), with detectors as close as 3.7 m to the interaction point (IP). It is an upgrade of the ATLAS-MPX network [13], which was based on Medipix (MPX) readout chips and operated successfully during the LHC Run 1 (2008-2012). Since the release of the TPX readout chip in 2006, a solid experience has been gained on particle categorization with TPX detectors, and several particle tracking features have been demonstrated [109]. Using pattern recognition algorithms on the reconstructed pixel clusters, it is possible to determine the stopping power (dE/dX) and incident angle of energetic charged particles crossing the sensor along a straight path. Making use of dedicated converter layers fixed between two Timepix detectors (hodoscope design), the measurement of neutrons is also possible, with the distinction between thermal and fast neutrons.

### 3.3.3. The ATLAS-TPX network

#### 3.3.3.1. *The hodoscope design*

The detector used in the ATLAS-TPX network is described in figure 3.3.1. It is a hodoscope composed of two Si sensor layers facing each other, each equipped with a Timepix chip [16]. The sensor layers have different thicknesses, one being 300 μm thick and the other 500 μm thick, in order to compare the detection rate of non-charged particles. Both sensors

are segmented into a square matrix of $256 \times 256$ pixels at a pixel pitch of $55\,\mu$m. The Timepix chip reads out data in constant time intervals, called frames. Each pixel can be set to one of three modes:

- The Time-of-Arrival (ToA) mode, which registers the time stamp of particle tracks with respect to the end of acquisition (frame);
- the Time-over-Threshold (ToT) mode, which gives the energy deposited by the particle in the sensor material;
- and the hit counting mode, that registers the number of signals received per pixel during a frame.

The frames are followed by the dead-time, during which no further hit can be registered. As a result of the pixelation, an ionizing particle interaction is seen as a cluster of adjacent pixels inside a frame. In section 3.3.4, we describe how cluster analysis is used for determination of stopping power and impact angle. In order to separate tracks, frame times have to be adjusted short enough to avoid significant track overlapping (pile-up).

The two ATLAS-TPX sensors are separated by a $1.4\,$mm gap filled with neutron converters, dividing each sensor surface into four sub-areas, as illustrated in Fig. 3.3.1B. A first area is covered by a $^6$LiF foil, where thermal neutrons (kinetic energy $\sim 25\,$meV) are detected with $\alpha$ and $^3$H particles emitted after neutron capture in $^6$Li. Then, two areas are covered by a $1.2\,$mm thick Polyethylene layer (PE) for fast neutron measurement through the detection of recoil protons in the sensors. On top of one PE area, an additional $80\,\mu$m thick Al foil is inserted, acting as a kinematic threshold at $\sim 4\,$MeV. Finally, a fourth area remains uncovered to measure background events, which include neutron-induced reactions in Si such as $^{28}$Si(n,$\alpha$)$^{25}$Mg or $^{28}$Si(n,p)$^{28}$Al.

### 3.3.3.2. *Positions in the ATLAS cavern*

Sixteen ATLAS-TPX detectors were installed for the LHC operation from 2015 to 2018. Their positions are illustrated in Fig. 3.3.2, and listed in Table 3.3.1. In the table, Z and R are the cylindrical coordinates of the ATLAS cylinder, whose center is the IP. $\theta$ is the polar angle between the IP and the sensor surface ($\theta = 0°$ means perpendicular). Detector surfaces are perpendicular to Z, except for TPX08 and TPX09 which are placed horizontally and TPX15 and TPX16 which are outside the ATLAS detector. TPX15 is on a wall of the
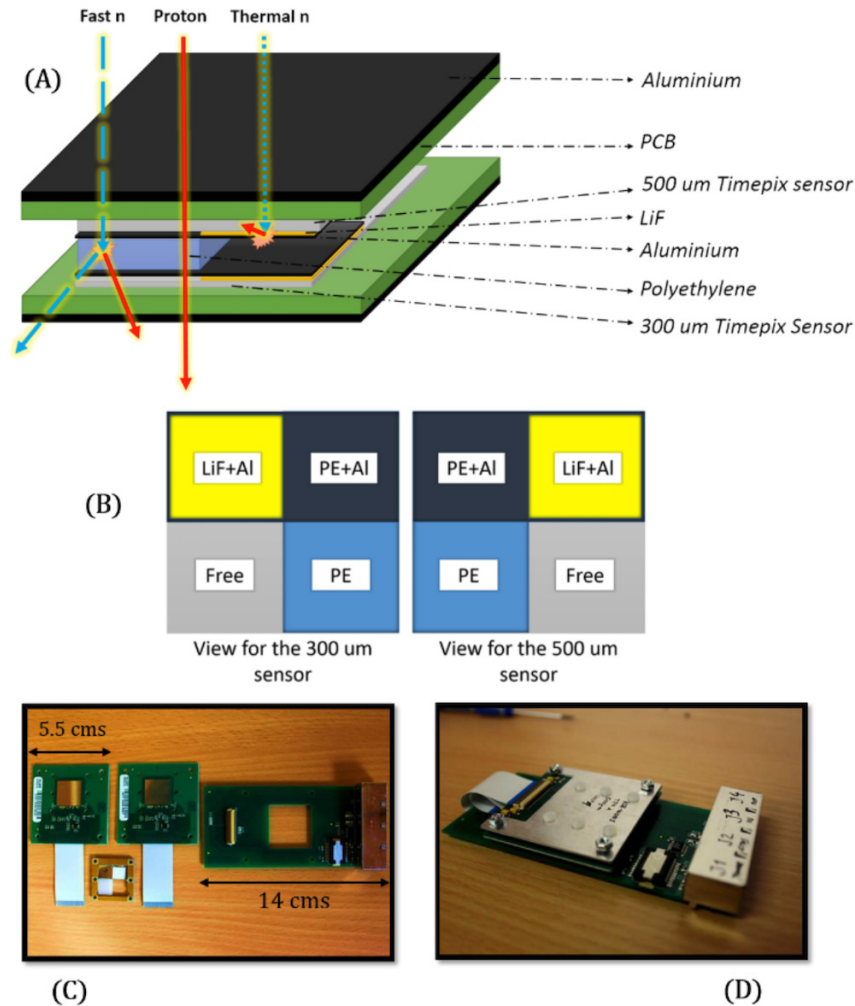
**Fig. 3.3.1.** The ATLAS-TPX detector [**16**]. (A) illustrates the detector design and the principle of discrimination between charged particle and neutron events. (B) shows the segmentation of the sensor surface into the four neutron converter areas, including the free (uncovered) area for background subtraction (see text for more details). (C) gives the dimensions of the detector components and (D) shows the assembled detector unit, which is then placed in a aluminum casing.

experimental cavern and TPX16 (which is not discussed here) is in the USA15 room, where most of ATLAS electronic equipment is stored. Two detectors (TPX02 and TPX12) were dedicated to luminosity monitoring using the hit counting mode, which was presented in a separate study [**110**]. Two other detectors (TPX03 and TPX13) were used in ToA mode. All other detectors were operated in ToT mode, which is the focus of the present study.
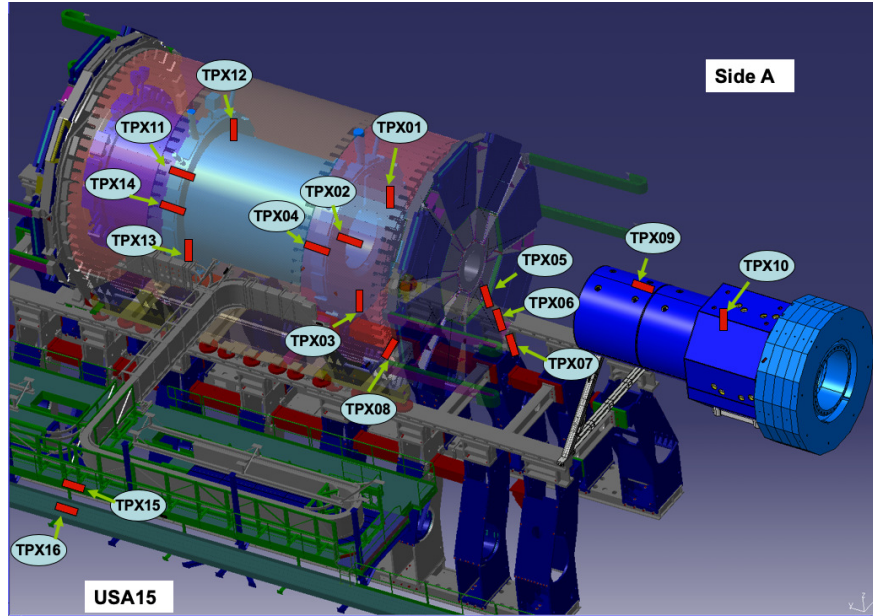
**Fig. 3.3.2.** Position of ATLAS-TPX detectors in ATLAS.

### 3.3.4. Analysis Methods

In section 3.3.5.1, we apply the neutron detection described in [**16**] to data taken in AT-LAS. For the characterization of the charged particle field presented in section 3.3.5.2, a new technique is developed. Both methods share features from the original pattern recognition algorithms described in [**111, 112, 109, 113**], which are summarized first.

#### 3.3.4.1. *Pattern recognition and cluster properties*

The analysis starts with the separation of clusters into six categories based on their geometrical shapes, which are illustrated on top of Fig. 3.3.3. Dots and small blobs are typically the trace of either low energy electrons (including those ejected by photons) or minimum ionizing particles (MIPs) hitting the sensor perpendicularly. Higher energy electrons, or MIPs emitting $\delta$-rays, give curly tracks. When hitting the sensor with a high incident angle without $\delta$-rays, MIPs also generate straight tracks. Finally, the larger shape of heavy blobs and heavy tracks arise in the case of high energy transfer particles, where the charge sharing effect [**114**] induces a pixel core with high energy deposit surrounded by a low signal halo. These two cluster types will be referred to as high energy transfer events (HETEs). Each

47

**Tab. 3.3.1.** Position and operational mode of ATLAS-TPX detectors in the ATLAS cavern. Z is the distance along the beam axis (from the interaction point), R is the radial distance.

| ID | Z (m) | R (m) | θ (°) | Mode |
|---|---|---|---|---|
| TPX01 | 3.54 | 1.11 | 17 | ToT |
| TPX02 | 3.54 | 1.11 | 17 | hit counting |
| TPX03 | 3.54 | 1.13 | 18 | ToA |
| TPX04 | 2.83 | 3.7 | 53 | ToT |
| TPX05 | 7.83 | 1.41 | 10 | ToT |
| TPX06 | 7.83 | 2.57 | 18 | ToT |
| TPX07 | 7.83 | 3.67 | 25 | ToT |
| TPX08 | 7.22 | 6.14 | 90 | ToT |
| TPX09 | 15.39 | 1.56 | 84 | ToT |
| TPX10 | 18.85 | 0.49 | 1 | not functional |
| TPX11 | -3.54 | 1.11 | 17 | ToT |
| TPX12 | -3.54 | 1.14 | 18 | hit counting |
| TPX13 | -3.54 | 1.11 | 17 | ToA |
| TPX14 | -2.83 | 3.7 | 53 | ToT |
| TPX15 | 4.86 | 16.69 | 16 | ToT |

cluster is characterized by a volume, which is the total energy summed over its pixels, and a centroid, which is its energy-weighted geometrical center.

Whenever directional information is needed, it is necessary to determine the incident polar ($\theta$) and azimuthal ($\phi$) angles corresponding to each cluster. For this, we first distinguish clusters that could correspond to particles hitting the sensor surface perpendicularly; they include dots, small blobs and heavy blobs. For dots and small blobs, the ambiguity between low energy electrons and perpendicular MIPs vanishes once the coincidence/anti-coincidence is determined (see section 3.3.4.3). Depending on the sensor thickness, this 'perpendicular' cluster category also includes particles with a small incident angle; for each shape, a maximum angle is attributed. For non perpendicular particles, the incident angle determination is easier, since the corresponding clusters are elongated. In this case, a linearity threshold is
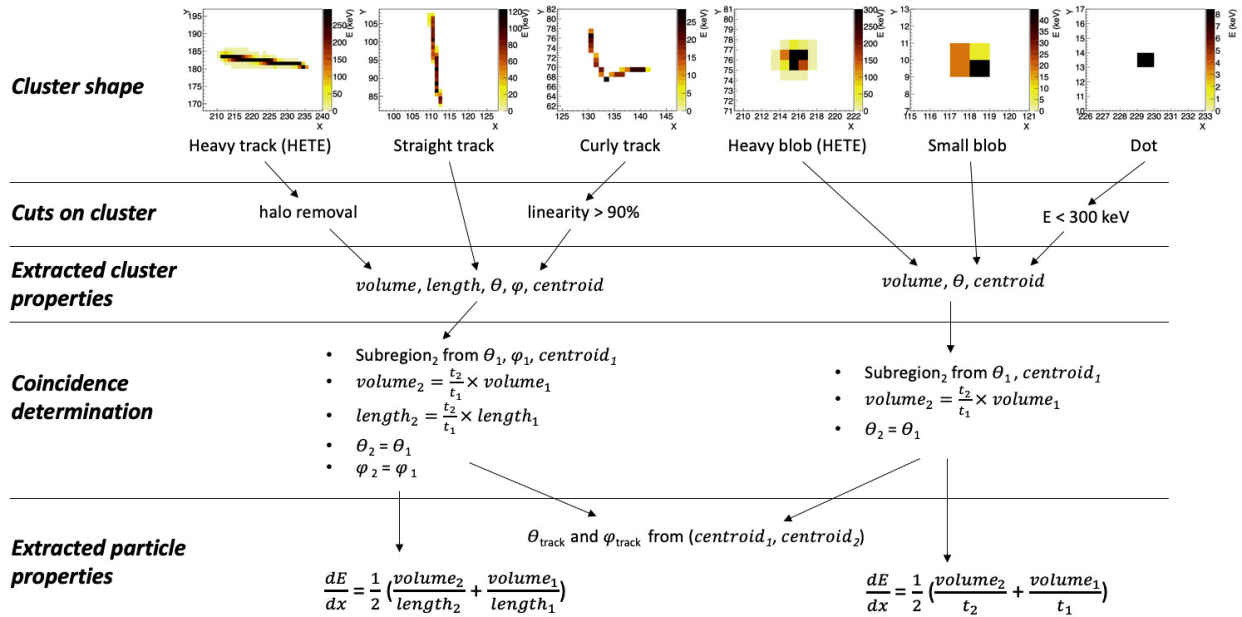
**Fig. 3.3.3.** Description of cluster processing in order to reconstruct charged particles incident angle and stopping power. $t_1$ and $t_2$ are the thickness of the two Si sensor layers, 300 μm and 500 μm respectively (the subscripts of other cluster properties refer to the corresponding layer). See text for more details.

set to reject curly tracks due to low energy electrons or δ-rays. The majority of the remaining clusters are straight tracks, whose angles are simply calculated from their length and the known sensor thickness. In the case of heavy tracks, the surrounding halo is removed by setting a 50 keV threshold before calculating the angles [115].

It should be noted that clusters touching the sensor borders cannot be correctly described, and are rejected in the analysis. In addition, noisy pixels are excluded by rejecting single pixel clusters with energy above 300 keV [113]: in this range of energy deposits, charge sharing starts to appear, making a clear distinction between noise and actual particle interactions.

### 3.3.4.2. *Neutron detection*

As described in [16], products of thermal and fast neutron reactions result in the detection of HETEs. The cluster location and geometrical category are thus enough to provide neutron fluences. In each neutron converter area, HETE counts are subtracted by the amount
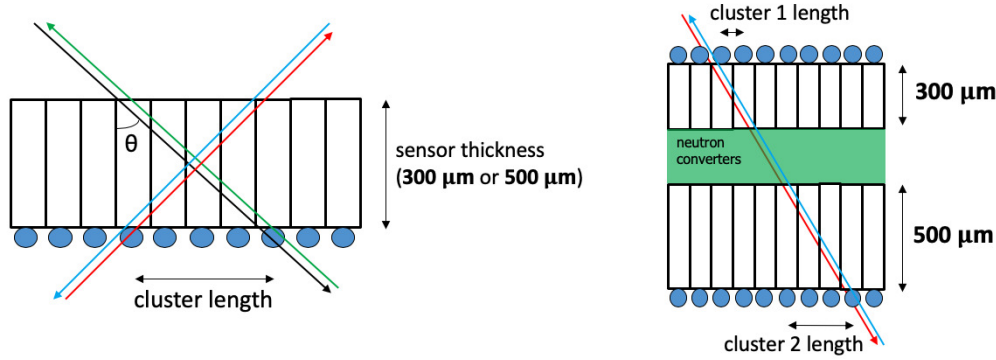
**Fig. 3.3.4.** Possibilities for wrong direction identification of incident angle according to the number of sensor layers (diagrams not in scale). With one layer (left), the same cluster can represent 4 particle directions. With two layers (right), the same combination of 2 clusters can represent 2 particle directions only.

measured below the uncovered region, resulting in the net converter effect. To obtain actual fluences, calibrations were done with an (isotropic) thermal neutron field and with fast neutron sources for several incident angles and energies.

### 3.3.4.3. *Charged particle detection*

The method developed for charged particle field characterization is based on the combined use of ToT information and coincidence determination. While coincidence determination using the ToT mode is more complicated than using the ToA mode, this allows the simultaneous measurement of dE/dX and incident direction.

Even though the particle direction and its dE/dX can be determined with only one Timepix layer, searching for a coincident cluster in the second layer has several advantages. Firstly, it allows one to better discriminate between MIPs and low energy electrons, since both particle types often lead to short straight tracks. Secondly, it improves the incident angle determination in two ways: reducing wrong direction attribution, as illustrated in Fig. 3.3.4, and improving the reconstructed angle precision (especially for perpendicular particle paths) since the trajectory can be extrapolated from the location of the two coincident clusters. Finally, it reduces the error on the dE/dX measurement, since two values are obtained for one particle track. The method is composed of several steps, described in the following subsections.
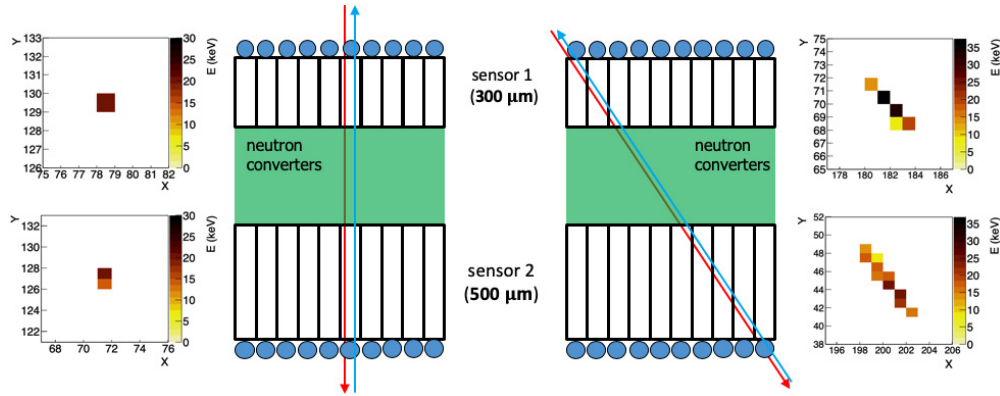
**Fig. 3.3.5.** Illustration of detected coincident events for MIPs crossing the hodoscope at different angles.

**Coincidence determination:** The first step consists of distinguishing MIPs hitting both sensors of the hodoscope (coincidence) from MIPs hitting one sensor only (anti-coincidence). For each cluster of the first layer (cluster 1), the second layer is scanned searching for a coincident cluster that has corresponding properties. According to the incident angle of cluster 1, only a subregion of the second layer is searched for, calculated from possible impact points. Then, a geometrical selection is done among clusters of the subregion according to the possible cluster length: for a given incident angle, a charged particle leaves a longer track in the $500\,\mu\mathrm{m}$ layer than in the $300\,\mu\mathrm{m}$ layer. Similarly, a selection on the deposited energy and $\theta/\phi$ angles of the second layer is applied. Examples of coincident clusters are illustrated in Fig. 3.3.5.

**dE/dx and trajectory reconstruction:** Once coincidence/anti-coincidence has been determined, the next step consists of calculating the charged particle properties of interest. In the case of anti-coincident clusters, only straight tracks and curly tracks with linearity $> 90\,\%$, and containing at least 5 pixels, are kept. This is done in order to reject HETEs from neutron reactions and small clusters from X and $\gamma$ ray interactions. The stopping power is obtained by dividing the cluster volume by the distance traveled by the particle in the sensor, which is calculated from the cluster length and sensor thickness. For coincident tracks, the stopping power is the average of the two coincident clusters dE/dX, and the $\theta/\phi$ angles are computed from the three dimensional vector formed by the centroid of each cluster (the complete decision tree is summarized in Fig. 3.3.3).

**Correction factors for angle maps:** In section 3.3.5.2, MIPs directional information is illustrated with angle maps obtained from coincident events. These maps are presented in polar coordinates, which gives an instinctive representation of the results. The radial axis represents the particle polar angle ($\theta$) with 10° wide bins, 0°/90° meaning perpendicular/parallel to the sensor surface, respectively. The azimuthal axis ($\phi$) is plotted with a 20° binning and depends on the orientation of the detector with respect to the interaction point. In order to get a meaningful information, two corrections must be applied to these histograms. Firstly, each track count is weighted by the effective area ($A_{eff}$) corresponding to its direction:

$$A_{eff} = \cos\theta \; (w - d \; \tan\theta \; |\cos\phi|)(w - d \; \tan\theta \; |\sin\phi|) \tag{3.3.1}$$

where $w$ is the sensor side (1.4 cm) and $d$ the distance between the two sensor centers. The terms in brackets represent the area that a particle flux hitting the first sensor with angles $\theta/\phi$ would hit in the second sensor. Secondly, each bin is divided by its covered solid angle to obtain a homogenized histogram.

**Validation with simulation:** The complete method (track reconstruction + correction factors for angle maps) was assessed by simulating the detection of MIPs with an ATLAS-TPX detector[6], using the *Geant4* [**116**] based software *Allpix2* [**4**]. A simple example illustrating the effect of correction factors is to imagine an isotropic radiation source surrounding a detector, as shown in Fig. 3.3.6. If MIPs have no preferred directions when hitting the sensors, e.g. if they originate from a sphere surrounding the detector, one would not expect fluctuations between the measured incident angles. As seen on Fig. 3.3.7a, without applying correction factors, the angle map is not homogeneous. In the center of the map, the decreased track count is due to the small solid angle covered by MIPs arriving perpendicularly to the detector surface. In the map periphery, the track count decreases because 1) the effective area and 2) the detection efficiency for MIPs with grazing angles are reduced. Applying the correction factors described in the previous subsection, we obtain an homogeneous map (Fig. 3.3.7b), except for the outer periphery that is still affected by the reduced detection

---

[6]For the simulated detector geometry, only TPX ASICs, sensors and neutron converters are taken into account. The detector casing and PCBs are omitted to avoid their impact on MIP trajectories, in order to validate the method independently of hardware design.

**(a)**                                                    **(b)**
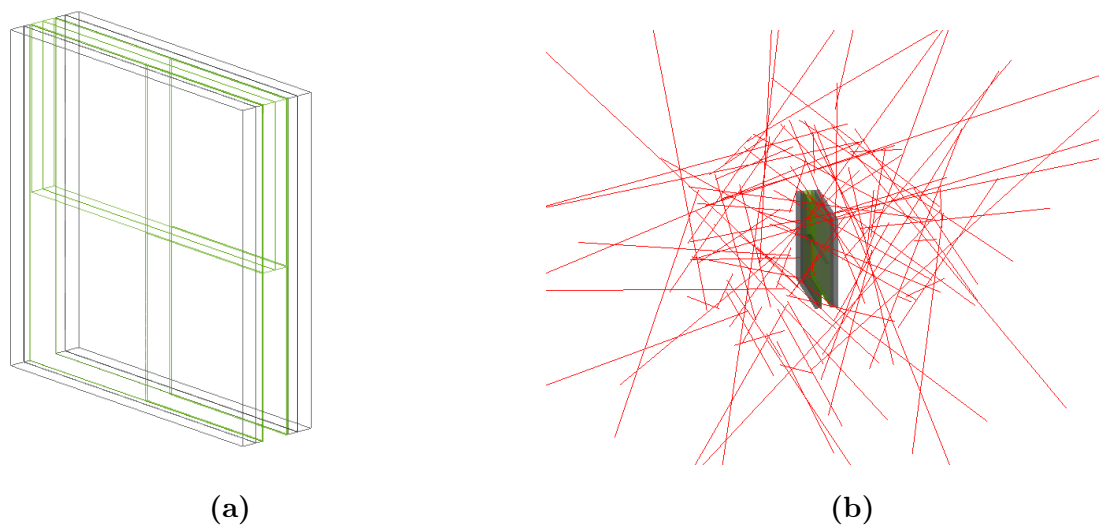
**Fig. 3.3.6.** Simulation of an ATLAS-TPX detector irradiated with an isotropic source of 500 MeV pions. (a) The geometry includes the two Timepix chips with their sensors and the neutron converters. (b) The particles are shot with random directions, from a sphere surrounding the detector.

efficiency of nearly parallel tracks. For this reason, the angle maps shown in section 3.3.5.2 are limited to $\theta = 70°$.

**Limitations of the method:** When frames have high cluster occupancy, using the ToT mode for coincidence determination occasionally leads to cases where more than two coincident clusters are found for one particle crossing the sensors, resulting in wrong coincidence identification. This is due to the tolerance used when comparing cluster angles, necessary to take into account small angle scattering (in the sensor and converter layers) and the limited track resolution caused by the 55 µm pixelation (which particularly affects perpendicular trajectories). It was found that this effect mainly concerned small blobs, and never exceeded a few percent of the total reconstructed tracks in the results presented here.

Another concern, for the measurement of MIPs fluences, is the case of overlapping clusters. This occurs most frequently when MIPs eject $\delta$-rays or when two MIPs cross each other inside the sensors, as illustrated in Fig. 3.3.8a and 3.3.8b respectively. Due the complexity of the radiation field, estimating precisely this effect is complicated and will be done in a
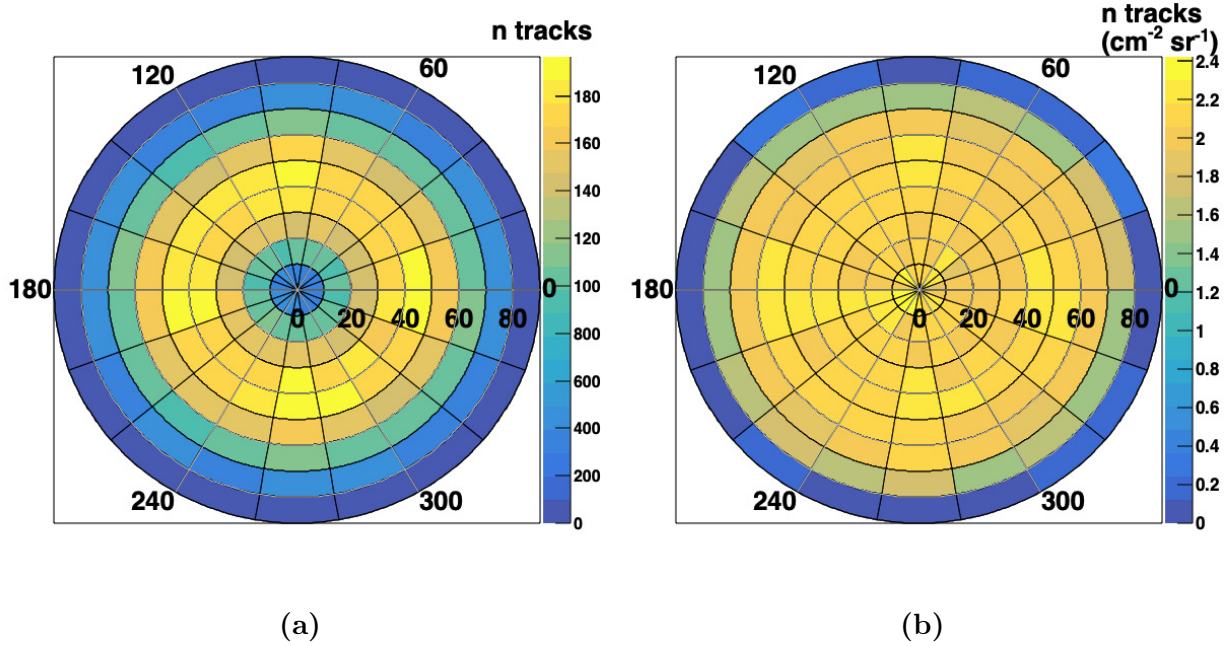
**Fig. 3.3.7.** Reconstructed MIP directions from the simulation described in Fig. 3.3.6. a) Raw track count and b) track count corrected for effective area and solid angle. The radial axis ($\theta$) represents the incident angle with respect to the sensor surface, as illustrated in Fig. 3.3.4 ($\theta = 0°$ means the particle is perpendicular to the surface).
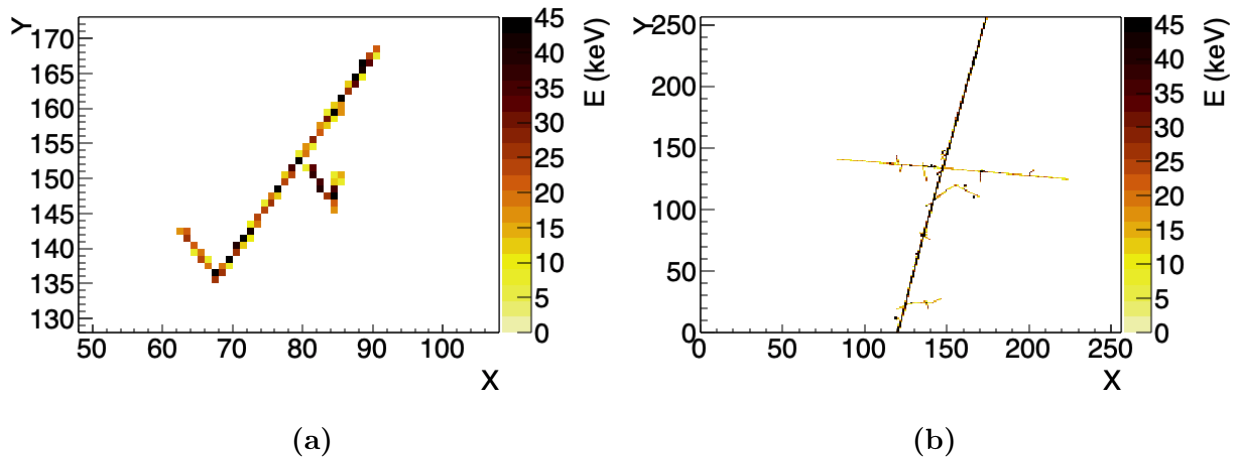


**Fig. 3.3.8.** Examples of overlapping clusters. a) One MIP emitting $\delta$-rays and b) two MIPs crossing each other (also with $\delta$-rays).
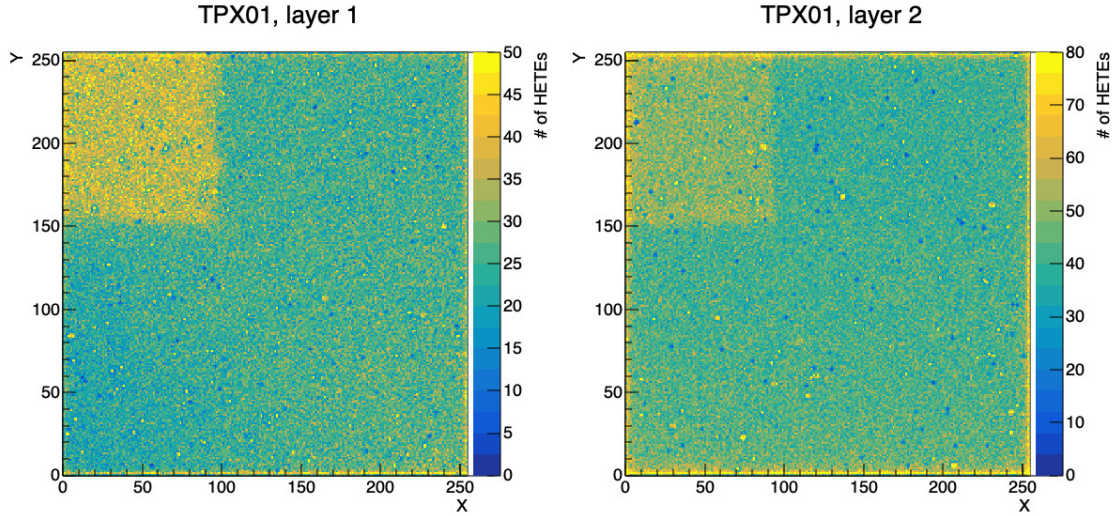
**Fig. 3.3.9.** Number of HETEs registered per pixel with TPX01 during several LHC runs in May 2016 (accumulated luminosity: 530 pb$^{-1}$). HETE locations are determined from the cluster centroid. The neutron converters placed in-between the two sensor layers are indicated, correspondingly to Fig. 3.3.1. The thermal neutron signal below the LiF+Al converter does not fully cover the delimited area due to the gaps between the different converters. For each pixel, the number of recorded events is incremented when the centroid of a HETE cluster is detected.

separate study. However, such events are rejected by the linearity criteria, and do not induce wrong dE/dX or incident angle measurements.

### 3.3.5. Results and Discussion

3.3.5.1. *Neutrons*

The detection of neutron-like events is illustrated in Fig. 3.3.9, with the number of HETEs registered by each pixel of TPX01 during several LHC runs. The thermal neutron signal below the $^6$LiF area can clearly be identified on the top left corner of each layer, allowing the fluence calculation as described in section 3.3.4.2. However, no clean distinction could be made between the PE areas and the uncovered area. This can be explained by the hardness of the fast neutron spectrum, involving a significantly higher probability for reactions
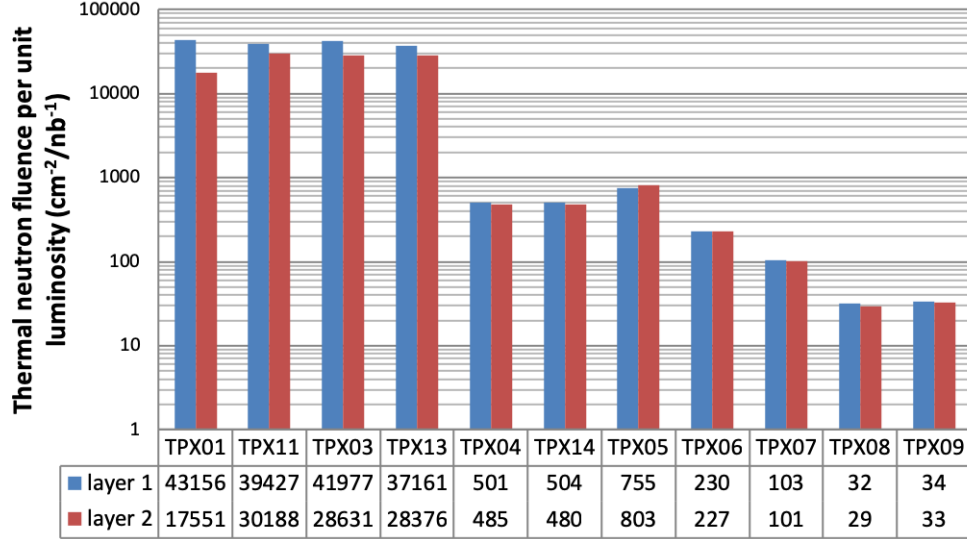
**Fig. 3.3.10.** Thermal neutron fluences per unit luminosity for the different ATLAS-TPX devices as measured during LHC Fill 4965 on May 31, 2016 (accumulated luminosity: $160\,\mathrm{pb^{-1}}$) [**117**].

in Si compared to the expected signal (recoiled protons). Although calibrations were successful [**16**], the composition of the radiation field inside ATLAS is hence too complex to separate high energy transfer particles from fast neutron events.

The thermal neutron field in ATLAS is strongly dependent on location, due to the various detector and shielding materials surrounding the interaction point and beam pipe. This is illustrated in Fig. 3.3.10 [**117**] with thermal neutron fluences at the ATLAS-TPX detector locations. The four closest detectors to IP, about 1 m from the beam axis (TPX01, TPX03, TPX11, TPX13), show the highest fluences. They are placed on a wall between the electromagnetic calorimeter barrel (EMB) and its end-cap, close to the forward calorimeter (FCAL) which is the dominant source of neutrons [**42**]. On the first forward muon system facing IP (the so-called small wheel [**11**]), TPX05 measures two orders of magnitude lower fluences, pointing out the effect of the polyethylene-boron shieldings designed to moderate and absorb neutrons from the beam pipe [**118**]. Further away from IP and FCAL, detectors on the outer part of EMB (TPX04, TPX14) and on the small wheel (TPX06, TPX07) show comparatively lower fluences. The lowest values are obtained with TPX08 and TPX09, which are outside the dense inner region of ATLAS.

### 3.3.5.2. *Charged particles*

**Stopping power measurements:** As for neutrons, the charged particle field in ATLAS strongly depends on the position of detectors which face varying fluences, energies and directions. Primaries from the interaction point and their scattering products in the experiment materials create a complex hadronic and leptonic field, mainly composed of protons, pions, electrons and muons. Even though their type cannot be distinguished with the presented methods, energetic charged particles penetrate through the sensor layers, allowing stopping power and flux measurements with clear distinction from lower energy electrons induced by photons. Following the methods described in section 3.3.4.3, the dE/dx spectra for all detectors are illustrated in Fig. 3.3.11 with logarithmic scale and in Fig. 3.3.12 with linear scale. Histograms are normalized per unit luminosity, thus obtaining charged particle fluxes for each energy bin. The logarithmic histogram reflects the steep variation of radiation levels in ATLAS, particularly around the beam pipe and in the dense core containing the inner tracker and calorimeters [42]. For example, fluxes measured by TPX01 ($Z = 3.5\,\text{m}$, $R = 1.1\,\text{m}$) are three orders of magnitude higher than for TPX04 ($Z = 2.8\,\text{m}$, $R = 3.7\,\text{m}$) and TPX05 ($Z = 7.8\,\text{m}$, $R = 1.4\,\text{m}$). On the linear histograms, we observe spectra that are similar to the typical Landau distribution of MIPs, with peaks around $1.2\,\text{MeV}\,\text{cm}^2/\text{g}$. The deviation from true Landau distribution is due to the mixed composition of the charged particle field and the cut on MIP clusters overlapping with $\delta$-rays.

**Direction measurements:** In addition to dE/dX measurements, the methods described in section 3.3.4 allow one to measure the direction of energetic charged particles. This is illustrated in Fig. 3.3.13 for all detectors. Here, the radial axis represents the polar angle ($\theta$) of incident particles, the disk center representing particles going through the sensor perpendicularly. The azimuthal axis ($\phi$) represents the rotation of the sensor surface around the beam axis (Z), except for TPX08, TPX09 and TPX15 which are not perpendicular to Z. Each $\theta/\phi$ bin is normalized to effective area, solid angle and integrated luminosity. The closest detectors to the IP, TPX01 and TPX11, and the three detectors placed on the muon system wall (TPX05, TPX06, TPX07), show maximum fluxes for polar angles corresponding to the relative IP position. TPX04 and TPX14 show, in addition to the IP direction, a significant amount of measured tracks close to perpendicular, indicating hot spots facing their surface (either on their front or back, as explained in section 3.3.4). Further away and
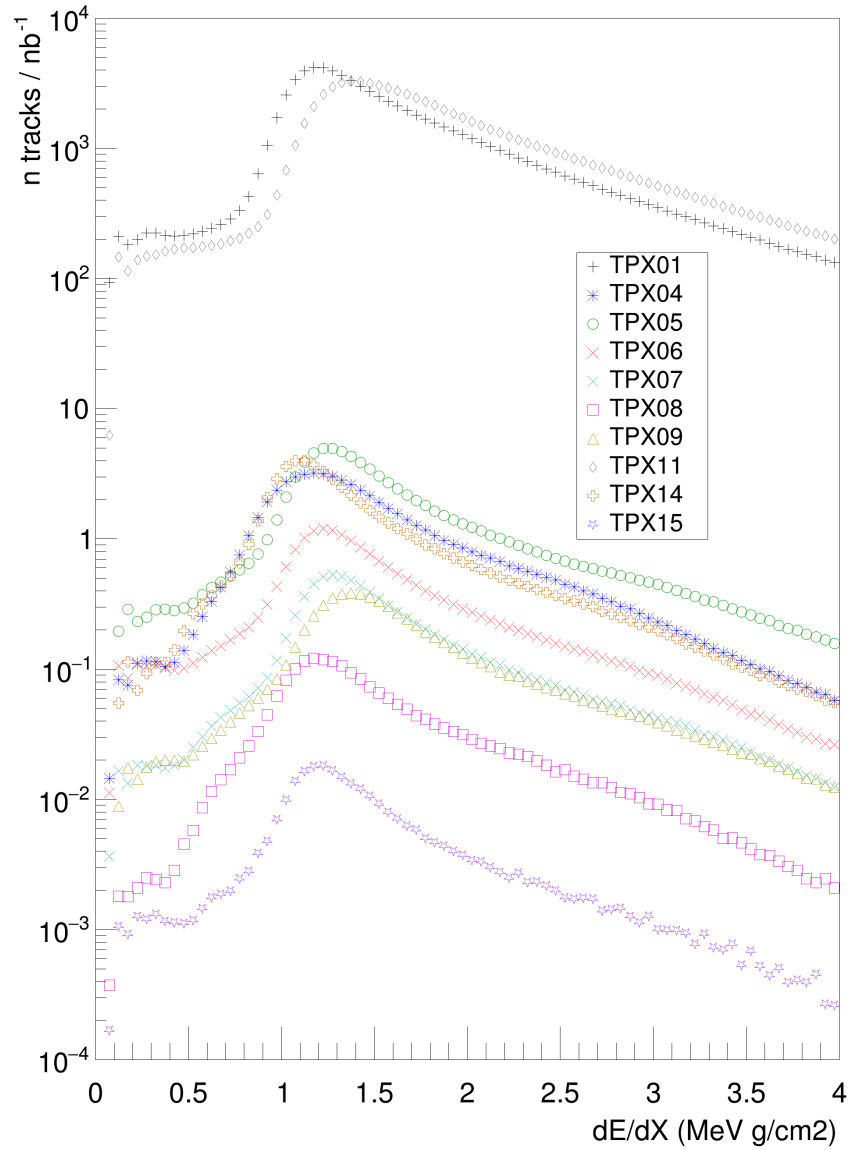
**Fig. 3.3.11.** Stopping power (dE/dX) of tracks measured by the ATLAS-TPX detectors with logarithmic scale (see detector positions in Table 3.3.1). The number of tracks per dE/dX bin is scaled per integrated luminosity. Data were measured during LHC Fill 4965 on May 31, 2016 (accumulated luminosity: $160 \, \text{pb}^{-1}$).
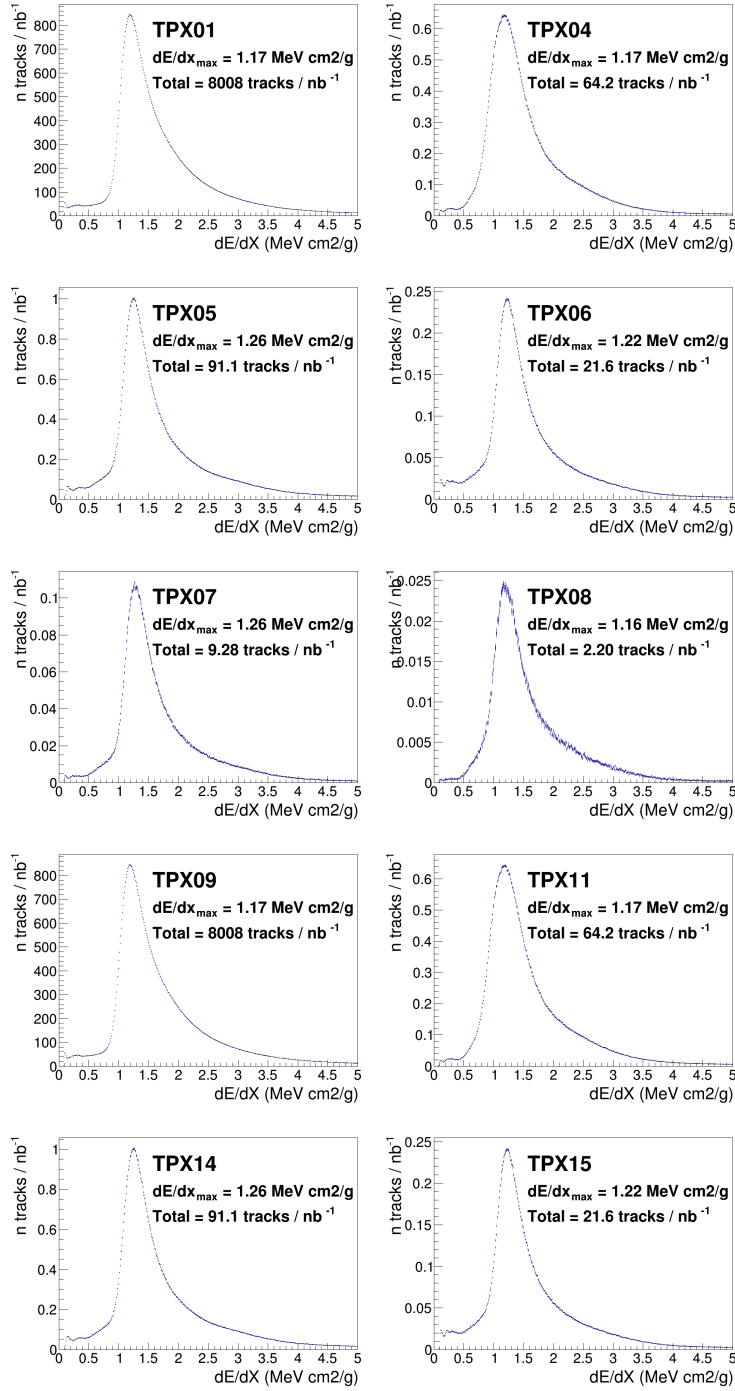
**Fig. 3.3.12.** Stopping power (dE/dX) of tracks measured by the ATLAS-TPX detectors with linear scale (see detector positions in Table 3.3.1). The number of tracks per dE/dX bin is scaled per integrated luminosity. Data were measured during LHC Fill 4965 on May 31, 2016 (accumulated luminosity: $160\,\text{pb}^{-1}$).

59

horizontally placed, TPX08 and TPX09 only measure surrounding radiation sources, since the IP is not included in their solid angle acceptance. Finally, various directions are observed with TPX15, which measures radiation escaping the ATLAS detector.

### 3.3.6. Conclusion

In this study, the capabilities of ATLAS-TPX detectors have been used for analyzing the composition as well as spectral and directional characteristics of radiation fields in the ATLAS experiment. Results can be used to benchmark simulations or evaluate radiation background properties at sensitive sub-detectors locations. Due to their compactness, these detectors can be easily installed in arduous locations where a better understanding of the radiation fields is required. In the course of the LHC Run 2, first investigations revealed no significant signal deterioration in terms of charge collection efficiency and cluster morphology, even for detectors as close as 3.7 m to the interaction point. In this regard, further studies will be performed, including in-house tests after the removal of detectors from the ATLAS cavern.

Even though this technology offers unprecedented capabilities for charged particles and neutron detection, it is still difficult to characterize the photon field precisely in such a complex environment. Progress in X-ray and $\gamma$-ray dosimetry has been achieved recently with Timepix chips [99], and the methodology for similar characterization of radiation fields around HEP experiments is now under development [117]. With the availability of the new Timepix3 chip [119], the dual ToA and ToT mode will allow reconstructing the three-dimensional path of incident electrons in the sensor volumes [120], improving the detection of Compton induced events. These chips were already assessed in the ATLAS cavern and around the LHC beam pipe in 2018, and will be used in the succeeding network, ATLAS-TPX3. First tests were successful and their ability to synchronize with LHC bunch crossings was proven, through their 1.6 ns time granularity [121].

In terms of fast neutron measurements, it is evident from the results that the concept of recoiled protons (whose functionality has been verified in Los Alamos Neutron Science Center [122], in the range of energies from 1 MeV to 20 MeV) does not distinguish recoiled protons from signal produced by highly energetic neutrons and hadrons in the sensor. In the present conditions, the signal is integrated during a time which is significantly longer
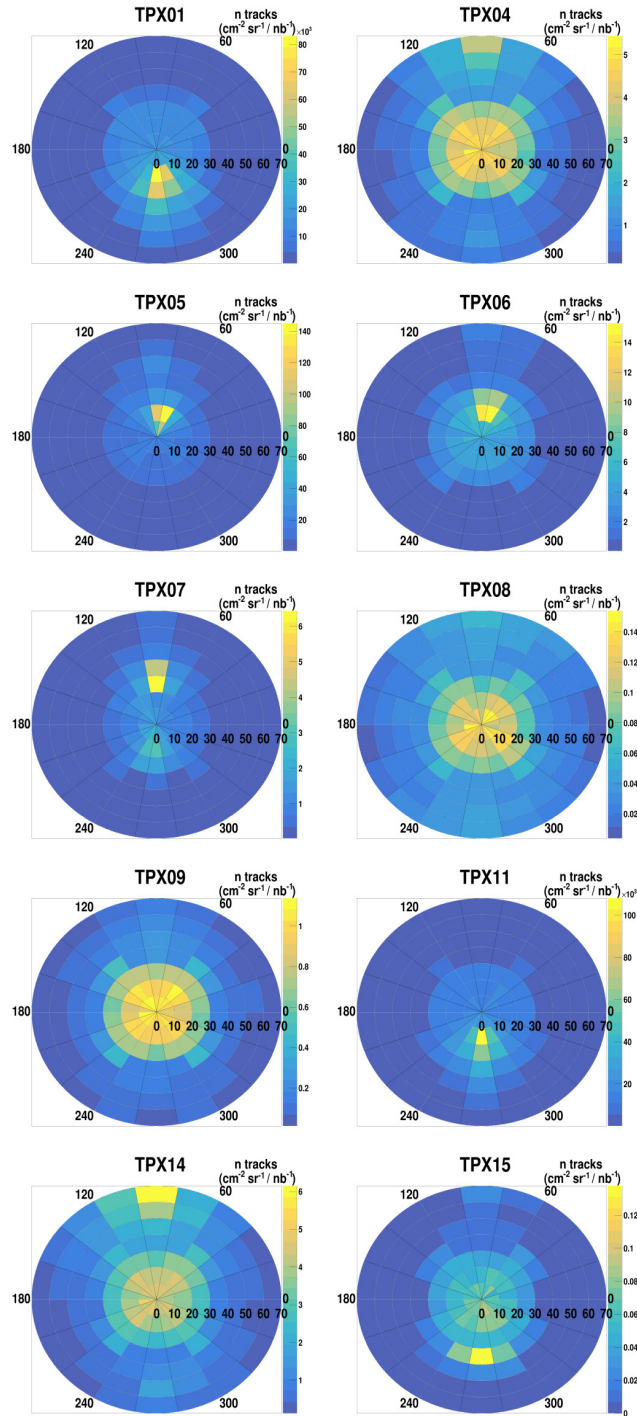
**Fig. 3.3.13.** MIP directions measured by the ATLAS-TPX detectors (see detector positions in Table 3.3.1). The radial axis ($\theta$) represents the incident angle with respect to the sensor surface ($\theta = 0°$ means the particle is perpendicular to the surface). Data were measured during LHC Fill 4965 on May 31, 2016 (accumulated luminosity: $160\,\mathrm{pb^{-1}}$).

61

than the time between individual proton-proton collisions in ATLAS. However, the results of fast neutron field measurements presented in this work contributed to the design of the ATLAS-TPX3 network, which allows to distinguish primary particles originating from the LHC beam collisions from the secondary particles (including neutrons) produced in the ATLAS environment by means of ToA.

publication

## 3.4. Summary and Beyond

This paper continues the investigation started in 2008 with the ATLAS-MPX detector network to measure and characterize the mixed radiation fields in ATLAS, but using its successor, the ATLAS-TPX detector network. In addition to particle categorization and thermal neutron fluence determination previously exposed in [13], the possibility to measure charged particle directions and dE/dx was demonstrated. Thereafter, results can be compared with simulations, which is foreseen for a near future. Combining the dE/dx and incident angle information on a track by track basis, one can get an insight on the locations where MIPs originate, as can be predicted with simulations (see figure 3.4.1). When performing such investigations, one must be keep in mind possible systematic errors that can arise from the presented methods. As explained in the paper, the technique for simultaneous angle and dE/dx determination of MIPs requires complex algorithms for coincidence identification, which is deteriorated in case of high frame occupancy. In this case, discrepancies between measurements and simulations could be observed. This issue will vanish with Timepix3 chips, since TOT and TOA modes can be used simultaneously, making coincidence identification much easier. Hodoscopes with TPX3 chips were operated in ATLAS in 2018, and the methods developed here could already be adapted and tested with the measured data. On another side, the paper explains that the measurement of fast neutrons proved to be problematic. This issue will be investigated further, using simulations results such as neutron spectra and their birth positions in the ATLAS cavern, as shown in the bottom right of figure 3.4.1.

Several other investigations are still to be done with ATLAS-TPX data. First, the energy deposited in Si sensors can be extracted for each cluster category, allowing estimations of the neutron and gamma doses. Measuring such quantities directly after LHC beams are dumped allows the identification of radioactivity sources limiting human interventions. Moreover, the detection of radioisotopes with long half-life can help in the decommissioning of activated parts of ATLAS. Radioactivity also contributes to the signal in ATLAS-TPX detectors during collisions periods and must be assessed both in the short term and in the long-term. This is particularly important for luminosity monitoring, which is currently being investigated using ATLAS-TPX detectors operated either in counting or TOT mode. On another hand, the fine segmentation of TPX chips can help characterizing radiation damages to Si sensors with
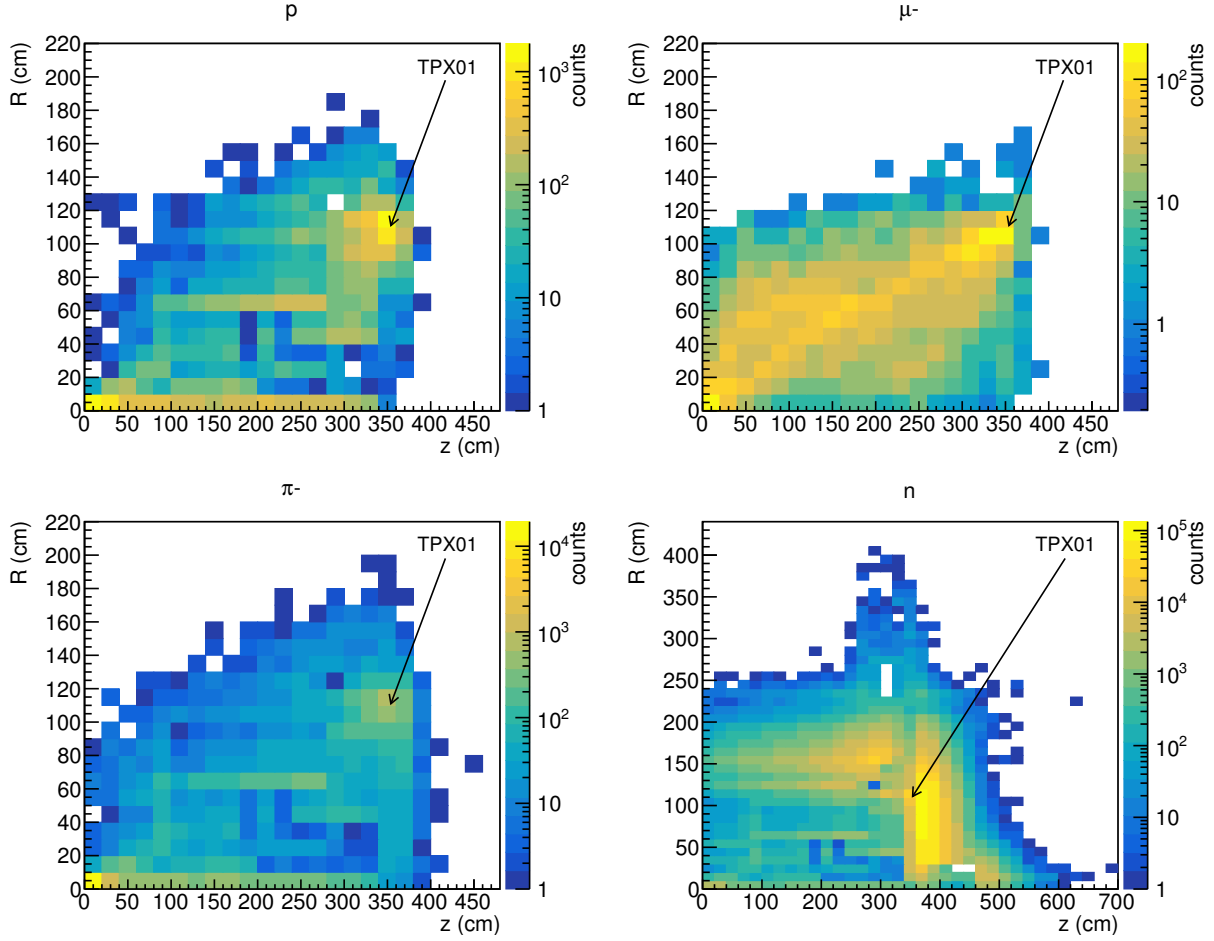
**Fig. 3.4.1.** Birth position of protons (p), muons (μ-), pions (π-) and neutrons (n) hitting the location of TPX01 in ATLAS (see table 3.3.1 for the detector location in ATLAS), as obtained from simulations [**97**]. The coordinate system origin is the interaction point, on the bottom left corner. The Z-axis is the distance along the beam pipe, and the R coordinate is the cylindrical radial distance. The ATLAS geometry, and consequently, the radiation field, are considered symmetrical around the Z-axis. Note the different scale and binning between charged particles and neutrons.

a good spatial resolution, comparing the signal amplitude between pixels over time. This can be done, for example, by analyzing the stability of cluster shapes and energies, providing spatially resolved charge collection efficiency estimations as a function of deposited dose. Finally, on a bigger picture, the demonstrated capabilities of the ATLAS-TPX detectors (and future upgrades) could be exploited in other experiments. In particular, the severe

conditions expected in the upcoming HL-LHC draws a special attention on the radiation hardness testing of the future upgrades of the four main detectors (ATLAS, CMS, LHCb and ALICE) [123].

# Chapter 4

## High-Z sensors for ATLAS-TPX upgrades

### 4.1. Context

Until today silicon still is the most common semiconductor material used for pixelated radiation sensors. The available material quality and low price tag of this material benefits from decades of manufacturing experience, resulting in the availability of rather cheap and high quality crystals with precise doping profiles. Advances in Si technologies also led to the recent availability of monolithic detectors, where readout chip and sensor are tailored in the same block of semiconductor, and to *3D sensors* where electrodes are hollowed out the silicon volume to reduce charge carrier drift time. Despite these advantages, the low atomic number of Si makes it a relatively weak tool for applications involving the detection of X and $\gamma$-rays, especially medical imaging, hadron therapy and electromagnetic radiation monitoring. Since especially the interaction cross-section of the photoelectric effect, but also that of Compton scattering and pair creation are functions of the atomic number, high-Z materials have been considered and tested in parallel of Si sensor development. High-Z compound semiconductors have, in addition, higher stopping powers for charged particles and wider band-gaps, which is an advantage for a wide range of applications [124]. However, the growth of such crystals has proven to be difficult, and detectors equipped with these sensors are suffering from incomplete charge collection, inhomogeneities and time-dependent fluctuations affecting their response [125, 126, 127]. In the TPX detector community, three high-Z compounds featuring sufficient material quality for sensor applications have recently

become available, GaAs, CdTe and CdZnTe[1]. These materials quickly were incorporated into several core application fields of hybrid pixel detectors, such as medical imaging and dose monitoring and even rendered new application fields possible, such as miniature particle trackers and Compton cameras with high stopping power.

In ATLAS, the measurement of X and $\gamma$-rays is important because they are among the most abundant particles of the radiation field during collisions (see figure 3.2.1 and section 4.5) and because they are an indicator of induced radioactivity. Since the 300 µm and 500 µm thick silicon sensors used in the ATLAS-TPX detector network have a low interaction cross-section for high energy photons, GaAs and CdTe sensors are good candidates for the network upgrade. Figure 4.1.1 compares the photon detection efficiency of different available sensors, which can be bump-bonded to either TPX or TPX3. In the displayed energy range, the dominant cross sections are those of photoelectric and Compton interactions, which can be identified by analyzing the shapes of recorded tracks (see section 2). Figure 4.1.1 shows that Si sensors are only sensitive to photons up to few tens of keV, while CdTe and CdZnTe sensors can reasonably detect $\gamma$-rays of few hundreds of keV. GaAs sensors are less sensitive to photons than CdTe sensors, nonetheless the sensor material is of particular interest since its higher electron mobility (see table 2.1.1) could be exploited with TPX3 in ATLAS to analyze radiation components on a bunch-by-bunch time scale (see section 4.5).

A large scale implementation of such sensors into long time experiments still requires additional thorough testing. A good knowledge of their homogeneity, time stability, CCE, energy resolution, and temperature sensitivity must be acquired. This is the subject of the two following publications. The assessed samples, a 500 µm thick GaAs and a 1 mm CdTe sensor, were obtained in 2016 through IEAP. The CdTe sensor was produced by Acrorad [129] and the GaAs sensor by the Tomsk State University [130]. For GaAs, the inherent EL2$^+$ trapping centers limiting electron lifetime in the material are filled by electrons of shallow donors (n-type doping), which are in turn compensated by deep acceptors (Cr) [131]. For this reason, this type of GaAs is usually referred to as GaAs:Cr. While both the CdTe and GaAs:Cr producers have been improving their crystal-growth processes during the last two

---

[1]Except for the sensor characterized in section 4.3, I include CdZnTe when I talk about CdTe since the photon cross sections are similar.
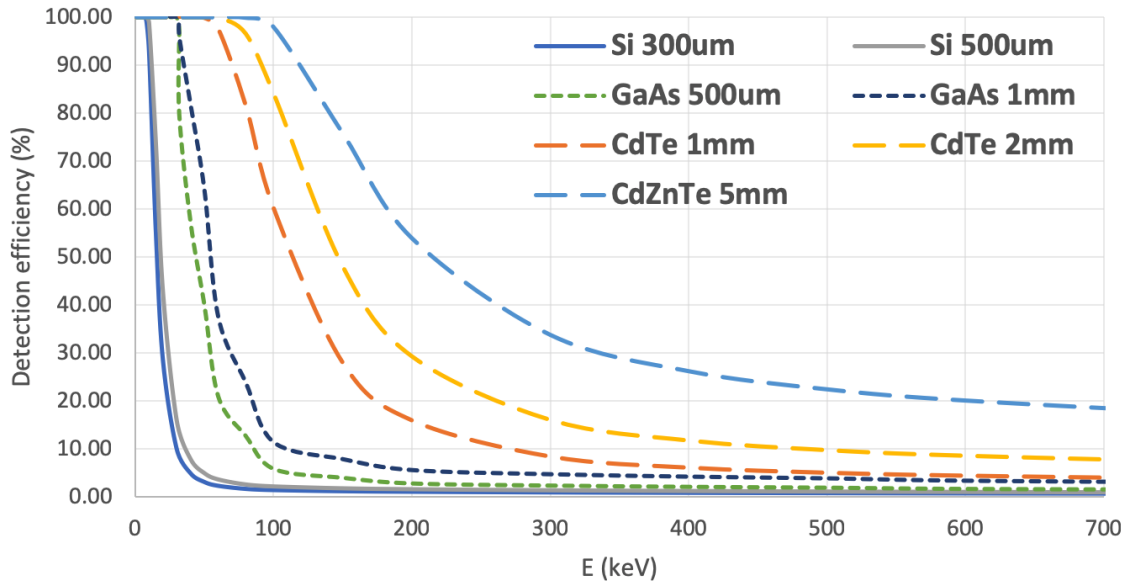
**Fig. 4.1.1.** Photon detection efficiency as a function of energy for different sensors currently available. The calculation is done for a photon arriving perpendicularly to the sensor surface, with data from Ref. [**128**]. Displayed sensors can be bump-bonded to either TPX or TPX3.

decades, tests of TPX and TPX3 detectors equipped with GaAs and CdTe sensors were reported only quite recently [**132, 133, 130, 134**].

## 4.2. Methodology

The material characterization provided by the manufacturers is typically slim, which is perhaps owed to the fact that the corresponding market is small and highly competitive. Once bonded to an ASIC, the possibilities to assess the whole detector unit depends on the electronic readout that is attached to the sensor. Standard preliminary tests of the sensor material include obtaining the I-V curve[2], giving an estimate of the leakage current and the type of contact at the electrode (e.g., ohmic or Schottky junction). The key parameter to investigate is the sensor CCE, which is affected by the presence of charge carrier trapping centers and is commonly represented by the $\mu\tau$ product (as discussed in chapter 2). This parameter is usually extracted by irradiating the sensor with particles having a short range in matter, such as alpha particles [**135**]. In medical and other high flux applications, a common problem found with compound semiconductors is short-scale time instabilities under strong

---

[2]Relation between applied voltage (V) and current (I).

X-ray irradiation, referred to as *polarization effects* [**136, 137**]. Another issue particularly affecting X-ray imaging with pixel detectors is the material inhomogeneity, which can be corrected to a certain extent by so-called flat-field and beam hardening corrections [**138**]. Inhomogeneities are also problematic for particle tracking, since the morphology of clusters can be altered, resulting for example in deteriorated dE/dx determination. In addition, the operation of high-Z detectors can be affected by leakage current, particularly when used under vacuum due to temperature effects. This leads to noisy response of pixels, causing false background signal which can be mis-identified as low energy electron or photon interactions in the detector.

The analysis performed in the publications provided within this study was subject to limitations in time and equipment. Indeed, only few detector units featuring high-Z sensors were available at IEAP at the time, and several groups (particle physics, medical imaging, space physics) were competing to test them in their respective radiation environments. For the CdTe Timepix detector (TPX-CdTe), the characterization was done at the University of Montreal, using radioactive sources ($^{241}$Am and $^{137}$Cs) and protons between 800 keV and 10 MeV from the Tandem Accelerator facility. Since the use of high-Z materials for radiation monitoring in ATLAS was one main concern of the current investigation, the time stability was assessed over a longer time period than is usually done to investigate polarization effects. Subsequently, the detector energy resolution was assessed with all available sources. Finally, the $\mu_e \tau_e$ product of the sensor was extracted using 800 keV protons. This source is convenient because it has a low range in sensors, and because the energy is low enough to avoid the saturation effect observed with TPX pixel amplifiers[3].

The GaAs:Cr TPX detector was characterized at IEAP. A Keithley source meter was used to obtain the I-V curve, thus verifying the ohmic resistivity claimed by the supplier and giving an estimate of the leakage current. Then, a Cd foil was bombarded by a X-ray tube to obtain a 23 keV mono-energetic X-ray source directed to the detector. This measurement allowed both a time stability verification over 3 hours and the extraction of $\mu_e \tau_e$ products. In contrast to an 800 keV proton, a 23 keV photon causes a single pixel event when hitting the center of a pixel area. Repeating the measurement with different biases, this feature was

---

[3]It has been observed that for deposited energies above $\sim$0.9 MeV inside a pixel, the TOT response is not linear anymore. See Ref. [**64**] for more details.

exploited to extract $\mu_e\tau_e$ for every single pixel. Beyond the measures described in literature, when fitting the Hecht equation, in this study, the small pixel effect was taken into account as well. As a result we obtain a very accurate CCE study over the whole sensor area, allowing for a comprehensive priori study of the detector tracking performance.

## 4.3. Publication: Characterization of a pixelated CdTe Timepix detector operated in ToT mode

My contributions to the publication:

- Data acquisition
- Development of the analytical methods
- Data analysis
- Authorship of the paper

C. Leroy helped with the development of the methods and the formulation of the paper. C. Papadatos supported the data taking and the data analysis. J.S. Roux supported the data analysis. S. Pospisil and M. Pichotka helped with the formulation of the paper.

# Characterization of a pixelated CdTe Timepix detector operated in ToT mode

*Thomas Billoud[1,*], Claude Leroy[1], Costa Papadatos[1], Martin Pichotka[2], Stanislav Pospisil[2] and Jean-Samuel Roux[1]*

[1]Groupe de Physique des Particules, Université de Montréal

[2]Institute of Experimental and Applied Physics, Czech Technical University in Prague

[*]Corresponding author

publication

### 4.3.1. Abstract

A 1 mm thick CdTe sensor bump-bonded to a Timepix readout chip operating in Time-over-Threshold (ToT) mode has been characterized in view of possible applications in particle and medical physics. The CdTe sensor layer was segmented into 256 x 256 pixels, with a pixel pitch of 55 $\mu$m. This CdTe Timepix device, of ohmic contact type, has been exposed to alpha-particles and photons from an $^{241}$Am source, photons from a $^{137}$Cs source, and protons of different energies (0.8 – 10 MeV) delivered by the University of Montreal Tandem Accelerator. The device was irradiated on the negatively biased backside electrode. An X-ray per-pixel calibration commonly used for this type of detector was done and its accuracy and resolution were assessed and compared to those of a 300 $\mu$m thick silicon Timepix device. The electron mobility-lifetime product ($\mu_e \tau_e$) of CdTe for protons of low energy has been obtained from the Hecht equation. Possible polarization effects have been also investigated. Finally, information about the homogeneity of the detector was obtained from X-ray irradiation.

### 4.3.2. Introduction

CdTe is a compound semiconductor material with a wide band gap energy ($E_g$= 1.47 eV), a high atomic number ($Z_{Cd} = 48$, $Z_{Te} = 52$), a high density ($\rho = 5.85$ g/cm$^3$) and high resistivity ($\geq 10^9$ $\Omega$.cm). Such properties allow the capability of operation at room temperature along with high detection efficiency for X-rays and gamma rays. When hybridized with a Timepix chip, the detector also benefits from the tracking capabilities and energy sensitivity of the pixels array. The high detection efficiency for photons is crucial for many applications such as medical imaging (SPECT and PET) or any physics experiments where the field of photons or photon background have to be investigated or monitored. However, it is known that CdTe detectors may suffer from incomplete charge collection due to traps inside the material, which causes lower energy resolution. Polarization effects have also been reported, which cause instabilities in the detector's response in time. This article presents some results of the characterization of a CdTe Timepix detector (TPX-CdTe) operated in Time Over Threshold (ToT) mode which permits the measurement of charge produced by radiation quanta in individual pixels. For this purpose, the detector was irradiated with alpha-particles and low energy photons from an $^{241}$Am source, high energy photons from a $^{137}$Cs source, and protons of energies in the 0.8 – 10 MeV range delivered by the University

of Montreal Tandem Accelerator (UMTA). These measurements also allowed one to assess the quality of the usual X-ray per-pixel calibration used for this type of detector for various levels of deposited energy.

The TPX-CdTe detector device is presented in section 4.3.3. Section 4.3.4 is dedicated to the description of the experimental set-up at the UMTA facility. The procedure of the per-pixel energy calibration is presented and discussed in section 4.3.5. Section 4.3.6 presents the detector energy resolution and its calibration's accuracy obtained from protons and photons measurements with a comparison to a 300 $\mu$m silicon Timepix detector (TPX-Si). In section 4.3.7, the Hecht equation fitted to low energy proton data allows the extraction of the electron mobility-lifetime product ($\mu_e\tau_e$) of the material. The homogeneity and time stability of the detector is investigated in section 4.3.8.

### 4.3.3. The CdTe Timepix detector device

The hybrid pixelated Timepix detector used in the present experiments consists of a ohmic-type CdTe sensor chip (1 mm thick layer with platinum contact on both surfaces) bump-bonded to a Timepix readout chip [107]. Processing and bump bonding was done by Freiburger Materialforschungszentrum (FMF) on a CdTe bulk material delivered by Acrorad [140]. The CdTe crystal was grown by the Traveling Heater Method (THM) technology. The sensor chip is equipped with a single common backside electrode and a front side matrix of electrodes (256 x 256 square pixels, each of 55 x 55 $\mu$m$^2$ area). On top of the backside Pt electrode (14 nm thick), a 7.6 $\mu$m thick parylene C coating is deposited. The thicknesses of these two backside layers were measured by Rutherford backscattering spectrometry with the University of Montreal Tandetron Accelerator. For the present study, a negative bias was applied on the backside electrode, electrons thus being collected on the pixel's side. Each pixel is connected to its respective preamplifier, discriminator with an adjustable threshold and digital counter, integrated on the readout chip. The threshold was set at 6.0 keV, below which a significant amount of noisy pixels appeared (in air, at room temperature). The device was operated in Time-over-Threshold (ToT) mode, which uses the clock and counter to determine the time the amplifier pulse has been over the pre-set threshold. This capability allows direct measurement of the energy deposited by a charged particle in each pixel. The data are recorded as images called frames that contain the ToT value of all pixels after a

given exposure time. The shapes of clusters of illuminated pixels are visible as tracks in the recorded frames. For highly ionizing particles striking the sensitive volume, the large concentration of electron-hole pairs generated in the pixelated device can create distortions of the electric field along the ionizing path, influencing charge collection and its lateral charge spread. This is caused, in addition to diffusion, by several drift processes, namely a plasma effect, charge column erosion and funneling [141, 142]. This lateral charge spread is responsible for a sharing of the charge among adjacent pixels, resulting in different track patterns for different interacting particles depending on their types, energies, incidence angles, and the nature of their interactions in the sensor. This is illustrated in figure 4.3.1 with tracks left by 2 MeV and 10 MeV protons hitting the detector's backside perpendicularly. The following terms will be used in the text to characterize tracks: the cluster size is the number of pixels forming the track, the cluster volume is the sum of per-pixel energies and the cluster height is the highest pixel energy. Recognition of the track shape makes particle identification possible [112]. The detector is fully controlled via a USB2 based readout interface [143] and the Pixelman software [144].
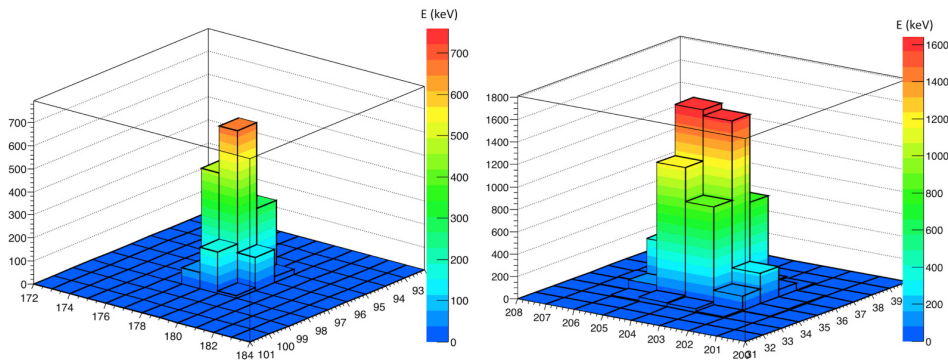


**Fig. 4.3.1.** Tracks left by a 2 MeV (left) and a 10 MeV (right) proton on TPX-CdTe. The applied bias is −300 V and protons hit the sensor's surface perpendicularly. X and Y axes are pixel coordinates. E is the deposited energy per pixel.

### 4.3.4. Experimental setup

The measurements were performed at the UMTA facility. For its operation, the TPX-CdTe detector device was located in a vacuum chamber (pressure of $\sim 10^{-7}$ Torr) of the

accelerator. The device was struck by protons from Rutherford Backscattering (RBS) on a 0.12 $\mu$m thick gold foil. The beam had energies from 800 keV up to 10 MeV. The protons struck the detector's surface perpendicularly. The device was also exposed successively to two radioactive sources ($^{241}$Am, $^{137}$Cs) mounted on a holder placed inside the chamber. The $^{241}$Am and $^{137}$Cs sources were aligned with the center of the detector at a distance of 1.5 cm and 1.2 cm, respectively. As the CdTe detector was showing large noise when operated at high voltage values (up to $-400$ V) in vacuum, the Timepix chip rested on a 5 mm thick copper layer in contact with the mounting system to allow thermal conductivity. The detector exposure time to incoming radiation was set to values short enough to avoid large track overlaps. The set of measurements used for the assessment of energy resolution and accuracy (section 4.3.6) was also done using a silicon Timepix detector (TPX-Si) for comparison. This TPX-Si detector is made of a 300 $\mu$m thick silicon sensor, reversely biased with a positive voltage on the backside electrode (1 $\mu$m thick Al layer). It was controlled and powered through a Fitpix interface [143]. It was calibrated with the same method as TPX-CdTe (see section 4.3.5), with an energy threshold of 5.4 keV. Its IKrum (current controlling the preamplifier pulse return to 0) digital value was 1 and its clock frequency (generating the ToT value) was 9.6 MHz. For TPX-CdTe, IKrum was 5 and the clock frequency was 48 MHz. TPX-CdTe and TPX-Si were both irradiated on the backside. In the following, $E_{beam}$ represents proton energies before they hit the gold foil. The proton energies corrected for energy loss in the gold foil ($E_{RBS}$) and deposited energies in the sensors' active volumes at the selected angle ($E_d$, corrected for energy loss in the dead layers) are given in section 4.3.6. In the present study, selected proton energies were such that the protons were entirely stopped inside the detectors' sensor layers (some examples of ranges are reported in Table 4.3.1). X-ray data used for calibration (section 4.3.5), energy resolution measurements (section 4.3.6) and homogeneity studies (section 4.3.8) were taken at the Institute of Experimental and Applied Physics, Prague.

### 4.3.5. Calibration

The detector was calibrated using the per-pixel X-ray calibration presented in [146]. This method, despite being time-consuming compared to an automated test pulse technique, is known to be the most precise [147]. The detector is irradiated with several X-ray sources

**Tab. 4.3.1.** Proton range in Si and CdTe for some energies used in the present study [145]. Semiconductor thicknesses are 300 $\mu$m for TPX-Si and 1000 $\mu$m for TPX-CdTe.

| Proton Energy (MeV) | Range in Si ($\mu$m) | Range in CdTe ($\mu$m) |
|:---:|:---:|:---:|
| 0.8 | 12 | 9 |
| 1.5 | 30 | 22 |
| 3 | 92 | 63 |
| 7 | 383 | 241 |
| 10 | 709 | 432 |

of energy below $\sim$60 keV, resulting mostly in single pixel clusters and thus allowing the individual calibration of every pixel. The relation between per-pixel ToT and deposited energy ($E_d$) is found to be non-linear for energies below $\sim$20 keV, and linear above that value. The calibration curve is obtained by fitting the following surrogate function (eq. 4.3.1) to the individual pixel response measured with different monoenergetic sources:

$$ToT = aE_d + b - \frac{c}{E_d - t} \; , \tag{4.3.1}$$

where a, b, c, and t are the coefficients to be extracted from the fit. X-rays of an $^{241}$Am source (59.5 keV), and X-ray fluorescence of Cd (23.2 keV) and Zn (8.6 keV) were used for TPX-CdTe. For TPX-Si, X-rays of $^{241}$Am (59.5 keV), and X-ray fluorescence of Cu (8.1 keV), Zr (15.8 keV) and In (24.2 keV) were used instead. The X-ray fluorescence was induced by means of an Amptek Mini-X X-ray tube for both detectors. During these measurements, TPX-CdTe was operated at $-300$ V and TPX-Si at 90 V. Figure 4.3.2 illustrates the fitted calibration curve for a random pixel of TPX-CdTe. Photons above $\sim$60 keV leave tracks larger than one pixel, which cannot be used for calibrating every pixel individually. The use of the per-pixel calibration for higher deposited energies is assessed in section 4.3.6.

Noteworthy is the so-called saturation effect of the Timepix front-end electronics for highly ionizing particles such as protons used in this study. It was demonstrated in [148] that, for silicon TPX detectors, the response to per-pixel energy deposits above $\sim$900 keV results in the distortion of the Gaussian shape of cluster volume distributions. This effect was observed in our measurements with protons, as can be seen in figure 4.3.3 a) showing
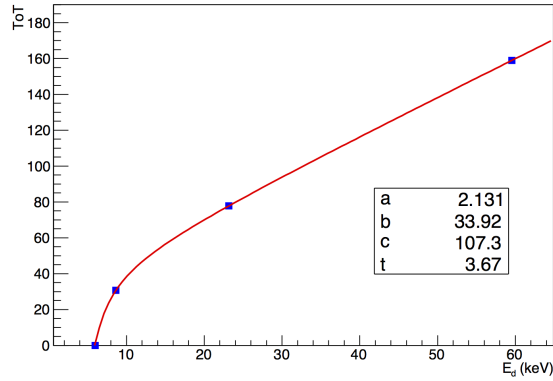
**Fig. 4.3.2.** Per-pixel calibration curve for a random pixel of TPX-CdTe. Spectral peaks of Zn (8.6 keV) and Cd (23.2 keV) fluorescence, $^{241}$Am (59.5 keV) X-rays and threshold energy (6.0 keV) are used for the fit with the ToT surrogate function (eq. 4.3.1). Error bars (errors on the means as calculated by Minuit-Migrad) are not visible.

TPX-Si cluster volume spectra for protons of different energies. The corresponding mean cluster height is 459 keV for 1 MeV, 740 keV for 2 MeV and 994 keV for the 3 MeV distorted spectrum. This is consistent with observations in [**148**], where a distorted cluster volume spectrum is obtained with 5.5 MeV alpha particles forming clusters with heights of ∼0.9 MeV. In addition to the distortion effect seen with 3 MeV protons, it can also be observed in figure 4.3.3 a) that as energy increases, resolution deteriorates and the response is shifted towards lower energies. For comparison, responses of TPX-CdTe to different proton energies up to 10 MeV are illustrated in figure 4.3.3 b). It is observed that Gaussian shapes are unaffected by distortion, even though resolution also deteriorates and peaks are also shifted to lower energies as energy increases. The cluster height for 10 MeV protons is 1753 keV, which is much higher than the distortion limit for TPX-Si. The 18% lower collected charge by TPX-CdTe due to the higher mean energy for electron-hole pair creation ($\varepsilon$) of CdTe compared to Si (4.43 eV for CdTe, 3.62 eV for Si [**149**]) does not account for such a difference. Moreover, TPX-CdTe has full charge collection at $-300$ V (see Hecht plot in section 4.3.7). Possible explanations could be the different electronic settings between the two detectors (e.g., IKrum, bias polaritiy) or recombination effects in CdTe during the charge carriers lateral spread and drift. A detailed study of this phenomenon will be done in the future.

Even though a solution has been proposed to correct for the distortion effect [148], it was not used in the present work.
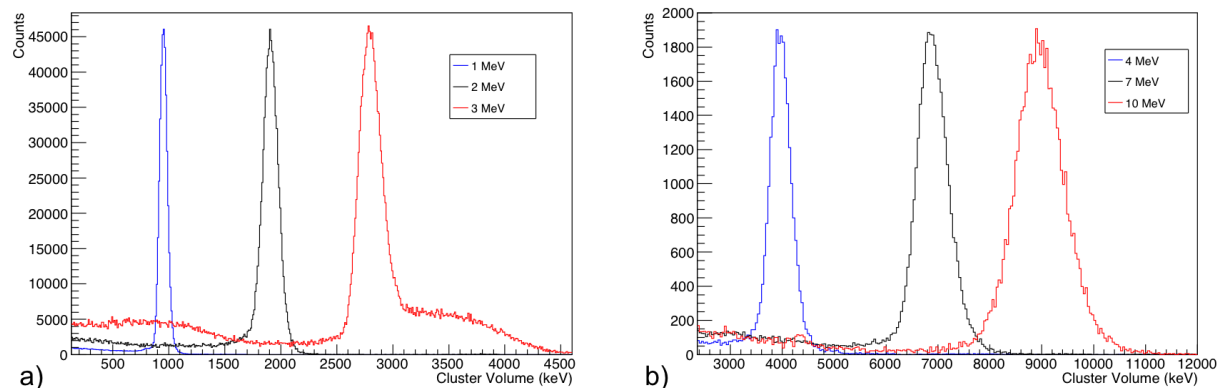


**Fig. 4.3.3.** Proton spectra for different energies with a) TPX-Si operated at 100V and b) TPX-CdTe operated at $-300$ V. For each figure, the spectra y-axis are scaled according to the lowest energy proton peak. Cluster volumes are computed using each detector's specific per-pixel calibration, as described in the text.

### 4.3.6. Energy resolution

Several effects affecting charge collection in CdTe sensors are expected to deteriorate their energy resolution, such as polarization or inhomogemeities inside the active volume. To assess the importance of these effects in our detector, we compared its resolution to that of a silicon Timepix detector (TPX-Si). The relative resolution (R) is usually expressed with the ratio of the Full Width at Half Maximum (FWHM) to the deposited energy ($E_d$). When particles are fully stopped inside the detector's active volume, the theoretical limit of energy resolution (Fano resolution) is given by the Fano factor (F), the deposited energy and the number of charge carriers created ($E_d/\varepsilon$). A Fano factor of 0.06 for CdTe and Si has been reported in literature [150]. In practice, the electronic noise ($\text{FWHM}_{elec}$) also deteriorates the resolution. In the case of a Timepix chip, $\text{FWHM}_{elec}$ accounts for the ToT fluctuations in each pixel of a cluster, and hence depends on the cluster size. The cluster size, in turn, depends on the energy threshold and applied bias (when charge sharing is present). Including the noise due to the various effects of defective charge collection ($\text{FWHM}_{CC}$), the FWHM can be expressed by [150]:

$$FWHM = \sqrt{8\ln{(2)}\varepsilon F E_d + FWHM_{CC}^2 + FWHM_{elec}^2}\,. \qquad (4.3.2)$$

Supposing that $FWHM_{CC} = 0$ for TPX-Si, its value for TPX-CdTe can be estimated if $FWHM_{elec}$ is the same for both detectors. For this reason, a bias of 100 V was chosen for TPX-Si measurements of protons because it resulted in cluster sizes as close as possible to that of TPX-CdTe, operated at $-300$ V, for all energies (within 15%). Comparisons of measured resolution for different deposited energies ($E_d$) are reported in Table 4.3.2 for protons and Table 4.3.3 for photons. For protons, the beam energy ($E_{beam}$) and beam energy corrected for energy loss inside the gold foil ($E_{RBS}$) are indicated, and $E_d$ differs from $E_{RBS}$ because $E_d$ is corrected for energy loss inside the dead layer. The accuracy of the per-pixel calibration is also reported in both tables, using the deviation (Dev) of the measured energy ($E_m$) from the calculated energy ($E_d$):

$$Dev(\%) = 100 \times \frac{E_m - E_d}{E_d}\,. \qquad (4.3.3)$$

It can be noted that the theoretical Fano resolutions are two orders of magnitude higher than the measured resolutions. For example, the calculated Fano resolution for 1 MeV protons is 0.1% for Si, whereas a resolution of 8.6% is measured. This indicates that the first term in eq. 4.3.2 is negligible compared to $FWHM_{elec}$ and, in the case of TPX-CdTe, to $FWHM_{CC}$. For protons up to 3 MeV, it is observed that TPX-Si has a better resolution than TPX-CdTe. Above 3 MeV, however, TPX-Si is affected by the distortion effect, as discussed in section 4.3.5. For TPX-CdTe, the best resolution is achieved with 7 MeV protons, above which saturation of the electronics starts to broaden spectra. For photons, TPX-Si also has better resolutions. For the 59.5 keV peak of $^{241}$Am, its resolution is better than that of TPX-CdTe by a factor of 2.6. Even though the different calibrations and electronic configurations (e.g., IKrum, energy thresholds) of the two detectors might cause differences between their $FWHM_{elec}$ noise, the significantly lower resolution of TPX-CdTe is a sign of defective charge collection effects in the CdTe sensor.

### 4.3.7. Electron mobility-lifetime product

Trapping effects are expected at various levels in compound semiconductor materials such as CdTe. It is important to estimate these effects as they are responsible for incomplete

**Tab. 4.3.2.** Comparison of TPX-CdTe and TPX-Si energy measurements for protons of different energies. Beam energy ($E_{beam}$), beam energy corrected for energy loss inside the gold foil ($E_{RBS}$) and energy deposited in the sensor's active volume ($E_d$, corrected for energy loss inside the dead layers using SRIM data [**145**]) are reported. Dev is the deviation of $E_m$ from $E_d$ and R is the relative resolution. Bias voltages are $-300$ V and $100$ V for TPX-CdTe and TPX-Si, respectively.

| $E_{beam}$ | $E_{RBS}$ | TPX-CdTe | | | | TPX-Si | | | |
|---|---|---|---|---|---|---|---|---|---|
| | | $E_d$ | $E_m$ | Dev | R | $E_d$ | $E_m$ | Dev | R |
| (keV) | (keV) | (keV) | (keV) | (%) | (%) | (keV) | (keV) | (%) | (%) |
| 800 | 769 | 446 | 430 | -3.7 | 18.8 | 713 | 734 | 2.8 | 8.6 |
| 1500 | 1468 | 1282 | 1403 | 8.6 | 12.8 | 1431 | 1461 | 2.1 | 8.3 |
| 3000 | 2958 | 2849 | 2992 | 4.8 | 12.3 | 2935 | 2802 | -4.7 | 9.6 |
| 5000 | 4941 | 4869 | 4921 | 1.1 | 11.2 | - | - | - | - |
| 7000 | 6923 | 6867 | 6891 | 0.4 | 10.1 | - | - | - | - |
| 9000 | 8904 | 8858 | 8405 | -5.4 | 11.1 | - | - | - | - |
| 10000 | 9894 | 9852 | 8951 | -10.1 | 12.4 | - | - | - | - |

charge collection. For this purpose, a widely used method is the extraction of the charge carrier's mobility-lifetime product from a fit based on the Hecht equation [**58**]. This relation gives the collected charge (Q) in terms of the applied bias (V) and the depth of interaction. We used protons with the lowest available energy (800 keV) to extract the electron mobility-lifetime ($\mu_e \tau_e$) of our CdTe sensor. For this beam energy, protons are slowed down to 457 keV after crossing the dead layer (see Table 4.3.2), and have a negligible range in the CdTe bulk (about 4 $\mu$m) compared to the sensor thickness. Assuming a uniform electric field, the Hecht equation can then be simplified to:

$$Q(V) = Q_0 \left( \frac{\mu_e \tau_e}{d^2} \right) (V - V_0) \left( 1 - e^{\frac{d^2}{\mu_e \tau_e (V - V_0)}} \right) , \qquad (4.3.4)$$

where $Q_0$ is the deposited charge inside the detector's active volume and $V_0$ accounts for the systematic error on the applied bias through the USB2 interface. Assuming that our calibrated signal is proportional to the collected charge, we can fit the cluster volume

**Tab. 4.3.3.** TPX-CdTe and TPX-Si energy measurements for X-ray fluorescence sources used for calibration, $^{241}$Am X-rays and $^{137}$Cs photopeak (observed only with TPX-CdTe). Energy deposited in the sensor's active volume ($E_d$), measured energy ($E_m$), deviation of $E_m$ from $E_d$ (Dev) and relative resolution (R) are reported. Bias voltages are $-300$ V and 90 V for TPX-CdTe and TPX-Si, respectively.

| | TPX-CdTe | | | TPX-Si | | |
|:---:|:---:|:---:|:---:|:---:|:---:|:---:|
| $E_d$ (keV) | $E_m$ (keV) | Dev (%) | R (%) | $E_m$ (keV) | Dev (%) | R (%) |
| 8.1 (Cu) | - | - | - | 8 | 1.2 | 20.8 |
| 8.6 (Zn) | 8.3 | -3.6 | 36.7 | - | - | - |
| 15.8 (Zr) | - | - | - | 15.9 | 0.4 | 27.2 |
| 23.2 (Cd) | 23.4 | 0.6 | 42.9 | - | - | - |
| 24.2 (In) | - | - | - | 23.7 | 2.2 | 33.8 |
| 59.5 ($^{241}$Am) | 60.1 | 1.0 | 26.2 | 59.1 | 0.7 | 10.2 |
| 661.7 ($^{137}$Cs photopeak) | 709.3 | 7.2 | 10.1 | - | - | - |

as a function of applied bias using eq. 4.3.4 in order to obtain the $\mu_e \tau_e$ product without the knowledge of the true collected charge. This is illustrated in figure 4.3.4. A $\mu_e \tau_e$ value of $4.98 \pm 0.02 \cdot 10^{-4}$ cm$^2$ V$^{-1}$ is obtained, which is slightly lower than values found in literature for THM grown CdTe [**135, 151, 152, 153, 154**].

### 4.3.8. Polarization and homogeneity studies

It is expected that compound semiconductors such as CdTe are subject to polarization effects, possibly caused by the presence of deep, long-lived traps that perturb and distort the local electric field, leading to time dependent counting rate and charge collection efficiency (see [**155, 156**], for instance). Polarization effects were observed in [**157**] and [**158**] for ohmic-like contact pixelated CdTe detector bonded to a Timepix chip. To investigate this problem, our TPX-CdTe detector was exposed to alpha-particles from an $^{241}$Am source over a period of 38 hours in a vacuum of $5 \cdot 10^{-7}$ Torr. A bias of $-150$ V was applied over the course of the measurement, the detector being too noisy at $-300$ V (voltage used for calibration) after few hours in vacuum. As documented in figure 4.3.4, the charge collection efficiency is
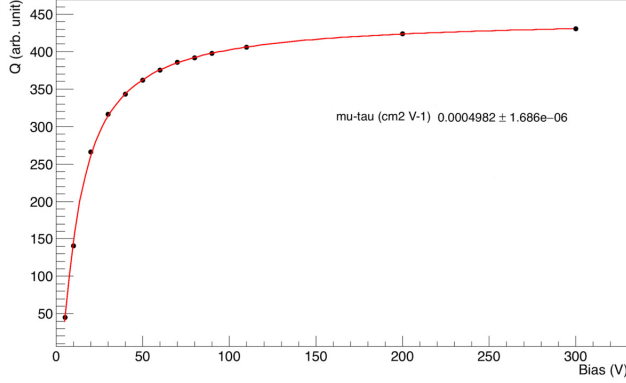
**Fig. 4.3.4.** Collected charge (arbitrary units) as a function of bias for TPX-CdTe irradiated with 800 keV protons. The collected charge is assumed to be proportional to cluster volumes obtained with the per pixel calibration. Error bars (errors on the means as calculated by Minuit-Migrad) are not visible.

not significantly changed between these two biases. The energy resolution shows a very good time stability, as seen in figure 4.3.5 a). In that figure, the $^{241}$Am spectra measured over 36 hours under continuous bias application are observed in complete overlap, confirming results reported in [140]. However, although no fluctuations were observed in cluster volumes, a slight increase in cluster sizes was noticed (figure 4.3.5 b)). Following the approach of [155], the relation between cluster size and applied bias was used to calculate the effective bias evolution over time, which is shown in figure 4.3.6. The effective bias is reduced by no more than 15V. The major variation occurs only within the first 17 hours, after which the bias appears to stabilize for a time until a moderate decrease resumes at 29 hours. This result supports the existence of moderate polarization effects affecting the detector over the considered time range.

The homogeneity of our TPX-CdTe detector was also investigated, as distortion in radiation measurements have been linked to non-uniformities in the device material [158]. This was done by measuring the integrated counts and average deposited energy in each pixel for X-ray data sets (the large tracks of protons and alpha particles are less efficient to unveil small-scale defects). The results obtained with X-rays from Cd fluorescence are illustrated in figure 4.3.7, where only single pixel clusters have been selected. It should be noted that the three black columns seen in figures 4.3.7 a) and b) are masked pixels due to defective bump

83

a)       b)
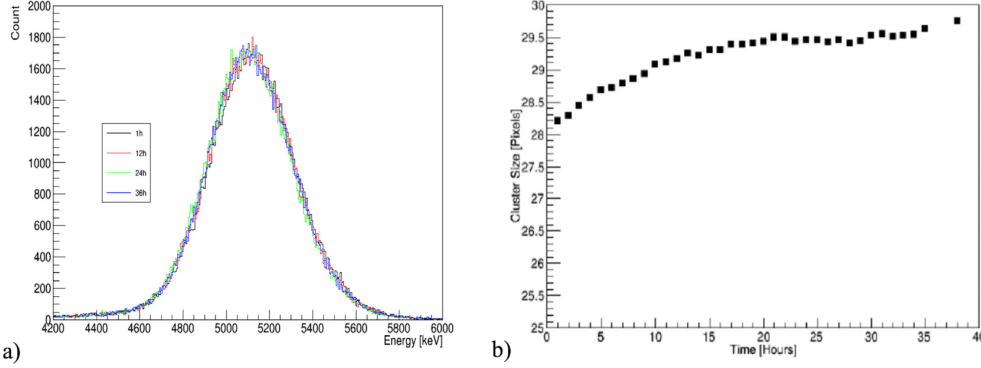
**Fig. 4.3.5.** Energy spectra of 5.5 MeV alpha particles as a function of time for TPX-CdTe exposed to $^{241}$Am. The spectra were measured over 36 hours under continuous bias application. b) Cluster size of 5.5 MeV alpha particles as a function of time for TPX-CdTe exposed to $^{241}$Am alpha-particles.
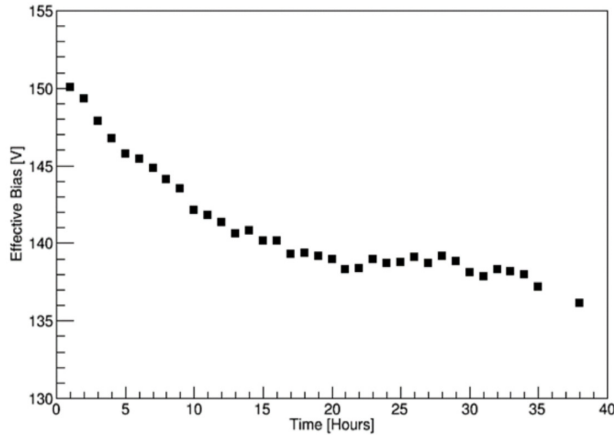


**Fig. 4.3.6.** The behaviour of the effective bias with time, calculated from the dependence of the cluster size on time and bias.

bonding, and that the black spot on top of figure 4.3.7 a) is due to the bias wire bond, which do not correspond to material inhomogeneities. Three types of defects can be identified in figure 4.3.7 a). 1) Lines crossing the detector where counts are higher (e.g., area surrounded by a dotted rectangle) and lines where the counts are slightly lower on one side and higher on the other (e.g., areas surrounded by a dotted circle). These types of defects were also observed in [**127**], where they have been linked to dislocations acting as current transport ducts. 2) Clusters of few pixels with no counts surrounded by pixels with high count rates

(e.g., area surrounded by a full-line rectangle). They are clusters of pixels that were masked before measurement because they were identified noisy regions. These high leakage current sources were observed and investigated in [158], where it is suggested that they represent local electric field distortions around Te inclusions close to the backside electrode. 3) Clusters of few pixels with very low count rates (e,g., area surrounded by a full-line circle), which represent regions with lower charge collection. As seen in figure 4.3.7 b), only the second type of defects has a significant impact on the per-pixel deposited energy measurement, as can be expected from calibrated data. Indeed, the per-pixel calibration corrects for variations of charge collection between pixels (if charge collection is constant over time and not too low), and only masked pixels cause inhomogeneities in spectral information over the detector's surface.
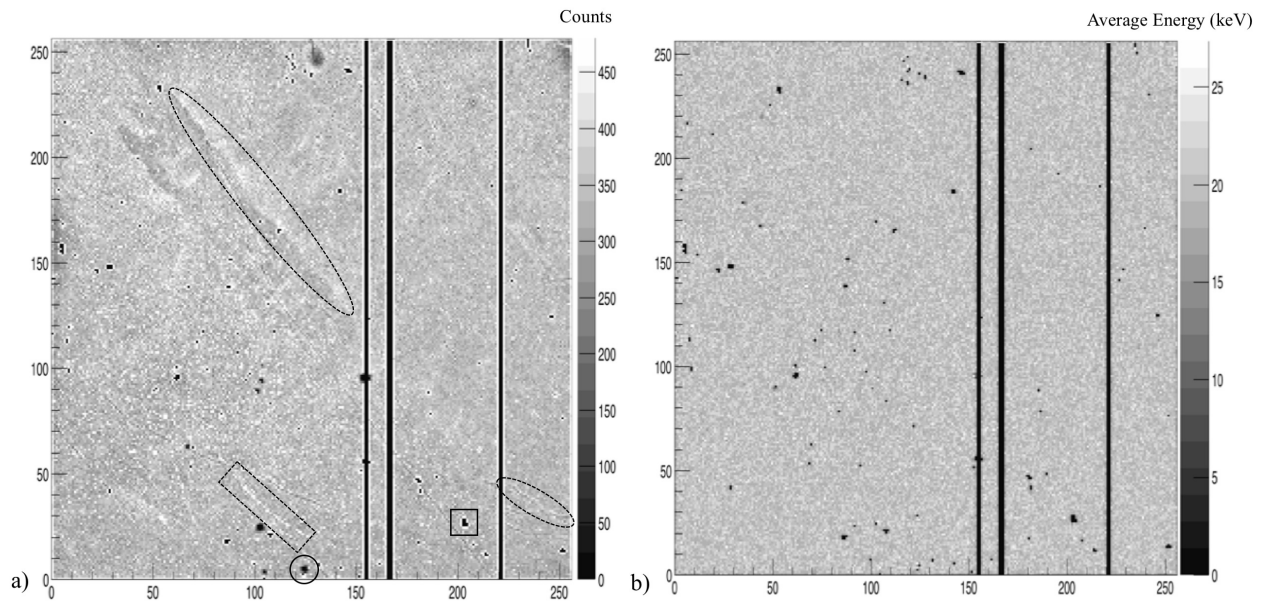


**Fig. 4.3.7.** Response of TPX-CdTe to X-rays from Cd fluorescence. a) Total number of single pixel clusters. b) Average energy of single pixel clusters. The detector was operated at $-300V$ during $\sim45$ mn with an acquisition time of 1 ms.

### 4.3.9. Summary and conclusion

The energy sensitivity of a Timepix detector hybridized with a ohmic-type CdTe sensor was characterized with alpha-particles and photons from an $^{241}$Am source, photons from a $^{137}$Cs source, and protons of various energies below 10 MeV. The relative resolution of the

CdTe detector was found to be lower than that of a 300 $\mu$m thick silicon Timepix detector. A mobility-lifetime product of $4.98\pm0.02 \cdot 10^{-4}$ cm$^2$ V$^{-1}$ was obtained for electrons by fitting the Hecht equation to 800 keV proton data. The good time stability of the detector was confirmed with alpha energy spectra. Irradiation with high fluxes of X-rays unveiled small-scale non-uniformities over the sensor's surface.

The results of this investigation reflect good progress made on the quality of the manufactured CdTe material over the years [132], which opens the possibility to use TPX-CdTe detectors in a wide range of applications. Their integration in medical imagers and Compton cameras (as absorber and scatter plane) or their use for the monitoring of photon fields at hadron therapy centers are known examples. TPX-CdTe can also be applied in particle physics experiments where photons are either an important component of the radiation field to be measured or the trace of induced radioactivity which contributes to the experimental background. Another possible application of TPX-CdTe in particle physics is the search of neutrinoless double beta decay with $^{116}$Cd and $^{130}$Te [133]. Here, it can be used both as a source and a detector, avoiding the need for a source foil surrounded by other types of detectors. The excellent tracking capabilities of the Timepix chip combined with its energy sensitivity are powerful tools for dissociating events of interest from background [159, 160]. In this case, the use of telescopes with two TPX-CdTe devices facing each other would permit an increase in statistics and tracking efficiency.

### 4.3.10. Acknowledgments

## 4.4. Publication: Homogeneity study of a GaAs:Cr pixelated sensor by means of X-rays

My contributions to the publication:

- Data acquisition
- Development of the analytical methods
- Data analysis
- Authorship of the paper

C. Leroy helped with the development of the methods and the formulation of the paper. C. Papadatos and J.S. Roux supported the data analysis. S. Pospisil and M. Pichotka helped formulating the paper.

# Homogeneity study of a GaAs:Cr pixelated sensor by means of X-rays

*Thomas Billoud[1,\*], Claude Leroy[1], Costa Papadatos[1], Martin Pichotka[2], Stanislav Pospisil[2] and Jean-Samuel Roux[1]*

[1]Groupe de Physique des Particules, Université de Montréal

[2]Institute of Experimental and Applied Physics, Czech Technical University in Prague

[\*]Corresponding author

publication

### 4.4.1. Abstract

Direct conversion semiconductor detectors have become an indispensable tool in radiation detection by now. In order to obtain a high detection efficiency, especially when detecting X or $\gamma$ rays, high-Z semiconductor sensors are necessary. Like other compound semiconductors GaAs, compensated by chromium (GaAs:Cr), suffers from a number of defects that affect the charge collection efficiency and homogeneity of the material. A precise knowledge of this problem is important to predict the performance of such detectors and eventually correct their response in specific applications. In this study we analyse the homogeneity and mobility-lifetime products ($\mu_e \tau_e$) of a 500 $\mu$m thick GaAs:Cr pixelated sensor connected to a Timepix chip. The detector is irradiated by 23 keV X-rays, each pixel recording the number of photon interactions and the charge they induce on its electrode. The $\mu_e \tau_e$ products are extracted on a per-pixel basis, using the Hecht equation corrected for the small pixel effect. The detector shows a good time stability in the experimental conditions. Significant inhomogeneities are observed in photon counting and charge collection efficiencies. An average $\mu_e \tau_e$ of $1.0 \cdot 10^{-4}$ $cm^2 V^{-1}$ is found, and compared with values obtained by other methods for the same material. Solutions to improve the response are discussed.

### 4.4.2. Introduction

The use of high-Z compound semiconductors for radiation detection has been investigated for several decades [162, 163, 149, 53], especially due to their high resistivity and high sensitivity to X and $\gamma$ rays. Their bonding to high-end pixelated chips such as Timepix [107] offers the possibility of particle tracking and spectrally sensitive high resolution imaging. However, the production of high quality compound semiconductors still remains a challenge that makes the use of such detectors relatively recent. In particular, the presence of material defects deteriorates the response homogeneity of the pixelated detector and is subject to thorough investigations [164, 165]. A good knowledge of this phenomenon is important to predict the performance of the detector in specific applications and allows, in some cases, the development of methods to correct for it. In this work, we present a detailed study of these effects on a Timepix detector bump-bonded to a 500 $\mu$m thick GaAs sensor ($Z_{Ga} = 31$, $Z_{As} = 33$). The material is chromium compensated and obtained by liquid encapsulated Czochralski growth in the Tomsk State University.

In order to characterize the sensor homogeneity with a resolution of 55 $\mu m$ (i.e the pixel pitch), the detector is irradiated by 23 keV X-rays. At this energy, a photon interacting in the pixel center creates a single signal on the opposite amplifier (this will be referred to as a "hit"), whereas higher energy particles typically induce charge on several adjacent pixels ("cluster"). This way, each pixel is used as an X-ray detector by itself and records the charge induced by each interaction, thus allowing the reconstruction of its energy spectrum. After describing the methods, we briefly discuss the time stability of the detector. We then analyse the homogeneity of the photon counting efficiency and induced charge consecutively. Finally, the distribution of $\mu_e \tau_e$ products over the sensor area is presented and linked with inhomogeneities in the detector response. Although $\mu_e \tau_e$ mapping has already been reported using identical detectors [166], we here take into account the small pixel effect in the Hecht equation to improve the precision of the parameters extracted from the fit.

### 4.4.3. Methods

#### 4.4.3.1. *Detector and set-up*

The 500 $\mu$m thick GaAs:Cr sensor used in this study is of ohmic type, with a 1 $\mu$m thick nickel electrode on the backside. The linearity of its IV curve was verified using a Keithley source meter at room temperature, from -300 V up to 300 V, as shown in fig 4.4.1 a). The resistivity obtained from this data is 2.0 GΩcm, which is in agreement with values given by the manufacturer [164]. On the front side, the sensor is bump-bonded to a Timepix chip, dividing the surface into a matrix of 256 x 256 pixels, each with a 55 $\mu$m pitch. Every pixel includes a preamplifier and a discriminator, which are used to measure the time during which the pulse of an interacting particle is over an adjusted threshold. This so-called "time-over-threshold" (TOT) can then be related to the deposited energy by an appropriate calibration. The TOT is recorded within constant time intervals, called frames, when all pixels are active. Its value is given in units of clock periods, whose frequency was set to 50 MHz. A threshold equalization was done using the Pixelman interface [144] in order to make the thresholds as homogeneous as possible. Even though the remaining non-uniformity of the pixel channels contribute to the inhomogeneity of the detector response [107], it causes random fluctuations which are negligible with respect to those from GaAs defects, as will be seen in section 4.4.4.3. The thresholds were set just above electronic noise, which corresponded to 3 keV.
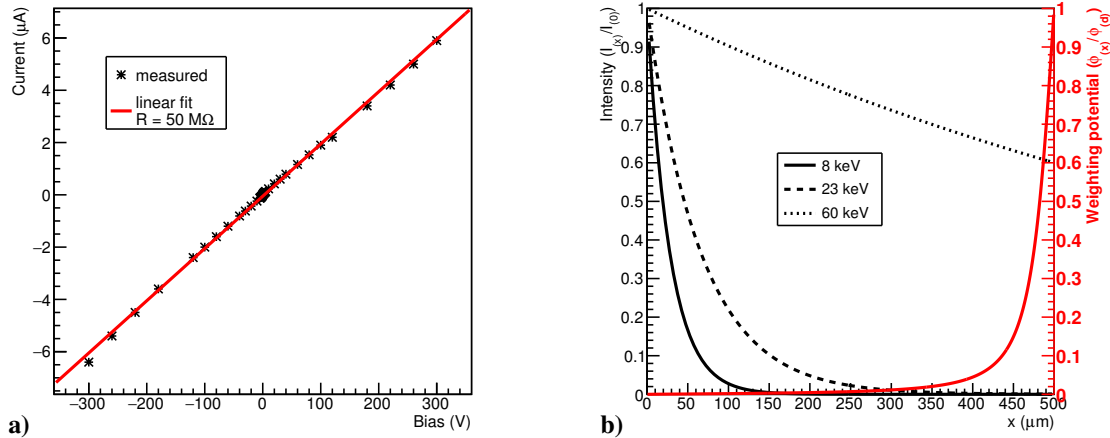
**Fig. 4.4.1.** a) IV curve of the GaAs:Cr sensor obtained with a Keithley source meter at room temperature, with a linear fit and the resulting resistance. b) Penetration curves (black) of 8 keV, 23 keV and 60 keV X-rays in a 500 $\mu$m thick GaAs layer and weighting potential [**56**] (red) for a charge carrier traveling along the center of a pixel. $I_{(x)}/I_{(0)}$ is the fraction of photons left at a depth $x$ in the sensor from an incoming intensity $I_{(0)}$.

For the purpose of Hecht fitting, the detector was energy calibrated at -300 V using the method presented in [**167**], where every pixel is calibrated individually using monoenergetic X-rays. In this procedure, only single pixel hits are taken into account, each pixel being used as an independent X-ray detector. Cluster events, occurring when the charge carrier cloud generated by an X-ray interaction spreads at the frontier between adjacent pixels, are rejected. For each pixel, the relation between TOT and energy is linear, except for energies close to the threshold. The calibration curve is thus obtained from two energy points in the linear region and one point close to the 3 keV threshold. For this purpose, the detector was irradiated by the fluorescence photons of 8 keV and 23 keV from Cu and Cd emission, respectively, and the 60 keV gamma rays of a $^{241}$Am source. The fluorescence was produced by means of an Amptek Mini-X X-ray tube, with the detector facing the irradiated foils. Figure 4.4.1 b) shows the penetration curves of the three photon sources into GaAs (from data in [**128**]). The results of the calibration are illustrated in figure 4.4.2 with the calibrated spectra of the 8 keV and 23 keV source at -300 V, taking into account only single pixel hits. The low energy peak in the 23 keV spectrum corresponds to the escape peaks of Ga and As.
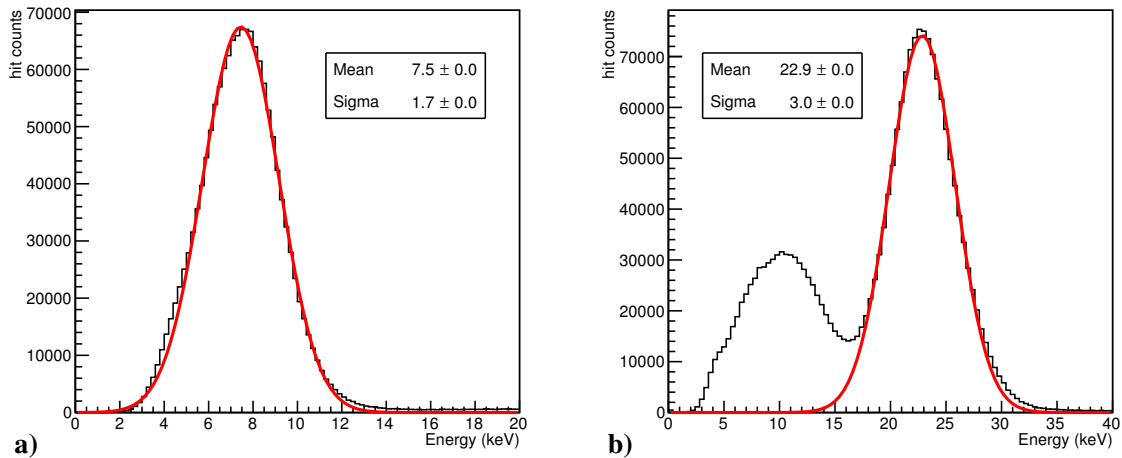
**Fig. 4.4.2.** X-ray spectrum of the 8 keV (a) and 23 keV (b) source obtained from Cu and Cd fluorescence emission, respectively, using the per-pixel calibration. Only single pixel hits are taken into account. Gaussian fits are displayed in red, along with the fit parameters.

For reasons explained in the next subsection, the 23 keV source was selected for the entire study presented in section 4.4.4. As in the calibration procedure, only single pixel hits were kept for this study, in order to reconstruct a well defined spectrum for each pixel. At -300 V, hits represented 32 % of the total number of events (2 pixels clusters being the dominant size), against 19 % at -30 V due to an increased charge sharing effect [**142**]. The analysis was done using the Mafalda framework[4], a C++ and ROOT [**168**] based code adapted to Pixelman, fits being performed with the ROOT Minuit-Migrad algorithm. The detector was cooled by a fan and its data was acquired using the Fitpix readout interface, [**143**] with frames of few milliseconds. With X-ray fluxes of the order of $10^5$ $cm^{-2}s^{-1}$, the dead time between two frames was ~50 ms, such that measurements (acquiring data from 65k pixels as individual spectroscopic chains) lasted several hours for each selected bias. With more recent readout interfaces [**169**] [**170**], or the more recent Timepix3 chip [**119**], the measuring time could be significantly reduced.

---

[4]Available at https://github.com/idarraga/mafalda

### 4.4.3.2. *Hecht equation and small pixel effect*

The Hecht equation is commonly used to extract the mobility-lifetime product of charge carriers in semiconductors [58]. It assumes a constant electric field along the depth of the semiconductor layer, which is insured by the ohmic type of the detector under study. However, its standard form is derived for a weighting potential $\phi(x)$ [171] linear with respect to the sensor depth $(x)$, which is not the case with pixel detectors. Indeed, the so-called small pixel effect [172] predicts that charge carriers induce more charge on their collecting pixel electrode when they travel close to it. For a pixel detector of thickness $d$, whose backside is irradiated with low penetrating particles and biased with a negative voltage V, the Hecht equation becomes [173]:

$$\frac{Q}{Q_0} = \exp(-\frac{d^2}{\mu_e \tau_e V}) + \frac{d}{\mu_e \tau_e V} \int_0^d \phi(x) \exp(-\frac{xd}{\mu_e \tau_e V}) dx \qquad (4.4.1)$$

where $Q$ is the induced charge on the amplifier and $Q_0$ the charge produced by the interaction of the photoelectron in the sensor. The small pixel size, as compared to the sensor thickness, has a significant impact on the weighting potential (see figure 4.4.1 b) and, consequently, on the $\mu_e \tau_e$ product obtained from the fit. Considering square pixel electrodes, we used the weighting potential model developed in [174], with the integral upper bound $N = 10$. We simplified the model by assuming that the charge is created in the pixel center and travels perpendicularly to the electrode surface. The former assumption is supported by the fact that photons interacting close to the border between pixels result in clusters, which were rejected in the analysis (see, for example, figure 7 in [175]).

Applying a negative bias on the backside electrode results in the collection of electrons on the pixel side. Since the average interaction depth is small for 23 keV photons, i.e. an average interaction depth of 13 % the sensor thickness (see figure 4.4.1 b), the contribution of holes and their recombination to the induced charge [176] can be neglected and eq. (4.4.1) is a reasonable approximation. Even though the use of the lowest energy source (8 keV) would have provided a shorter interaction depth (5.6 % the sensor thickness), the induced charge for this source was in the non-linear response region and would have required significantly longer measurements for low biases to obtain sufficient statistics. We thus chose the 23 keV source, with seven different biases from -30 V to -300 V. Finally, it should be noted that even though the induced charge is not directly measured, one only needs a variable proportional

93
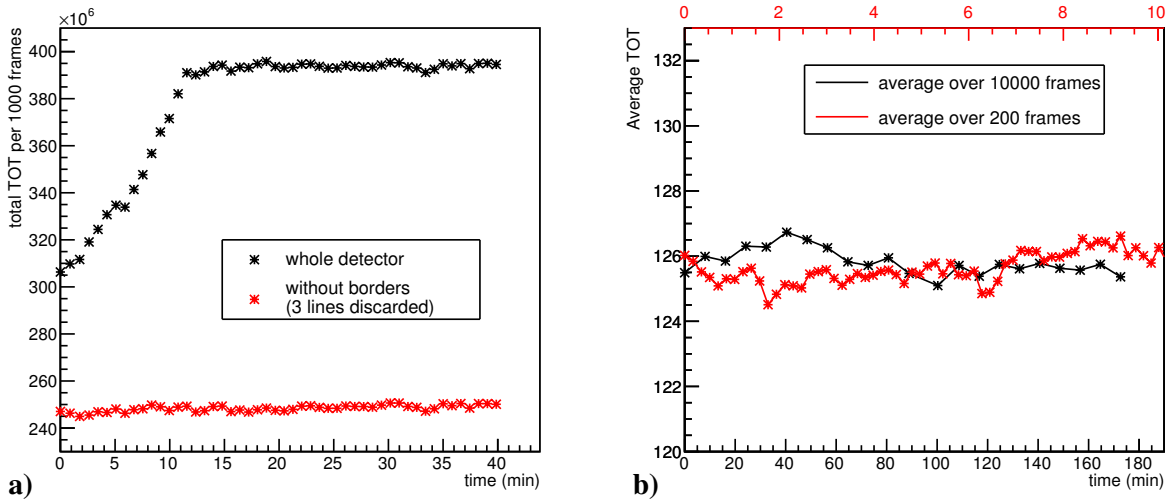
**Fig. 4.4.3.** a) Total TOT (summed over 1000 frames) as a function of time for the 23 keV source with a -300 V bias. The black graph includes all pixels whereas the red graph excludes 3 lines of pixels on each border of the detector. b) Average TOT of single pixel hits as a function of time for the same measurement, illustrated with two different time scales.

to $Q$ in order to fit the data with eq. 4.4.1 and extract the $\mu_e\tau_e$ parameter. As discussed earlier, the measured TOT is not proportional to $Q$ for values close to the detector threshold, and thus the corresponding energy obtained from calibration was used instead.

### 4.4.4. Results and discussion

#### 4.4.4.1. *Time stability*

Compound semiconductor detectors have been shown to suffer from temporal instabilities, such as the polarization effect [172]. Even though these effects are mostly observed for II-VI compounds and higher X-ray fluxes than used for this study, we verified the time stability of the detector in our experimental setup. First, we observed an evolution of noise over time. This is illustrated in figure 4.4.3 a), showing the total TOT summed over 1000 frames for the first 40 mins of the 23 keV measurement with -300 V bias (hits and clusters are considered in this case). The black graph, considering all pixels in the matrix, starts with a continuous increase of total TOT, followed by a stabilization after ~10 mins. The noisy events mostly come from the borders of the matrix, as can be seen by comparison with the

94

red graph, where we excluded 3 lines of pixels on every side of the detector (the outer lines were mostly affected but the 2nd and 3rd also had noticeably more occurrences than in the interior). These events occur when electronic noise or leakage current in the sensor causes the TOT recorded by a pixel to reach its maximum value within a frame, which is limited to $1.2 \cdot 10^4$ clock periods by the digital counter. In the case of the black graph, this is believed to originate from surface currents on the sensor edges [130]. Fitting the red graph with a linear function on the 40 mins range, we obtain a slope of $7.6 \pm 1.2 \cdot 10^4\ TOT\ min^{-1}$, which (dividing by $1.2 \cdot 10^4$ TOT/event) represents an increase of 6 noisy events per minute in the interior of the pixel matrix. These effects are likely due to temperature variations related to the power consumption of the chip, and are not a consequence of polarization.

A parameter indicating the stability of the spectral information more precisely is the average TOT recorded per pixel. It is shown as a function of time in figure 4.4.3 b), for the same data set, excluding border pixels and keeping hits only. In addition, noise and pile up events are rejected by fixing an upper limit on the considered TOT values (TOT < 250). The black graph shows the response for the entire duration of the measurement, and the red graph for the first 10 mins. The Poissonian errors on the average TOT values are in the order of $10^{-3}\%$ for the former and $10^{-2}\%$ for the latter (not visible on the figure). For each time scale we observe trends fluctuating within 2%, which could be explained by instabilities in the analog part of the Timepix chip related to temperature. Even though time stability could be more precisely studied with the faster readouts and chip cited earlier, no trace of polarization could therefore be identified in the present conditions (that is, with 1 ms frames, 50 ms dead time, and detector operated in TOT mode).

### 4.4.4.2. *Photon counting homogeneity*

The detector homogeneity is first analysed in terms of X-ray counting with the 23 keV source and a -300 V bias. The map and distribution of hit counts for the 3 hrs measurement are shown in figure 4.4.4 a) and b), respectively. Inhomogeneities are clearly visible on the map, similar to observations in [134], [177] and [130] for the same material and readout chip, where they are attributed to GaAs defects. Bright areas of pixels surrounded by dark countours correspond to the GaAs dislocation cell structures described in [178], consisting of walls with high dislocation density separated by interiors of dislocation-free material. One
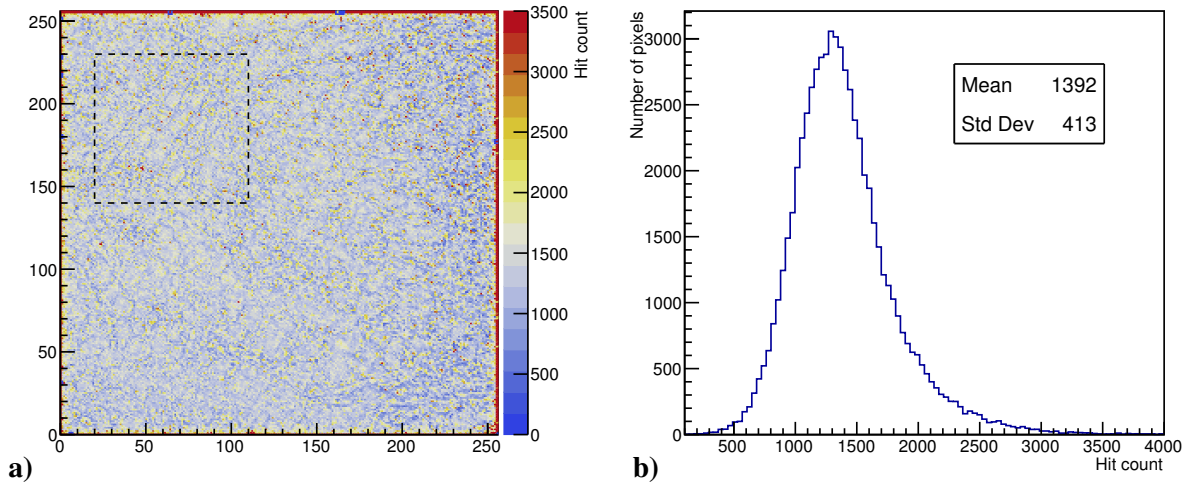
**Fig. 4.4.4.** Map (a) and distribution (b) of hit counts per-pixel for the 23 keV X-ray irradiation at -300 V. The dashed area on the map is enlarged in figure 4.4.5.

can also observe a lower counting (dark blue) region on the right side of the surface, which explains the asymmetry of the distribution.

The gradient of hit counts at the defect boundaries presumably reflects the variation of charge carrier mobility and the distortion of electric field lines [130], which shift the charge carriers path and contribute to the inhomogeneity of charge collection. Even if this can be corrected by a flat-field correction for imaging purposes [179], it is interesting to see how pixel spectra are affected. The dashed area arbitrarily selected on the map is enlarged in figure 4.4.5, with illustration of pixel spectra from three types of regions. A significant difference of statistics is observed between the three selected pixels (a factor 5 between the two extremes).

### 4.4.4.3. *Photon spectroscopy homogeneity*

We now look at the spectral homogeneity of the sensor in more detail, using Gaussian fits on each individual pixel spectrum, as illustrated by red curves in figure 4.4.5. The low energy peak, visible on these spectra, was avoided by limiting the fitting range around the main peak. The map of Gaussian means is shown on figure 4.4.6 a) for the -300 V measurement. Unlike observations with the hit count map, inhomogenities related to material defects cannot be clearly distinguished from statistical fluctuations, except for few strongly affected areas.
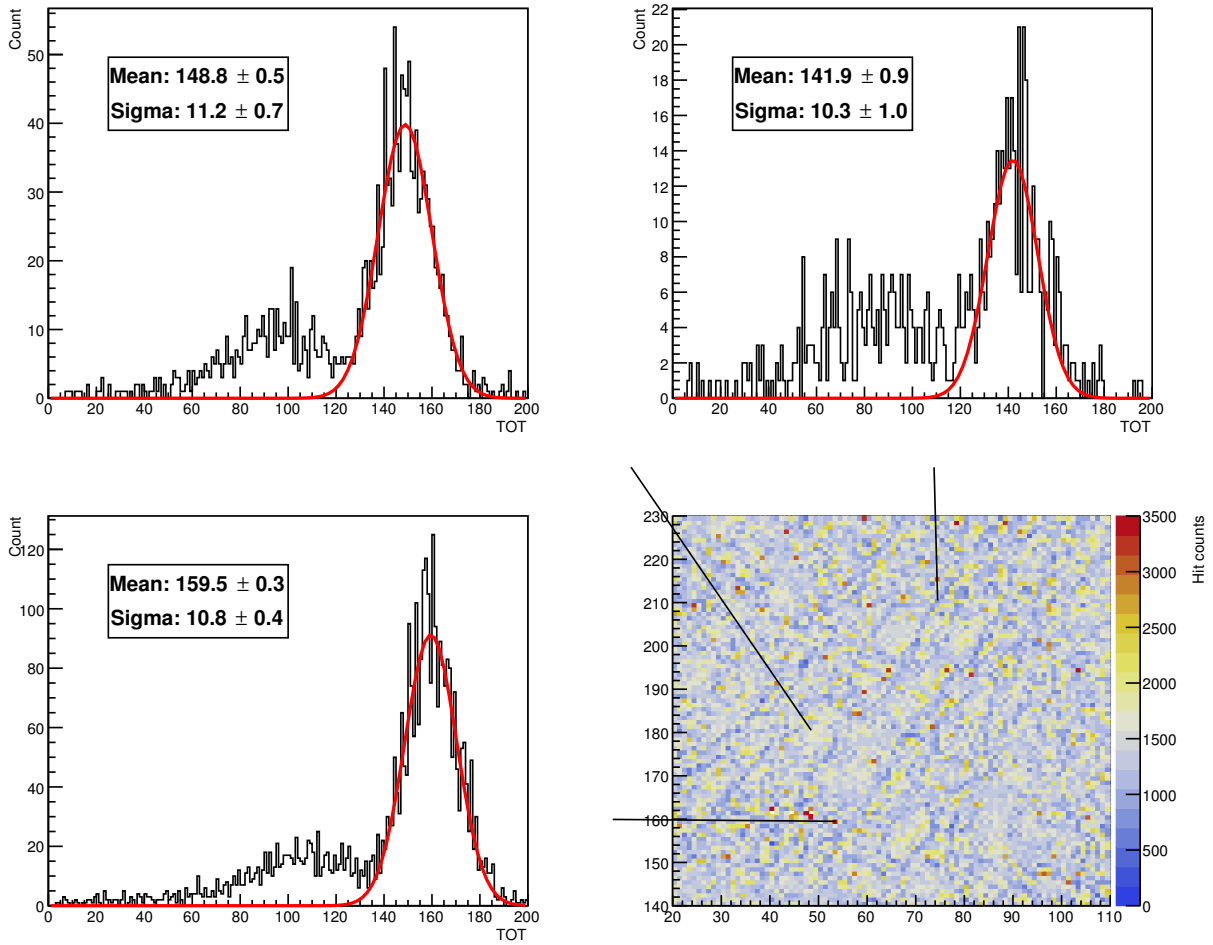
**Fig. 4.4.5.** Zoom on the dashed area of figure 4.4.4 a) with pixel spectra from different regions. Gaussian fits are displayed in red, along with the fit parameters. The detector is operated in TOT mode, which allows the measurement of deposited energy and photon counting at the same time.

This indicates that quasi full charge collection is achieved under this voltage. However, the same plot for the -30 V measurement, in figure 4.4.6 b), reveals a similar structure as observed on the hit count map. The correlation between hit count and Gaussian mean maps is more precisely illustrated on figure 4.4.7 a) for the -300 V and -30 V data sets. Here, the z axis corresponds to the number of pixels with a specific Gaussian mean (x axis) and hit count (y axis). The correlation factor is higher at -30 V (0.42) than at -300 V (0.33), which confirms the visual comparisons of maps. Moreover, we observe for each bias that
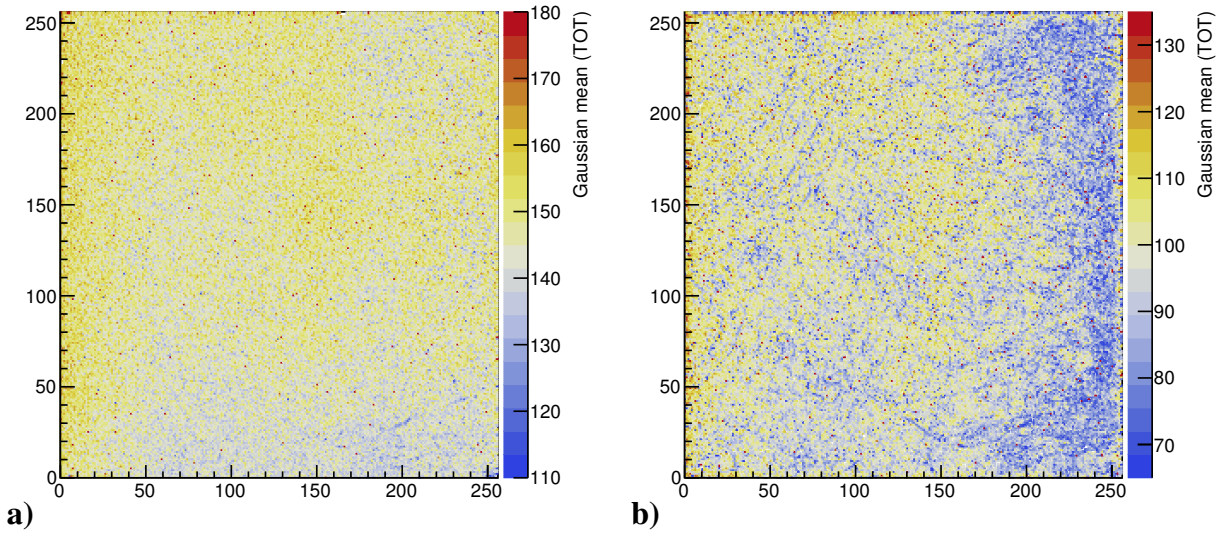
**Fig. 4.4.6.** Map of Gaussian means (in TOT) for the 23 keV irradiation with a bias of -300 V (a) and -30 V (b). Examples of fitted Gaussian functions are illustrated in red in figure 4.4.5 for -300 V.
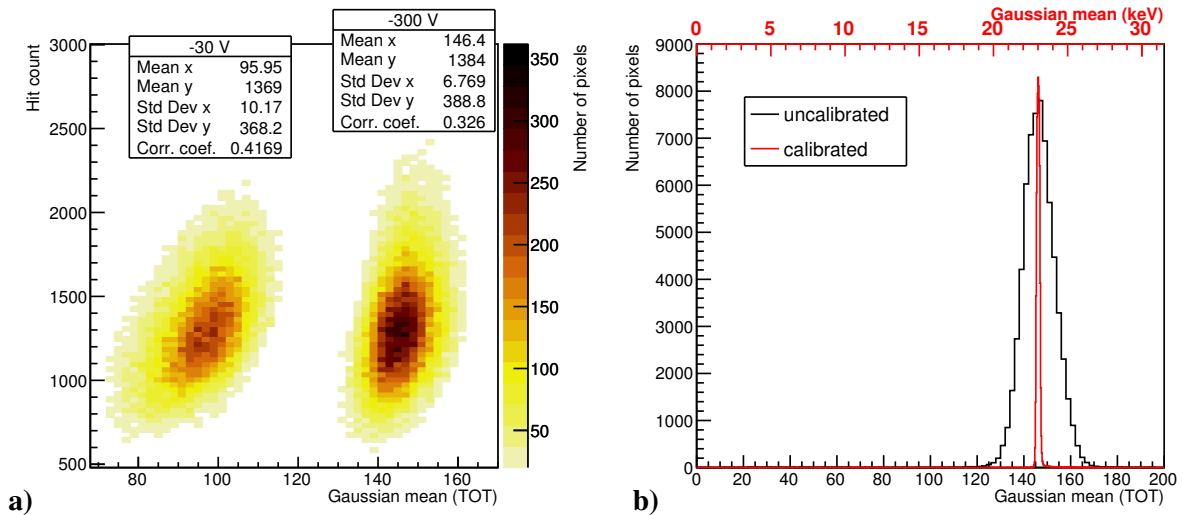
**Fig. 4.4.7.** a) Correlation between the photon count map and the Gaussian mean map for the 23 keV irradiation at -30 V (left) and -300 V (right). Each bin corresponds to the number of pixels with a specific Gaussian mean and photon count. b) Comparison of Gaussian mean distributions with calibrated and uncalibrated data for the 23 keV irradiation at -300 V.

regions with lower mean values correspond to regions with lower counts. Hence, dislocation regions that deviate charge carriers from their corresponding pixel also have smaller charge induction. This can be explained by the presence of traps and/or the combined effects of interaction depth fluctuation and electric field inhomogeneity in the sensor, and will be further discussed in the next subsection.

It is worth mentioning that for a specific bias, the spectral inhomogeneities due to defects would not be observed if the per-pixel calibration was applied, since a reduced charge collection efficiency for a pixel would be compensated by its calibration function. This is why figure 4.4.5, 4.4.6 and 4.4.7 a) are shown in TOT units, i.e. with uncalibrated data[5]. To illustrate this, the variations in per-pixel fitted Gaussian means at -300 V are compared for calibrated and uncalibrated data in figure 4.4.7 b). Fitting these histograms with normal distributions, we obtain a relative spread (FWHM/mean) of 0.9 % with calibration and 10.4 % without. The per-pixel calibration also improves the global energy resolution when all sizes of X-ray clusters are considered, since it corrects for the non-linearity between TOT and deposited energy [175]. An independent study of resolution has been presented in [180] for a GaAs:Cr sensor equipped with a Timepix chip.

### 4.4.4.4. $\mu_e\tau_e$ homogeneity

Finally, we analyse the $\mu_e\tau_e$ products of the sensor, as is commonly done to characterize the quality of high-Z sensors and determine a reasonable range of viable sensor thickness. The corresponding map and distribution obtained with the Hecht model described in section 4.4.3.2 are shown in figure 4.4.8 a) and b), respectively, and three selected fits are illustrated in figure 4.4.9 a). The sensor average $\mu_e\tau_e$ is $1.0 \cdot 10^{-4}$ $cm^2V^{-1}$, which is in agreement with another study [164] investigating the same material using $\alpha$ particles. As a comparison, the average $\mu_e\tau_e$ obtained without taking into account the small pixel effect in our model is $0.45 \cdot 10^{-4}$ $cm^2V^{-1}$, a factor two difference, which is similar to results in [166] with X-rays and the uncorrected Hecht model.

Interestingly, the map shows a defect structure similar to the one observed with hit counts. As can be seen by comparison of figure 4.4.9 b) and figure 4.4.5, regions with lower $\mu_e\tau_e$ match regions with lower count rates. This is confirmed by the histogram in figure 4.4.10,

---

[5]The determination of $\mu_e\tau_e$ products presented in the next subsection, however, does require calibrated data, as explained in section 4.4.3.2.
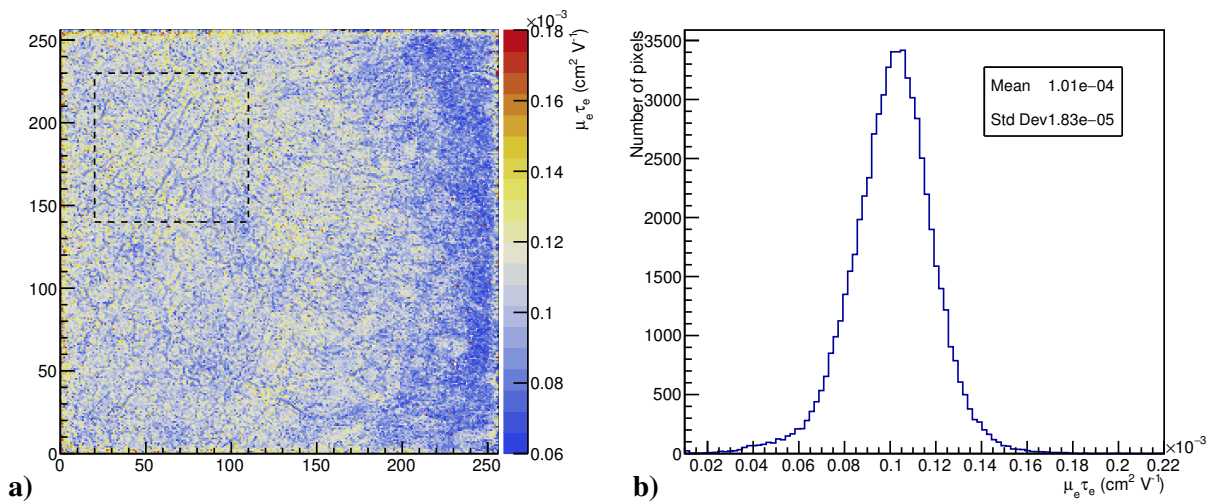
**Fig. 4.4.8.** $\mu_e\tau_e$ map (a) and distribution (b) obtained from the 23 keV source. The dashed area on a) is enlarged in figure 4.4.9 a).

correlating the hit count map at -300 V and the $\mu_e\tau_e$ map. Here, the z axis corresponds to the number of pixels with a specific $\mu_e\tau_e$ and hit count. Following the displayed trend line, a 1% increase of $\mu_e\tau_e$ leads to a 1 % increase of hit counts from the means values. Defect structures trapping charge carriers and simultaneously bending the electric field in their vicinity are a possible interpretation of these observations. As seen in figure 4.4.9 a), these regions reach full charge collection slower than others as the bias increases, and it is therefore important to bias the detector sufficiently to reduce inhomogeneities in the induced charge.

### 4.4.5. Conclusion

The GaAs:Cr pixel detector characterized in this study has the capability of photon counting and spectroscopy with good time stability for X-ray fluxes of the order of $10^5 \ cm^{-2}s^{-1}$. Its $\mu_e\tau_e$ product was extracted on a per-pixel basis with a precise Hecht model, and was found to follow the same inhomogeneities as the hit counting response due to material defects. Considering the involved electric field ($E$), the regions with lowest $\mu_e\tau_e$ values corresponded to a mean electron drift length ($\mu_e\tau_e \cdot E$) in the order of 1 mm.

The response inhomogeneity can be corrected to a certain extent, for example with the per-pixel calibration in spectroscopy or a flat-field correction in imaging with known energy spectra [138]. However, the 3D distribution of defects in the GaAs volume will deteriorate
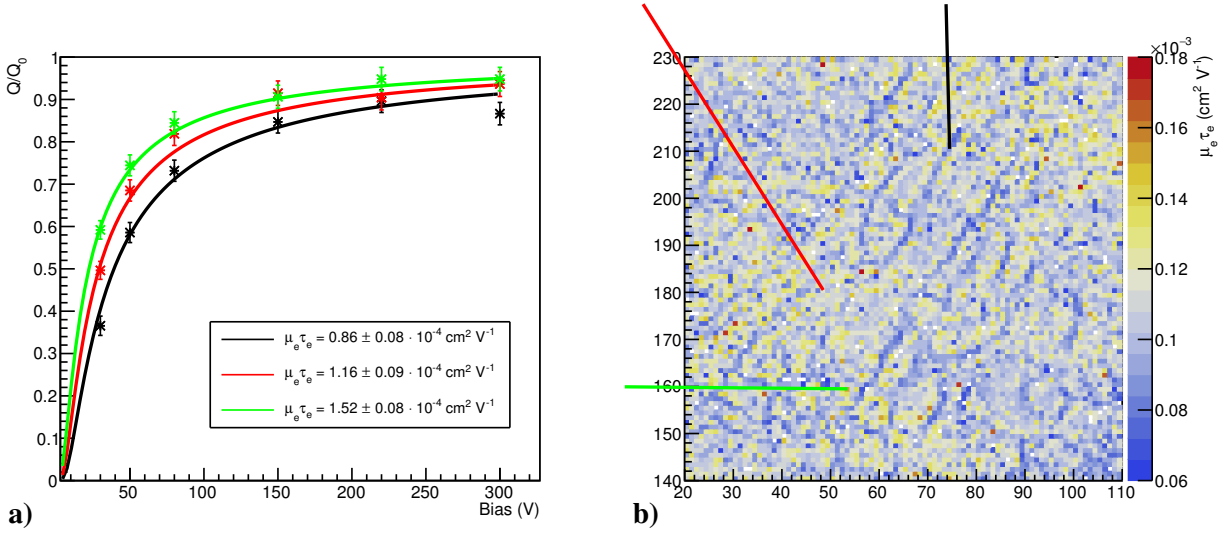
**Fig. 4.4.9.** a) Hecht graphs and fit functions for the same pixels as figure 4.4.5. For each point, the error bar was calculated from the statistical errors on the TOT Gaussian mean and calibration coefficients. b) Zoom on the dashed area of figure 4.4.8 (same area as figure 4.4.5). The arrow colors refer to the graphs on the left.
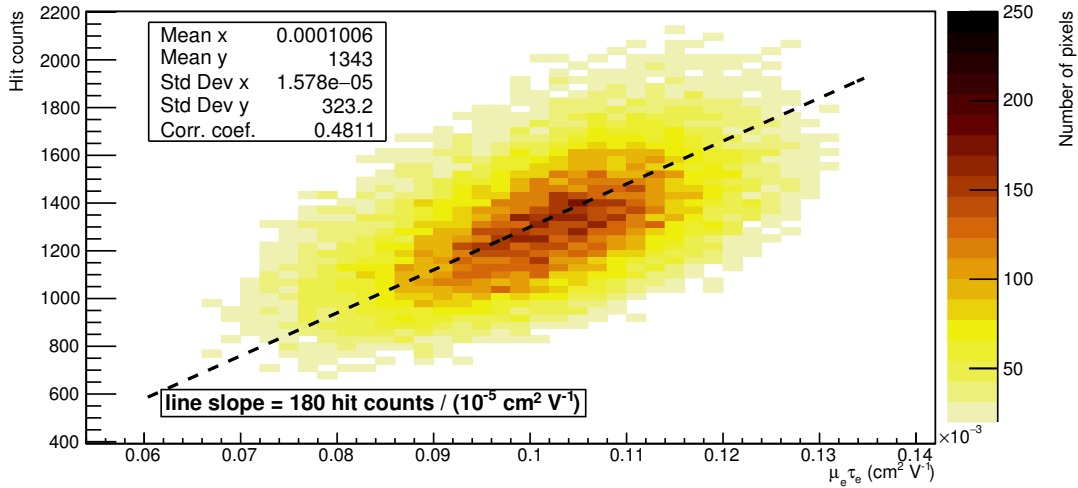
**Fig. 4.4.10.** Correlation between the photon count map at -300 V and the $\mu_e\tau_e$ map for the 23 keV irradiation. Each bin corresponds to the number of pixels with a specific $\mu_e\tau_e$ and photon count.

101

the detector response in situations involving mixed radiation fields (consisting not only of photons but also neutrons and energetic charged particles) or X-ray imaging with unknown spectra, since the localization of charge carriers in the sensor depends on the type of interacting radiation quantum and its energy. Additionally, the inhomogeneity of hit count rates decreases the dynamic range of the detector in imaging (when using the detector in counting mode), since some counters are filled over-proportionally fast, whereas others remain empty. This results in the need for multiple shorter exposures or to discard some areas completely, having a counter of limited depth. Dedicated studies should be made for specific applications and are planned for the future. Nevertheless, this detector seems promising for applications in which its higher atomic number is an advantage over silicon.

### 4.4.6. acknowledgments

publication

## 4.5. Summary and Beyond

The above investigations demonstrated that CdTe and GaAs:Cr TPX detectors can be operated reasonably well at room temperature, and in vacuum using a thermal sink. They proved to be stable over several hours of measurement, even though noisy pixels must be looked out for and eliminated. This is to be particularly considered with the current plan to use TPX3 chips operated in *data driven* mode for ATLAS-TPX upgrades since, with TPX3, noisy pixels can drastically increase the data rate, resulting in possible crashes of the controlling software and producing over-sized data files. Further, it was found that the sensors possess acceptable levels of inhomogeneities, which can be corrected to some extent by the per-pixel energy calibration. With regard to installation in ATLAS, CdTe and GaAs:Cr TPX detectors should be compared with silicon TPX detectors in terms of other particle tracking capabilities, such as dE/dx, incident angle or neutron measurements. The radiation hardness of CdTe and GaAs:Cr sensors should also be assessed, and compared to the radiation hardness of the TPX and TPX3 chips. In conclusion, advances in the production of CdTe and GaAs crystals make these sensors suitable for upgrades of the ATLAS-TPX network, in particular if accurate analysis of the photon field or higher stopping power of single detectors are of concern. Also the combination of semiconductor detector featuring different sensor material gives additional means of particle analysis. For example, identifying two coincident tracks in an hodoscope detector with one Si sensor and one high-Z sensor, and comparing both dE/dx measured, could help distinguishing between different heavy charged particles. In addition, the high electron mobility of GaAs could be exploited if faster signal is required to keep track of bunch-by-bunch interactions in LHC.

The sensor materials discussed in this work are subject to ongoing investigations. In particular, GaAs:Cr TPX detectors have been installed in ATLAS soon after the investigations of the paper [181], and preliminary results are expected soon. Moreover, as discussed earlier, TPX3 chips can be used to develop Compton cameras, which could help characterizing the photon field in ATLAS. The concept of such devices is to localize gamma ray sources using two energy-sensitive pixel detectors in an hodoscope structure, as presently done with ATLAS-TPX. The photon trajectory is scattered in the first sensor by Compton interaction, and absorbed in the second by photoelectric effect (see Ref. [70], for example). To increase
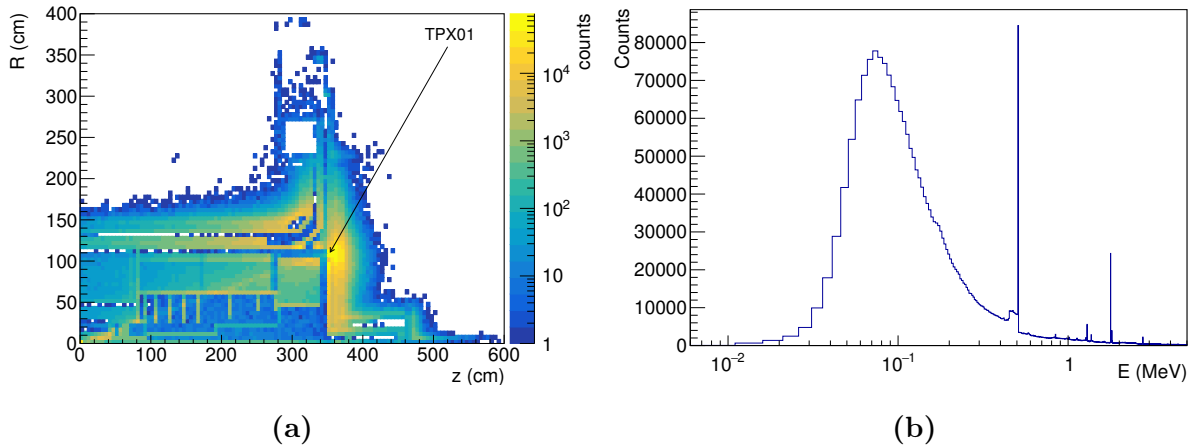
**Fig. 4.5.1.** Birth position of photons hitting the location of TPX01 in ATLAS (a) and their spectra (b), as obtained from simulations [**97**]. See table 3.3.1 for the detector location in ATLAS. See figure 3.4.1 and 3.2.2 for comparisons with charged particles and neutrons.

the probability of absorption, the second layer ideally features a high-Z sensor. With sufficient statistics, the recorded scattering angles then allow reconstructing the origin of the gamma source. First prototypes using TPX3 chips have been tested recently [**182**], and progress in this direction can be expected to be fast due to the potential of these devices in a wide range of applications. However, current investigations address the simplest possible case of point-like mono-energetic sources, which is far from the complex radiation environment in ATLAS (see figure 4.5.1). Hence, the applicability of such devices to ATLAS-TPX upgrades will require dedicated investigations.

# Conclusion and Outlook

The present thesis was written in the context of the ATLAS-TPX project, a pixel detector network to characterize the radiation field in ATLAS using a novel readout ASIC technology. An analysis of the data recorded by the ATLAS-TPX detectors during LHC Run-2 was presented. Here, the main development was the establishment of algorithms to extract properties of energetic charged particles, namely their direction and energy loss, at any location where the detectors are installed. The developed analysis methods were applied to measured data, and results were reported. Moreover, thermal neutron fluences were measured, analyzed and reported, while the fast neutron component proved to be not completely resolved, pending further investigation. The results allow the identification of radiation sources which cause induced radioactivity, background signals and radiation damage to the multiple detectors forming ATLAS. They can be used to benchmark simulations of the radiation environment in ATLAS, in a different way than usually done with other radiation monitors, i.e., on a track by track basis. The developed methods can be used for the future upgrade of ATLAS-TPX, which is currently being discussed at UdeM and IEAP. In particular, they can be adapted to the new generation of Timepix detectors, Timepix3, which will be the readout ASICs used in the upgrade for improving time resolution, track coincidence identification and data acquisition time. As a general matter, detection techniques developed and tested with ATLAS-TPX in the complex radiation field of ATLAS could be used in any other experiment where mixed radiation fields need to be investigated.

In conjunction with this, Timepix detectors with GaAs and CdTe sensors were characterized, considering the possible integration of these sensors in future ATLAS-TPX upgrades. The focus was put on their charge collection efficiency, homogeneity and time-stability, revealing an acceptable level of trapping centers and noise. Their electron mobility-lifetime

products were extracted and were found to be consistent with values available in the literature. Moreover, the detectors showed to be quite stable over extended periods of time under alpha or X-ray irradiation. Hence, the recent developments in the growth processes of these compound semiconductors make them suitable for use in applications such as radiation monitoring in ATLAS. With this information in mind, the next step will be to assess their tracking performance in more realistic conditions, for example with energetic charged particles and neutrons of different energy ranges. When bump-bonded to these high-Z sensors, Timepix3 chips could improve the photon field characterization, and even allow the localization of gamma sources using the Compton effect. This would improve our knowledge of the background signal, radiation damage sources and induced radioactivity in ATLAS. Such investigations have already started, and will continue to be performed during the current LHC shutdown (2019-2020) with regard to ATLAS-TPX upgrades.

# Bibliography

[1] A. Sopczak, B. Ali, T. Asawatavonvanich *et al.*, "Precision Luminosity of LHC Proton–Proton Collisions at 13 TeV Using Hit Counting With TPX Pixel Devices," *IEEE Transactions on Nuclear Science*, vol. 64, no. 3, pp. 915–924, March 2017.

[2] R. Brun and F. Rademakers, "ROOT — An object oriented data analysis framework," *Nucl. Instr. Meth. Phys. Res. A*, vol. 389, no. 1, pp. 81 – 86, 1997, new Computing Techniques in Physics Research V. [Online]. Available: http://www.sciencedirect.com/science/article/pii/S016890029700048X

[3] S. Agostinelli, J. Allison, K. Amako *et al.*, "Geant4—a simulation toolkit," *Nucl. Instrum. Methods Phys. Res. A, Accel. Spectrom. Detect. Assoc. Equip.*, vol. 506, no. 3, pp. 250 – 303, 2003, doi: 10.1016/S0168-9002(03)01368-8.

[4] S. Spannagel, K. Wolters, D. Hynds *et al.*, "Allpix2: A modular simulation framework for silicon detectors," *Nucl. Instrum. Methods Phys. Res. A, Accel. Spectrom. Detect. Assoc. Equip.*, vol. 901, pp. 164 – 172, 2018, doi: 10.1016/j.nima.2018.06.020.

[5] "MAFalda framework," accessed: Apr. 30th 2019. [Online]. Available: https://github.com/idarraga/mafalda

[6] "Allpix2: Generic Pixel Detector Simulation Framework," accessed: Apr. 30th 2019. [Online]. Available: https://gitlab.cern.ch/allpix-squared/allpix-squared/

[7] "ATpx framework," accessed: May 6th 2019. [Online]. Available: https://gitlab.cern.ch/tbilloud/

[8] A. Ferrari, P. R. Sala, A. Fassò *et al.*, "Can we predict radiation levels in calorimeters?" CERN, Geneva, Tech. Rep. ATL-CAL-91-005, ATL-AC-PN-5, Nov 1991. [Online]. Available: http://cds.cern.ch/record/685617

[9] The ATLAS Collaboration, "ATLAS: Letter of intent for a general purpose p p experiment at the large hadron collider at CERN," CERN, Tech. Rep. CERN-LHCC-92-04, CERN-LHCC-I-2, 1992.

[10] The ATLAS Collaboration, "ATLAS: Detector and physics performance technical design report. Volume 1," CERN, Tech. Rep. CERN-LHCC-99-14, ATLAS-TDR-14, 1999.

[11] The ATLAS Collaboration, "The ATLAS Experiment at the CERN Large Hadron Collider," *J. Instrum.*, vol. 3, no. 08, pp. S08 003–S08 003, Aug. 2008, doi: 10.1088/1748-0221/3/08/s08003.

[12] C. Leroy, S. Pospisil, M. Suk *et al.*, "Proposal to Measure Radiation Field Characteristics, Luminosity and Induced Radioactivity in ATLAS with Timepix Devices," CERN, Geneva, Switzerland, Tech. Rep. ATLAS-COM-GEN-2014-005, 2014. [Online]. Available: https://cds.cern.ch/record/1646970/

[13] M. Campbell, E. Heijne, C. Leroy *et al.*, "Analysis of the Radiation Field in ATLAS Using 2008-2011 Data from the ATLAS-MPX Network," CERN, Geneva, Tech. Rep. ATL-GEN-PUB-2013-001, Apr. 2013. [Online]. Available: https://cds.cern.ch/record/1544435

[14] R. Alemany-Fernandez, E. Bravin, L. Drosdal *et al.*, "Operation and Configuration of the LHC in Run 1," CERN, Tech. Rep. CERN-ACC-NOTE-2013-0041, Nov 2013. [Online]. Available: https://cds.cern.ch/record/1631030

[15] J. Wenninger, "Operation and Configuration of the LHC in Run 2," CERN, Tech. Rep. CERN-ACC-NOTE-2019-0007, Mar 2019. [Online]. Available: https://cds.cern.ch/record/2668326

[16] B. Bergmann, I. Caicedo, C. Leroy *et al.*, "ATLAS-TPX: a two-layer pixel detector setup for neutron detection and radiation field characterization," *J. Instrum.*, vol. 11, no. 10, p. P10002, Oct. 2016, doi: 10.1088/1748-0221/11/10/P10002.

[17] R. Jayakumar, *Particle Accelerators, Colliders, and the Story of High Energy Physics.* Springer-Verlag Berlin Heidelberg, 2012.

[18] M. Tanabashi, K. Hagiwara, K. Hikasa *et al.*, "Review of particle physics," *Phys. Rev. D*, vol. 98, p. 030001, Aug 2018. [Online]. Available: https://link.aps.org/doi/10.1103/PhysRevD.98.030001

[19] S. Abachi, B. Abbott, M. Abolins *et al.*, "Observation of the top quark," *Phys. Rev. Lett.*, vol. 74, pp. 2632–2637, Apr 1995. [Online]. Available: https://link.aps.org/doi/10.1103/PhysRevLett.74.2632

[20] K. Kodama, N. Ushida, C. Andreopoulos *et al.*, "Observation of tau neutrino interactions," *Physics Letters B*, vol. 504, no. 3, pp. 218 – 224, 2001. [Online]. Available: http://www.sciencedirect.com/science/article/pii/S0370269301003070

[21] (2019, Mar.). [Online]. Available: https://home.cern/about

[22] G. Aad, T. Abajyan, B. Abbott *et al.*, "Observation of a new particle in the search for the Standard Model Higgs boson with the ATLAS detector at the LHC," *Physics Letters B*, vol. 716, no. 1, pp. 1 – 29, 2012. [Online]. Available: http://www.sciencedirect.com/science/article/pii/S037026931200857X

[23] S. Chatrchyan, V. Khachatryan, A. Sirunyan *et al.*, "Observation of a new boson at a mass of 125 GeV with the CMS experiment at the LHC," *Physics Letters B*, vol. 716, no. 1, pp. 30 – 61, 2012. [Online]. Available: http://www.sciencedirect.com/science/article/pii/S0370269312008581

[24] R. N. Cahn, "The eighteen arbitrary parameters of the standard model in your everyday life," *Rev. Mod. Phys.*, vol. 68, pp. 951–959, Jul 1996. [Online]. Available: https://link.aps.org/doi/10.1103/RevModPhys.68.951

[25] U. Baur, I. Hinchliffe, and D. Zeppenfeld, "Excited quark production at hadron colliders," *International Journal of Modern Physics A*, vol. 02, no. 04, pp. 1285–1297, 1987. [Online]. Available: https://doi.org/10.1142/S0217751X87000661

[26] L. Lederman, "The God particle et al." *Nature*, vol. 448, pp. 310 EP –, 07 2007. [Online]. Available: https://doi.org/10.1038/nature06081

[27] K. Iordanidou, "First ATLAS Search Results With 140 fb-1," in *CERN seminar*, Mar. 2019.

[28] (2019, Mar.). [Online]. Available: http://timeline-fr.web.cern.ch/timelines/The-ATLAS-experiment/overlay#2010-03-30%2008:45:00

[29] G. Apollinari, I. Béjar Alonso, O. Brüning *et al.*, "High-Luminosity Large Hadron Collider (HL-LHC): Technical Design Report V. 0.1," CERN, Tech. Rep. CERN-2017-007-M, 2017. [Online]. Available: https://cds.cern.ch/record/2284929

[30] (2019, Mar.). [Online]. Available: https://home.cern/news/press-release/accelerators/lhc-prepares-new-achievements

[31] A. Baldini, D. Glenzinski, F. Kapusta *et al.*, "Charged lepton flavour violation using intense muon beams at future facilities (a submission to the 2020 update of the european strategy for particle physics)," COMET, MEG, Mu2e and Mu3e collaborations., Tech. Rep. arXiv:1812.06540, 2019.

[32] M. Benedikt, A. Blondel, O. Brunner *et al.*, "Future Circular Collider," CERN, Geneva, Tech. Rep. CERN-ACC-2018-0057, Dec 2018, submitted for publication to Eur. Phys. J. ST. [Online]. Available: http://cds.cern.ch/record/2651299

[33] V. Shiltsev, "A phenomenological cost model for high energy particle accelerators," *JINST*, vol. 9, 04 2014.

[34] O. S. Brüning, P. Collier, P. Lebrun *et al.*, *LHC Design Report*, ser. CERN Yellow Reports: Monographs. Geneva: CERN, 2004. [Online]. Available: http://cds.cern.ch/record/782076

[35] The ATLAS Collaboration, "Measurement of the Inelastic Proton-Proton Cross Section at $\sqrt{s} = 13$ TeV with the ATLAS Detector at the LHC," CERN, Geneva, Tech. Rep. ATLAS-CONF-2015-038, Aug 2015. [Online]. Available: http://cds.cern.ch/record/2045064

[36] (2019, Mar.). [Online]. Available: https://twiki.cern.ch/twiki/bin/view/AtlasPublic/LuminosityPublicResultsRun2

[37] D. Froidevaux and P. Sphicas, "General-purpose detectors for the Large Hadron Collider," *Ann. Rev. Nucl. Part. Sci.*, vol. 56, pp. 375–440, 2006.

[38] M. Bruschi, "The New ATLAS/LUCID detector," CERN, Tech. Rep. ATL-FWD-PROC-2015-002, 2015.

[39] S. Abdel Khalek *et al.*, "The ALFA Roman Pot Detectors of ATLAS," *JINST*, vol. 11, no. 11, p. P11013, 2016.

[40] The ATLAS Collaboration, "Technical Design Report for the ATLAS Forward Proton Detector," CERN, Tech. Rep. CERN-LHCC-2015-009, ATLAS-TDR-024, May 2015. [Online]. Available: https://cds.cern.ch/record/2017378

[41] S. White, "The ATLAS zero degree calorimeter," *Nuclear Instruments and Methods in Physics Research Section A: Accelerators, Spectrometers, Detectors and Associated Equipment*, vol. 617,

no. 1, pp. 126 – 128, 2010, 11th Pisa Meeting on Advanced Detectors. [Online]. Available: http://www.sciencedirect.com/science/article/pii/S0168900209019044

[42] S. Baranov, M. Bosman, I. Dawson *et al.*, "Estimation of Radiation Background, Impact on Detectors, Activation and Shielding Optimization in ATLAS," CERN, Geneva, Switzerland, Tech. Rep. ATL-GEN-2005-001, ATL-COM-GEN-2005-001, CERN-ATL-GEN-2005-001, 2005. [Online]. Available: http://cdsweb.cern.ch/record/814823/files/gen-2005-001.pdf

[43] B. T. Knudsen, "Presentation of the WA97 experiment at CERN," *Czechoslovak Journal of Physics*, vol. 47, no. 9, pp. 925–929, Sep 1997. [Online]. Available: https://doi.org/10.1023/A:1021200315694

[44] (2019, Mar.). [Online]. Available: https://medipix.web.cern.ch/

[45] M. Campbell, "10 years of the Medipix2 Collaboration," *Nuclear Instruments and Methods in Physics Research Section A: Accelerators, Spectrometers, Detectors and Associated Equipment*, vol. 633, 05 2011.

[46] L. Rossi, P. Fischer, T. Rohe *et al.*, "Pixel detectors," *Pixel Detectors: From Fundamentals to Applications, Particle Acceleration and Detection. ISBN 978-3-540-28332-4. Springer-Verlag Berlin Heidelberg, 2006*, 01 2006.

[47] A. Owens and A. Peacock, "Compound semiconductor radiation detectors," *Nucl. Instr. Meth. Phys. Res. A*, vol. 531, no. 1–2, pp. 18 – 37, 2004, proceedings of the 5th International Workshop on Radiation Imaging Detectors. [Online]. Available: http://www.sciencedirect.com/science/article/pii/S0168900204010575

[48] H. Spieler, *Semiconductor Detector Systems*, ser. Semiconductor Science and Technology. Oxford: Oxford University Press, 2005, vol. v.12. [Online]. Available: http://www.oup.co.uk/isbn/0-19-852784-5

[49] A. A. Quaranta, A. Taroni, and G. Zanarini, "Plasma time and related delay effects in solid state detectors," *Nuclear Instruments and Methods*, vol. 72, no. 1, pp. 72 – 76, 1969. [Online]. Available: http://www.sciencedirect.com/science/article/pii/0029554X69902675

[50] J. Bouchami, A. Gutierrez, A. Houdayer *et al.*, "Study of the charge sharing in silicon pixel detector with heavy ionizing particles interacting with a medipix2 and a timepix devices," in *2008 IEEE Nuclear Science Symposium Conference Record*, Oct 2008, pp. 1358–1360.

[51] K. Mathieson, M. Passmore, P. Seller *et al.*, "Charge sharing in silicon pixel detectors," *Nuclear Instruments and Methods in Physics Research Section A: Accelerators, Spectrometers, Detectors and Associated Equipment*, vol. 487, no. 1, pp. 113 – 122, 2002, 3rd International Workshop on Radiation Imaging Detectors. [Online]. Available: http://www.sciencedirect.com/science/article/pii/S0168900202009543

[52] J. Bouchami, A. Gutiérrez, A. Houdayer *et al.*, "Study of the charge sharing in silicon pixel detector by means of heavy ionizing particles interacting with a Medipix2 device," *Nucl. Instr. Meth. Phys. Res. A*, vol. 633, Supplement 1, pp. S117 – S120, 2011,

11th International Workshop on Radiation Imaging Detectors (IWORID). [Online]. Available: http://www.sciencedirect.com/science/article/pii/S0168900210013318

[53] A. Owens, *Compound Semiconductor Radiation Detectors*, ser. Series in Sensors. Taylor & Francis Group, 2016. [Online]. Available: https://books.google.fi/books?id=bMpEvgAACAAJ

[54] S. Ramo, "Currents induced by electron motion," *Proc. Ire.*, vol. 27, pp. 584 – 585, 1939.

[55] L.-A. Hamel and M. Julien, "Generalized demonstration of ramo's theorem with space charge and polarization effects," *Nuclear Instruments and Methods in Physics Research Section A: Accelerators, Spectrometers, Detectors and Associated Equipment*, vol. 597, no. 2, pp. 207 – 211, 2008. [Online]. Available: http://www.sciencedirect.com/science/article/pii/S0168900208014393

[56] W. Riegler and G. A. Rinella, "Point charge potential and weighting field of a pixel or pad in a plane condenser," *Nucl. Instr. Meth. Phys. Res. A*, vol. 767, pp. 267 – 270, 2014. [Online]. Available: http://www.sciencedirect.com/science/article/pii/S0168900214009796

[57] G. F. Knoll, *Radiation detection and measurement; 4th ed.* New York, NY: Wiley, 2010. [Online]. Available: https://cds.cern.ch/record/1300754

[58] K. Hecht, "Zum Mechanismus des lichtelektrischen Primärstromes in isolierenden Kristallen," *Zeitschrift fur Physik*, vol. 77, p. 235, 1932.

[59] (2019, Mar.). [Online]. Available: https://en.wikipedia.org/wiki/Medipix

[60] J. Bouchami, A. Gutiérrez, T. Holy *et al.*, "Measurement of pattern recognition efficiency of tracks generated by ionizing radiation in a Medipix2 device," *Nucl. Instrum. Methods Phys. Res. A, Accel. Spectrom. Detect. Assoc. Equip.*, vol. 633, pp. S187 – S189, 2011, doi: 10.1016/j.nima.2010.06.163.

[61] J. Jakůbek, "Semiconductor Pixel detectors and their applications in life sciences," *Journal of Instrumentation*, vol. 4, no. 03, pp. P03 013–P03 013, mar 2009. [Online]. Available: https://doi.org/10.1088%2F1748-0221%2F4%2F03%2Fp03013

[62] X. Llopart, R. Ballabriga, M. Campbell *et al.*, "Timepix, a 65k programmable pixel readout chip for arrival time, energy and/or photon counting measurements," *Nucl. Instr. Meth. Phys. Res. A*, vol. 581, no. 1–2, pp. 485 – 494, 2007, {VCI} 2007Proceedings of the 11th International Vienna Conference on Instrumentation. [Online]. Available: http://www.sciencedirect.com/science/article/pii/S0168900207017020

[63] J. Jakubek, A. Cejnarova, T. Holy *et al.*, "Pixel detectors for imaging with heavy charged particles," *Nucl. Instr. Meth. Phys. Res. A*, vol. 591, no. 1, pp. 155 – 158, 2008. [Online]. Available: http://www.sciencedirect.com/science/article/pii/S0168900208004245

[64] J. Jakubek, "Precise energy calibration of pixel detector working in time-over-threshold mode," *Nucl. Instr. Meth. Phys. Res. A*, vol. 633, Supplement 1, pp. S262 – S266, 2011. [Online]. Available: http://www.sciencedirect.com/science/article/pii/S0168900210013732

[65] N. Asbah, C. Leroy, S. Pospisil *et al.*, "Measurement of the efficiency of the pattern recognition of tracks generated by ionizing radiation in a Timepix detector," *J. Instrum.*, vol. 9, no. 05, p. C05021, 2014.

[66] C. Leroy, N. Asbah, L.-G. Gagnon *et al.*, "Timepix device efficiency for pattern recognition of tracks generated by ionizing radiation," in *Proceedings of the 14th ICATPP Conference, Villa Olmo, Como, Italy*, S. Giani et al., World Scientific Publishing, Co. Pte. Ltd., Singapore, Ed., Aug. 2014, pp. 494–506.

[67] M. Campbell, J. Alozy, R. Ballabriga *et al.*, "Towards a new generation of pixel detector readout chips," *J. Instrum.*, vol. 11, no. 01, p. C01007, 2016. [Online]. Available: http://stacks.iop.org/1748-0221/11/i=01/a=C01007

[68] T. Poikela, J. Plosila, T. Westerlund *et al.*, "Timepix3: a 65K channel hybrid pixel readout chip with simultaneous ToA/ToT and sparse readout," *J. Instrum.*, vol. 9, no. 05, p. C05013, 2014. [Online]. Available: http://stacks.iop.org/1748-0221/9/i=05/a=C05013

[69] B. Bergmann, M. Pichotka, S. Pospisil *et al.*, "3d track reconstruction capability of a silicon hybrid active pixel detector," *The Eur. Physical J. C*, vol. 77, no. 6, p. 421, Jun. 2017, doi: 10.1140/epjc/s10052-017-4993-4.

[70] C. Leroy and P.-G. Rancoita, *Principles of radiation interaction in matter and detection*, 4th ed. Singapore: World Scientific, 2016. [Online]. Available: https://www.worldscientific.com/doi/abs/10.1142/9167

[71] W. R. Leo, *Techniques for nuclear and particle physics experiments: a how-to approach; 2nd ed.* Berlin: Springer, 1994. [Online]. Available: https://cds.cern.ch/record/302344

[72] M. Platkevic, P. Cermak, J. Jakubek *et al.*, "Characterization of charge collection in various semiconductor sensors with energetic protons and timepix device," in *2011 IEEE Nuclear Science Symposium Conference Record*, Oct 2011, pp. 4715–4719.

[73] M. Esposito, J. Jakubek, G. Mettivier *et al.*, "Energy sensitive Timepix silicon detector for electron imaging," *Nuclear Instruments and Methods in Physics Research Section A: Accelerators, Spectrometers, Detectors and Associated Equipment*, vol. 652, no. 1, pp. 458 – 461, 2011, symposium on Radiation Measurements and Applications (SORMA) XII 2010. [Online]. Available: http://www.sciencedirect.com/science/article/pii/S0168900211002506

[74] M. J. Berger, J. H. Hubbell, S. M. Seltzer *et al.*, "XCOM: Photon Cross Sections Database," *NIST Standard Reference Database 8 (XGAM)*, 2010.

[75] M. Hodgson, A. Lohstroh, P. Sellin *et al.*, "Neutron detection performance of silicon carbide and diamond detectors with incomplete charge collection properties," *Nuclear Instruments and Methods in Physics Research Section A: Accelerators, Spectrometers, Detectors and Associated Equipment*, vol. 847, pp. 1–9, 11 2016.

[76] M. M. Pickrell, A. Lavietes, V. Gavron *et al.*, "The IAEA Workshop on Requirements and Potential Technologies for Replacement of 3He Detectors in IAEA Safeguards Applications," *JNMM, Journal of the Institute of Nuclear Materials Management*, vol. 41, pp. 14–29, 03 2013.

[77] J. Jakubek, T. Holy, E. Lehmann *et al.*, "Spatial resolution of Medipix-2 device as neutron pixel detector," *Nuclear Instruments and Methods in Physics Research Section A: Accelerators, Spectrometers, Detectors and Associated Equipment*, vol. 546, no. 1, pp. 164 – 169, 2005, proceedings of the 6th International Workshop on Radiation Imaging Detectors. [Online]. Available: http://www.sciencedirect.com/science/article/pii/S0168900205006248

[78] M. Campbell, V. Havranek, E. Heijne *et al.*, "Charge collection from proton and alpha particle tracks in silicon pixel detector devices," in *2007 IEEE Nucl. Sci. Symp. Conf. Rec.*, vol. 2, Oct. 2007, pp. 1047–1050, doi: 10.1109/NSSMIC.2007.4437190.

[79] S. Gohl, B. Bergmann, H. Evans *et al.*, "Study of the radiation fields in LEO with the Space Application of Timepix Radiation Monitor (SATRAM)," *Advances in Space Res.*, 2018, doi: 10.1016/j.asr.2018.11.016.

[80] K. Akiba, M. Artuso, R. Badman *et al.*, "Charged particle tracking with the timepix asic," *Nuclear Instruments and Methods in Physics Research Section A: Accelerators, Spectrometers, Detectors and Associated Equipment*, vol. 661, no. 1, pp. 31 – 49, 2012. [Online]. Available: http://www.sciencedirect.com/science/article/pii/S0168900211017736

[81] K. Akiba, P. Ronning, M. van Beuzekom *et al.*, "The timepix telescope for high performance particle tracking," *Nuclear Instruments and Methods in Physics Research Section A: Accelerators, Spectrometers, Detectors and Associated Equipment*, vol. 723, pp. 47 – 54, 2013. [Online]. Available: http://www.sciencedirect.com/science/article/pii/S0168900213004816

[82] I. Mandic, V. Cindro, M. Deliyergiyev *et al.*, "First results from the online radiation dose monitoring system in ATLAS experiment," in *2011 IEEE Nucl. Sci. Symp. Conf. Rec.*, Oct. 2011, pp. 1107–1112, doi: 10.1109/NSSMIC.2011.6154582.

[83] D. Turecek, T. Holy, J. Jakubek *et al.*, "Pixelman: a multi-platform data acquisition and processing software package for Medipix2, Timepix and Medipix3 detectors," *J. Instrum.*, vol. 6, no. 01, p. C01046, 2011.

[84] J. Bouchami *et al.*, "Estimate of the neutron fields in ATLAS based on ATLAS-MPX detectors data," *JINST*, vol. 6, p. C01042, 2011.

[85] P. Mánek, "Machine learning approach to ionizing particle recognition using hybrid active pixel detectors," Master's thesis, Czech Technical University in Prague, 2018.

[86] W. Furnell, A. Shenoy, E. Fox *et al.*, "First results from the lucid-timepix spacecraft payload onboard the techdemosat-1 satellite in low earth orbit," *Advances in Space Research*, vol. 63, no. 5, pp. 1523 – 1540, 2019. [Online]. Available: http://www.sciencedirect.com/science/article/pii/S0273117718308330

[87] A. Ferrari, P. R. Sala, A. Fasso *et al.*, "FLUKA: A multi-particle transport code (Program version 2005)," CERN, Tech. Rep. CERN-2005-010, SLAC-R-773, INFN-TC-05-11, 2005. [Online]. Available: https://cds.cern.ch/record/898301

[88] T. Böhlen, F. Cerutti, M. Chin *et al.*, "The fluka code: Developments and challenges for high energy and medical applications," *Nuclear Data Sheets*, vol. 120, pp. 211 – 214, 2014. [Online]. Available: http://www.sciencedirect.com/science/article/pii/S0090375214005018

[89] (2019, Apr.) ATLAS Experiment - Public Results. [Online]. Available: https://twiki.cern.ch/twiki/bin/view/AtlasPublic/RadiationSimulationPublicResults

[90] I. Mandic, V. Cindro, A. Gorisek *et al.*, "Online Integrating Radiation Monitoring System for the ATLAS Detector at the Large Hadron Collider," *IEEE Transactions on Nuclear Science*, vol. 54, no. 4, pp. 1143–1150, Aug 2007.

[91] M. Reinhard and A. Rosenfeld, "Determination of 1 MeV equivalent neutron fluence using a P-I-N dosimeter diode," in *Proceedings of the 4th Australian experimental high energy physics meeting and workshop.* Australia: ANSTO, 1995, p. 72. [Online]. Available: http://inis.iaea.org/search/search.aspx?orig_q=RN:29003456

[92] I. V. Gorelov, "A Leakage Current-based Measurement of the Radiation Damage in the ATLAS Pixel Detector," *JINST*, vol. 10, no. 04, p. C04024, 2015, doi: 10.1088/1748-0221/10/04/C04024.

[93] A. L. Schorlemmer, "Monitoring radiation damage in the ATLAS pixel detector," Ph.D. dissertation, Gottingen U., II. Phys. Inst., 2014-06-11.

[94] I. Mandić *et al.*, "First Results from the Online Radiation Dose Monitoring System in ATLAS experiment," in *Proceedings, 2011 IEEE Nuclear Science Symposium and Medical Imaging Conference (NSS/MIC 2011): Valencia, Spain, October 23-29, 2011*, 2011, pp. 1107–1112. [Online]. Available: http://cdsweb.cern.ch/record/1400437/files/ATL-INDET-PROC-2011-034.pdf

[95] F. Ravotti, M. Glaser, and M. Moll, "Sensor catalogue data compilation of solid-state sensors for radiation monitoring," CERN, Geneva, Tech. Rep. CERN-TS-Note-2005-002, May 2005. [Online]. Available: http://cds.cern.ch/record/835408

[96] M. Campbell, C. Leroy, S. Pospisil *et al.*, "Measurement of Spectral Characteristics and Composition of Radiation in ATLAS by MEDIPIX2-USB Devices," CERN, Geneva, Switzerland, Tech. Rep. ATL-R-MA-0001, 2006.

[97] Data set of radiation field particles hitting ATLAS-TPX detectors, obtained from FLUKA simulations performed by Tatsumi Koi (SLAC) in 2016.

[98] M. Tavlet and M. E. Leon Florian, "Dose and neutron-fluence measurements in mixed gamma-neutron fields by means of semi-conductor dosimeters," in *RADECS 93. Second European Conference on Radiation and its Effects on Components and Systems (Cat. No.93TH0616-3)*, Sep. 1993, pp. 27–32.

[99] P. Rubovič, B. Bergmann, D. Ekendahl *et al.*, "Timepix detector as a tool for x-ray and gamma dosimetry," *Radiation Measurements*, vol. 107, pp. 39 – 42, Dec. 2017, doi: 10.1016/j.radmeas.2017.10.012.

[100] B. Bergmann, T. Billoud, C. Leroy *et al.*, "Characterization of the Radiation Field in the ATLAS Experiment With Timepix Detectors," *IEEE Trans. Nucl. Sci*, vol. 66, no. 7, pp. 1861–1869, July 2019, doi: 10.1109/TNS.2019.2918365.

[101] H. Vincke and C. Theis, "ActiWiz – optimizing your nuclide inventory at proton accelerators with a computer code," *Prog. Nucl. Sci. Tech.*, vol. 4, pp. 228–232. 5 p, 2014, doi: 10.15669/pnst.4.228.

[102] F. Ravotti, M. Glaser, and M. Moll, "Sensor catalogue data compilation of solid-state sensors for radiation monitoring," CERN, Geneva, Tech. Rep. CERN-TS-Note-2005-002, May 2005. [Online]. Available: http://cds.cern.ch/record/835408

[103] I. Mandic, V. Cindro, M. Deliyergiyev *et al.*, "First results from the online radiation dose monitoring system in ATLAS experiment," in *2011 IEEE Nucl. Sci. Symp. Conf. Rec.*, Oct. 2011, pp. 1107–1112, doi: 10.1109/NSSMIC.2011.6154582.

[104] R. Harper, C. Buttar, P. Allport *et al.*, "Evolution of silicon microstrip detector currents during proton irradiation at the CERN PS," *Nucl. Instrum. Methods Phys. Res. A, Accel. Spectrom. Detect. Assoc. Equip.*, vol. 479, no. 2, pp. 548 – 554, Mar. 2002, doi: 10.1016/S0168-9002(01)00945-7.

[105] I. Gorelov, "A leakage current-based measurement of the radiation damage in the ATLAS pixel detector," *J. Instrum.*, vol. 10, no. 04, pp. C04 024–C04 024, apr 2015, doi: 10.1088/1748-0221/10/04/c04024. [Online]. Available: https://iopscience.iop.org/article/10.1088/1748-0221/10/04/C04024

[106] M. Moll, "Radiation damage in silicon particle detectors: Microscopic defects and macroscopic properties," Ph.D. dissertation, Hamburg Univ., Hamburg, Germany, 1999. [Online]. Available: http://www-library.desy.de/cgi-bin/showprep.pl?desy-thesis99-040

[107] X. Llopart, R. Ballabriga, M. Campbell *et al.*, "Timepix, a 65k programmable pixel readout chip for arrival time, energy and/or photon counting measurements," *Nucl. Instr. Meth. Phys. Res. A*, vol. 581, no. 1–2, pp. 485 – 494, 2007, doi: 10.1016/j.nima.2007.08.079.

[108] C. Leroy, S. Pospisil, M. Suk *et al.*, "Proposal to Measure Radiation Field Characteristics, Luminosity and Induced Radioactivity in ATLAS with Timepix Devices," CERN, Geneva, Switzerland, Tech. Rep. ATL-R-MA-0001, 2014.

[109] C. Teyssier, J. Bouchami, F. Dallaire *et al.*, "Performance of the Medipix and Timepix devices for the recognition of electron-gamma radiation fields," *Nucl. Instrum. Methods Phys. Res. A, Accel. Spectrom. Detect. Assoc. Equip.*, vol. 650, no. 1, pp. 92 – 97, 2011, doi: 10.1016/j.nima.2010.12.114.

[110] A. Sopczak *et al.*, "Precision Luminosity of LHC Proton–Proton Collisions at 13 TeV Using Hit Counting With TPX Pixel Devices," *IEEE Trans. Nucl. Sci.*, vol. 64, no. 3, pp. 915–924, Mar. 2017, doi: 10.1109/TNS.2017.2664664.

[111] J. Bouchami, A. Gutiérrez, T. Holy *et al.*, "Measurement of pattern recognition efficiency of tracks generated by ionizing radiation in a Medipix2 device," *Nucl. Instrum. Methods Phys. Res. A, Accel. Spectrom. Detect. Assoc. Equip.*, vol. 633, pp. S187 – S189, 2011, doi: 10.1016/j.nima.2010.06.163.

[112] N. Asbah, C. Leroy, S. Pospisil *et al.*, "Measurement of the efficiency of the pattern recognition of tracks generated by ionizing radiation in a Timepix detector," *J. Instrum.*, vol. 9, no. 05, p. C05021, May 2014, doi: 10.1088/1748-0221/9/05/C05021.

[113] S. Gohl, B. Bergmann, H. Evans *et al.*, "Study of the radiation fields in LEO with the Space Application of Timepix Radiation Monitor (SATRAM)," *Advances in Space Res.*, 2018, doi: 10.1016/j.asr.2018.11.016.

[114] M. Campbell, V. Havranek, E. Heijne *et al.*, "Charge collection from proton and alpha particle tracks in silicon pixel detector devices," in *2007 IEEE Nucl. Sci. Symp. Conf. Rec.*, vol. 2, Oct. 2007, pp. 1047–1050, doi: 10.1109/NSSMIC.2007.4437190.

[115] S. Gohl, B. Bergmann, C. Granja *et al.*, "Measurement of particle directions in low earth orbit with a Timepix," *J. Instrum.*, vol. 11, no. 11, p. C11023, Nov. 2016, doi: 10.1088/1748-0221/11/11/c11023.

[116] S. Agostinelli, J. Allison, K. Amako *et al.*, "Geant4—a simulation toolkit," *Nucl. Instrum. Methods Phys. Res. A, Accel. Spectrom. Detect. Assoc. Equip.*, vol. 506, no. 3, pp. 250 – 303, 2003, doi: 10.1016/S0168-9002(03)01368-8.

[117] B. Bergmann, "Improved methodology of the recognition and separation of X-rays, neutrons and charged particles with hybrid active pixel detectors," Ph.D. dissertation, University of Erlangen–Nuremberg, Erlangen, Germany, Work in progress.

[118] [Online]. Available: http://atlas.web.cern.ch/Atlas/GROUPS/Shielding/shielding.htm#part7

[119] T. Poikela, J. Plosila, T. Westerlund *et al.*, "Timepix3: a 65K channel hybrid pixel readout chip with simultaneous ToA/ToT and sparse readout," *J. Instrum.*, vol. 9, no. 05, p. C05013, May 2014, doi: 10.1088/1748-0221/9/05/C05013.

[120] B. Bergmann, M. Pichotka, S. Pospisil *et al.*, "3d track reconstruction capability of a silicon hybrid active pixel detector," *The Eur. Physical J. C*, vol. 77, no. 6, p. 421, Jun. 2017, doi: 10.1140/epjc/s10052-017-4993-4.

[121] P. Burian, P. Broulím, B. Bergmann *et al.*, "Timepix3 detector network at ATLAS experiment," *J. Instrum.*, vol. 13, no. 11, p. C11024, Nov. 2018, doi: 10.1088/1748-0221/13/11/c11024.

[122] P. Lisowski and K. Schoenberg, "The Los Alamos Neutron Science Center," *Nucl. Instrum. Methods Phys. Res. A, Accel. Spectrom. Detect. Assoc. Equip.*, vol. 562, pp. 910–914, Jun. 2006, doi: 10.1016/j.nima.2006.02.178.

[123] L. Dimitrov, P. Iaydjiev, G. Mitev *et al.*, "Radiation Monitoring at the New GIF++ Irradiation Facility at CERN," *Bulg. J. Phys.*, vol. 42, no. 2, pp. 163–171, 2015.

[124] A. Owens, "Semiconductor materials and radiation detection," *Journal of synchrotron radiation*, vol. 13, pp. 143–50, 04 2006.

[125] A. Kozorezov, J. Wigmore, A. Owens *et al.*, "Resolution degradation of semiconductor detectors due to carrier trapping," *Nuclear Instruments and Methods in Physics Research Section A: Accelerators, Spectrometers, Detectors and Associated Equipment*, vol. 546, no. 1, pp. 209 – 212, 2005, proceedings of the 6th International Workshop on Radiation Imaging Detectors. [Online]. Available: http://www.sciencedirect.com/science/article/pii/S0168900205006303

[126] A. Cola and I. Farella, "The polarization mechanism in cdte schottky detectors," *Applied Physics Letters*, vol. 94, pp. 102 113–102 113, 03 2009.

[127] C. Buis, G. Marrakchi, T. A. Lafford *et al.*, "Effects of dislocation walls on image quality when using Cadmium Telluride X-ray detectors," *IEEE Transactions on Nuclear Science*, vol. 60, no. 1, 2013.

[128] M. J. Berger, J. H. Hubbell, S. M. Seltzer *et al.* (2010. [Online] Available: http://physics.nist.gov/xcom [2017 December 11]. National Institute of Standards and Technology, Gaithersburg, MD.) XCOM: Photon Cross Section Database (version 1.5). [Online]. Available: http://physics.nist.gov/xcom

[129] M. Funaki, Y. Ando, R. Jinnai *et al.*, "Development of CdTe detectors in Acrorad," presented at the International Workshop on Semiconductor PET, 2007. [Online] Available: http://www.acrorad.co.jp/_skin/pdf/Development_of_CdTe_detectors.pdf. [Online]. Available: http://www.acrorad.co.jp/_skin/pdf/Development_of_CdTe_detectors.pdf

[130] E. Hamann, A. Cecilia, A. Zwerger *et al.*, "Characterization of photon counting pixel detectors based on semi-insulating GaAs sensor material," *J. Phys. Conf. Ser.*, vol. 425, no. 6, p. 062015, 2013. [Online]. Available: http://stacks.iop.org/1742-6596/425/i=6/a=062015

[131] A. I. Ayzenshtat, D. L. Budnitsky, O. B. Koretskaya *et al.*, "GaAs as a material for particle detectors," *Nucl. Instrum. Meth.*, vol. A494, pp. 120–127, 2002.

[132] P. Čermák, M. Fiederle, J. Jakůbek *et al.*, "Intrinsic properties of semiconductor detectors studied with charged particles using Timepix pixel devices in tracking mode," in *2008 IEEE Nuclear Science Symposium Conference Record*, vol. 16th International workshop on room-temperature semiconductor X- and Gamma-ray detectors (RTSD). IEEE RTSD R14-1 (Dresden, Germany), 2008. [Online]. Available: https://ieeexplore.ieee.org/document/4774079

[133] P. Cermak, I. Stekl, V. Bocarov *et al.*, "The characterization of CdTe Timepix device and the study of its capabilities for the double beta decay measurements," in *2008 IEEE Nuclear Science Symposium Conference Record*, Oct 2008, pp. 444 – 445.

[134] D. Budnitsky, A. Tyazhev, V. Novikov *et al.*, "Chromium-compensated GaAs detector material and sensors," *J. Instrum.*, vol. 9, no. 07, p. C07011, 2014. [Online]. Available: http://stacks.iop.org/1748-0221/9/i=07/a=C07011

[135] D. Greiffenberg, A. Fauler, A. Zwerger *et al.*, "Energy resolution and transport properties of CdTe-Timepix-Assemblies," *J. Instrum.*, vol. 6, p. C01058, 2011.

[136] M. Ruat and C. Ponchut, "Characterization of a pixelated CdTe X-ray detector using the Timepix photon-counting readout chip," *IEEE Transactions on Nuclear Science*, vol. 59, no. 5, pp. 2392 – 2401, Oct 2012.

[137] M. Ruat and M. Ponchut, "Defect signature, instabilities and polarization in CdTe X-ray sensors with quasi-ohmic contacts," *J. Instrum.*, vol. 9, no. 04, p. C04030, 2014.

[138] C. Ponchut and M. Ruat, "Energy calibration of a CdTe X-ray pixel sensor hybridized to a Timepix chip," *J. Instrum.*, vol. 8, no. 01, p. C01005, 2013. [Online]. Available: http://stacks.iop.org/1748-0221/8/i=01/a=C01005

[139] T. Billoud, C. Leroy, C. Papadatos *et al.*, "Characterization of a pixelated CdTe timepix detector operated in ToT mode," *Journal of Instrumentation*, vol. 12, no. 01, pp. P01018–P01018, jan 2017. [Online]. Available: https://doi.org/10.1088%2F1748-0221%2F12%2F01%2Fp01018

[140] M. Funaki, Y. Ando, R. Jinnai *et al.*, "Development of CdTe detectors in Acrorad," presented at the International Workshop on Semiconductor PET, 2007. [Online] Available: http://www.acrorad.co.jp/_skin/pdf/Development_of_CdTe_detectors.pdf. [Online]. Available: http://www.acrorad.co.jp/_skin/pdf/Development_of_CdTe_detectors.pdf

[141] M. Campbell, E. Heijne, T. Holý *et al.*, "Study of the charge sharing in a silicon pixel detector by means of $\alpha$-particles interacting with a Medipix2 device," *Nucl. Instr. Meth. Phys. Res. A*, vol. 591, no. 1, pp. 38 – 41, 2008, doi: 10.1016/j.nima.2008.03.096.

[142] J. Bouchami, A. Gutiérrez, A. Houdayer *et al.*, "Study of the charge sharing in silicon pixel detector by means of heavy ionizing particles interacting with a Medipix2 device," *Nucl. Instr. Meth. Phys. Res. A*, vol. 633, Supplement 1, pp. S117 – S120, 2011, doi: 10.1016/j.nima.2010.06.141.

[143] V. Kraus, M. Holik, J. Jakubek *et al.*, "FITPix — fast interface for Timepix pixel detectors," *J. Instrum.*, vol. 6, no. 01, p. C01079, 2011.

[144] D. Turecek, T. Holy, J. Jakubek *et al.*, "Pixelman: a multi-platform data acquisition and processing software package for Medipix2, Timepix and Medipix3 detectors," *J. Instrum.*, vol. 6, no. 01, p. C01046, 2011.

[145] J. F. Ziegler, M. Ziegler, and J. Biersack, "SRIM – The stopping and range of ions in matter (2010)," *Nucl. Instr. Meth. Phys. Res. B*, vol. 268, no. 11–12, pp. 1818 – 1823, 2010, 19th International Conference on Ion Beam Analysis. [Online]. Available: http://www.sciencedirect.com/science/article/pii/S0168583X10001862

[146] J. Jakubek, A. Cejnarova, T. Holy *et al.*, "Pixel detectors for imaging with heavy charged particles," *Nucl. Instr. Meth. Phys. Res. A*, vol. 591, no. 1, pp. 155 – 158, 2008, doi: 10.1016/j.nima.2008.03.091.

[147] D. Turecek, J. Jakubek, M. Kroupa *et al.*, "Energy calibration of pixel detector working in Time-Over-Threshold mode using test pulses," in *Nuclear Science Symposium and Medical Imaging Conference (NSS/MIC)*. IEEE, 2011, doi: 10.1109/NSSMIC.2011.6154668.

[148] J. Jakubek, "Precise energy calibration of pixel detector working in time-over-threshold mode," *Nucl. Instr. Meth. Phys. Res. A*, vol. 633, Supplement 1, pp. S262 – S266, 2011. [Online]. Available: http://www.sciencedirect.com/science/article/pii/S0168900210013732

[149] A. Owens and A. Peacock, "Compound semiconductor radiation detectors," *Nucl. Instr. Meth. Phys. Res. A*, vol. 531, no. 1–2, pp. 18 – 37, 2004, proceedings of the 5th International Workshop on Radiation Imaging Detectors. [Online]. Available: http://www.sciencedirect.com/science/article/pii/S0168900204010575

[150] R. Devanathan, L. Corrales, F. Gao *et al.*, "Signal variance in gamma-ray detectors—A review," *Nucl. Instr. Meth. Phys. Res. A*, vol. 565, no. 2, pp. 637 – 649, 2006. [Online]. Available: http://www.sciencedirect.com/science/article/pii/S0168900206009089

[151] S. Del Sordo, L. Abbene, E. Caroli *et al.*, "Progress in the development of CdTe and CdZnTe semiconductor radiation detectors for astrophysical and medical applications," *Sensors*, vol. 9, no. 5, p. 3491, 2009. [Online]. Available: http://www.mdpi.com/1424-8220/9/5/3491

[152] P. J. Sellin, A. W. Davies, A. Lohstroh *et al.*, "Drift mobility and mobility-lifetime products in CdTe:Cl grown by the travelling heater method," *IEEE Transactions on Nuclear Science*, vol. 52, no. 6, pp. 3074 – 3078, 2005.

[153] H. Shiraki, M. Funaki, Y. Ando *et al.*, "Improvement of the productivity in the growth of CdTe single crystal by THM for the new PET system," in *2007 IEEE Nuclear Science Symposium Conference Record*, vol. 3, Oct 2007, pp. 1783 – 1787.

[154] T. Takahashi, T. Mitani, Y. Kobayashi *et al.*, "High resolution Schottky CdTe diode detector," in *Nuclear Science Symposium Conference Record, 2001 IEEE*, vol. 4, 2001, pp. 2464 – 2468.

[155] R. Bell, G. Entine, and H. Serreze, "Time-dependent polarization of CdTe gamma-ray detectors," *Nucl. Instrum. Meth.*, vol. 117, no. 1, pp. 267 – 271, 1974. [Online]. Available: http://www.sciencedirect.com/science/article/pii/0029554X7490408X

[156] K. Okada, Y. Sakurai, and H. Suematsu, "Characteristics of both carriers with polarization in diode-type CdTe x-ray detectors," *Appl. Phys. Lett.*, vol. 90, no. 6, 2007. [Online]. Available: http://scitation.aip.org/content/aip/journal/apl/90/6/10.1063/1.2457971

[157] M. Ruat and C. Ponchut, "Characterization of a pixelated CdTe X-ray detector using the Timepix photon-counting readout chip," *IEEE Transactions on Nuclear Science*, vol. 59, no. 5, pp. 2392 – 2401, Oct 2012.

[158] M. Ruat and C. Ponchut, "Defect signature, instabilities and polarization in CdTe X-ray sensors with quasi-ohmic contacts," *J. Instrum.*, vol. 9, no. 04, p. C04030, 2014.

[159] J. M. Jose, P. Čermák, I. Štekl *et al.*, "Timepix background studies for double beta decay experiments," *J. Instrum.*, vol. 6, no. 11, p. C11030, 2011.

[160] M. Schwenke, K. Zuber, B. Janutta *et al.*, "Exploration of pixelated detectors for double beta decay searches within the COBRA experiment," *Nucl. Instr. Meth. Phys. Res. A*, vol. 650, no. 1, pp. 73 –

78, 2011, international Workshop on Semiconductor Pixel Detectors for Particles and Imaging 2010. [Online]. Available: http://www.sciencedirect.com/science/article/pii/S0168900210029086

[161] T. Billoud, C. Leroy, C. Papadatos *et al.*, "Homogeneity study of a GaAs:cr pixelated sensor by means of x-rays," *Journal of Instrumentation*, vol. 13, no. 04, pp. P04 002–P04 002, apr 2018. [Online]. Available: https://doi.org/10.1088%2F1748-0221%2F13%2F04%2Fp04002

[162] J. W. Allen, "Gallium Arsenide as a Semi-insulator," *Nature*, vol. 187, pp. 403 – 405, 07 1960. [Online]. Available: http://dx.doi.org/10.1038/187403b0

[163] J. E. Eberhardt, R. D. Ryan, and A. J. Tavendale, "High-resolution nuclear radiation detectors from epitaxial n-GaAs," *Appl. Phys. Lett.*, vol. 17, no. 10, pp. 427 – 429, 1970.

[164] G. Ayzenshtat, N. Bakin, D. Budnitsky *et al.*, "GaAs structures for X-ray imaging detectors," *Nucl. Instr. Meth. Phys. Res. A*, vol. 466, no. 1, pp. 25 – 32, 2001, 2nd Int. Workshop on Radiation Imaging Detectors. [Online]. Available: http://www.sciencedirect.com/science/article/pii/S0168900201008208

[165] G. Bertuccio and D. Maiocchi, "Electron-hole pair generation energy in gallium arsenide by x and gamma photons," *J. Appl. Phys.*, vol. 92, pp. 1248 – 1255, Aug. 2002.

[166] M. Veale, S. Bell, D. Duarte *et al.*, "Chromium compensated gallium arsenide detectors for X-ray and $\gamma$-ray spectroscopic imaging," *Nucl. Instr. Meth. Phys. Res. A*, vol. 752, pp. 6 – 14, 2014. [Online]. Available: http://www.sciencedirect.com/science/article/pii/S0168900214003271

[167] J. Jakubek, "Precise energy calibration of pixel detector working in time-over-threshold mode," *Nucl. Instr. Meth. Phys. Res. A*, vol. 633, Supplement 1, pp. S262 – S266, 2011, doi: 10.1016/j.nima.2010.06.183.

[168] R. Brun and F. Rademakers, "ROOT — An object oriented data analysis framework," *Nucl. Instr. Meth. Phys. Res. A*, vol. 389, no. 1, pp. 81 – 86, 1997, doi: 10.1016/S0168-9002(97)00048-X.

[169] http://advacam.com/camera/modupix-tracker [2017, December 11], accessed: 2017-09-05. [Online]. Available: http://www.advacam.com/en/products/modupix

[170] B. van der Heijden, J. Visser, M. van Beuzekom *et al.*, "SPIDR, a general-purpose readout system for pixel ASICs," *J. Instrum.*, vol. 12, no. 02, p. C02040, 2017. [Online]. Available: http://stacks.iop.org/1748-0221/12/i=02/a=C02040

[171] S. Ramo, "Currents induced by electron motion," *Proc. Ire.*, vol. 27, pp. 584 – 585, 1939, doi: 10.1109/JRPROC.1939.228757.

[172] G. Knoll, *Radiation Detection and Measurement*. Wiley, 2000. [Online]. Available: https://books.google.fi/books?id=HKBVAAAAMAAJ

[173] U. Lachish, "Electron lifetime determination in semiconductor gamma detector arrays," *arXiv*, Mar. 2017. [Online]. Available: https://arxiv.org/abs/1701.03459

[174] W. Riegler and G. A. Rinella, "Point charge potential and weighting field of a pixel or pad in a plane condenser," *Nucl. Instr. Meth. Phys. Res. A*, vol. 767, pp. 267 – 270, 2014, doi: 10.1016/j.nima.2014.08.044.

[175] J. Jakubek, "Energy-sensitive X-ray radiography and charge sharing effect in pixelated detector," *Nucl. Instr. Meth. Phys. Res. A*, vol. 607, no. 1, pp. 192 – 195, 2009, radiation Imaging Detectors 2008. [Online]. Available: http://www.sciencedirect.com/science/article/pii/S0168900209006408

[176] U. Lachish, "CdTe and CdZnTe semiconductor gamma detectors equipped with ohmic contacts," *Nucl. Instr. Meth. Phys. Res. A*, vol. 436, no. 1, pp. 146 – 149, 1999. [Online]. Available: http://www.sciencedirect.com/science/article/pii/S0168900299006117

[177] E. Hamann, T. Koenig, M. Zuber *et al.*, "Investigation of GaAs:Cr Timepix assemblies under high flux irradiation," *J. Instrum.*, vol. 10, no. 01, p. C01047, 2015. [Online]. Available: http://stacks.iop.org/1748-0221/10/i=01/a=C01047

[178] P. Rudolph, "Dislocation cell structures in melt-grown semiconductor compound crystals," *Cryst. Res. Technol.*, vol. 40, no. 1-2, pp. 7 – 20, 2005. [Online]. Available: 10.1002/crat.200410302

[179] E. Hamann, T. Koenig, M. Zuber *et al.*, "Performance of a Medipix3RX spectroscopic pixel detector with a high resistivity gallium arsenide sensor," *IEEE Transactions on Medical Imaging*, vol. 34, no. 3, pp. 707–715, March 2015.

[180] A. Butler, P. Butler, S. Bell *et al.*, "Measurement of the energy resolution and calibration of hybrid pixel detectors with GaAs:Cr sensor and Timepix readout chip," *Phys. Part. Nuclei Lett.*, vol. 12, no. 1, pp. 59 – 73, 2015. [Online]. Available: 10.1134/S1547477115010021

[181] D. Dedovich, M. Demichev, A. Gongadze *et al.*, "Proposal to measure radiation field characteristics, luminosity and induced radioactivity in ATLAS with Timepix detectors having GaAs:Cr sensors," CERN, Tech. Rep. ATL-COM-GEN-2016-001, 2016.

[182] D. Turecek, J. Jakubek, E. Trojanova *et al.*, "Compton camera based on timepix3 technology," *Journal of Instrumentation*, vol. 13, no. 11, pp. C11 022–C11 022, nov 2018. [Online]. Available: https://doi.org/10.1088/1748-0221/13/11/c11022